Eddy Current braking applied to the Kosmos-3M second rocket stage

Master Thesis

Michielsen Marijn

Technische Universiteit Delft

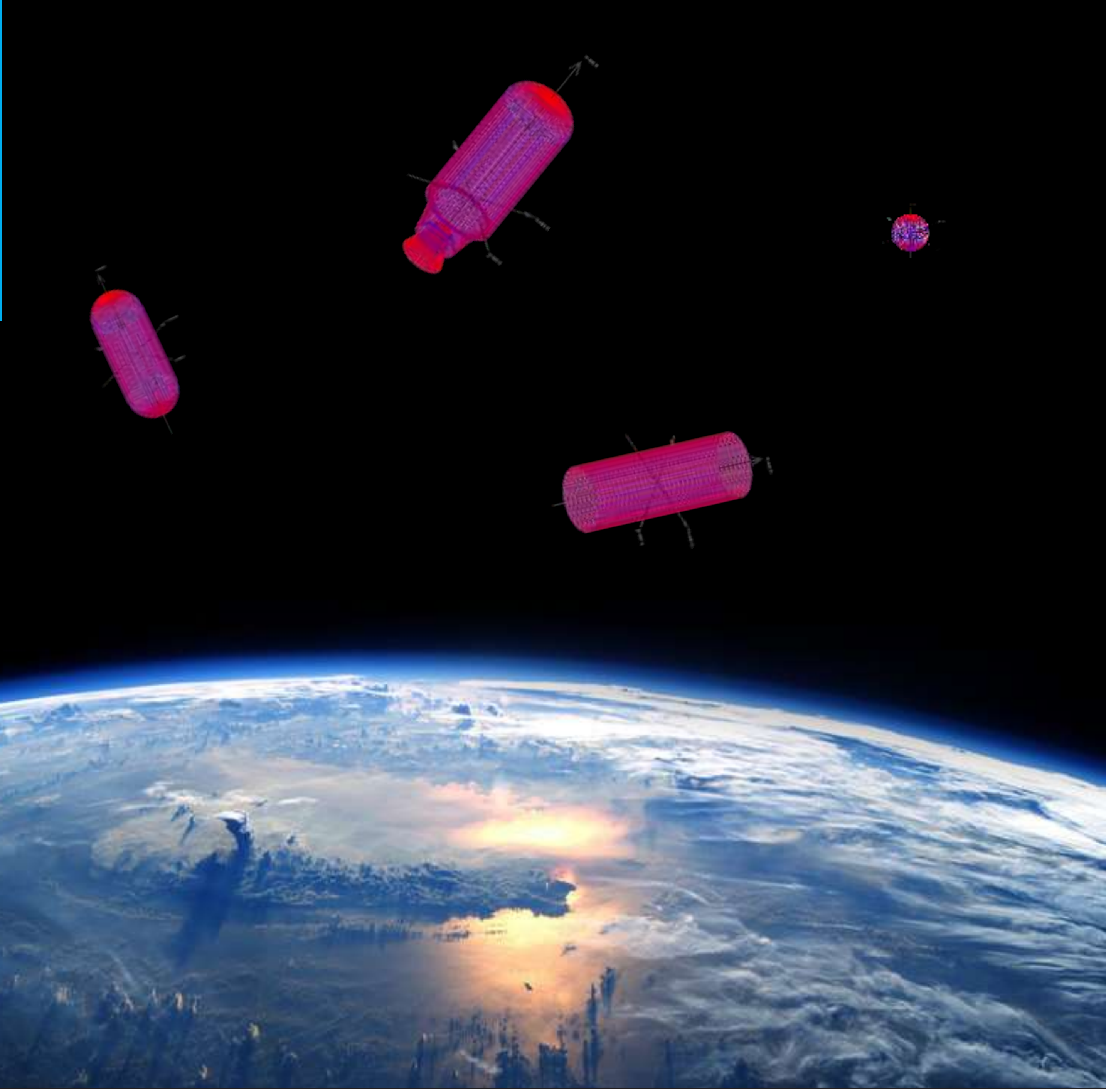

Delft University of Technology

Challenge the future

Eddy Current braking applied to the Kosmos-3M second rocket stage

Master Thesis

by

Michielsen Marijn

Master of Science
in Aerospace Engineering

at the Delft University of Technology,

Supervisors: ir. K. Cowan
ir. R. Noomen

Preface

This Thesis is written as part of the Master Space Exploration at the Delft University of Technology. My personal aim for this Thesis was to do something unique, something innovative, something that would be a useful contribution to existing research. As a member of the generation raised in the midst of an energy revolution and global warming, with an increased awareness on the pollution of the Earth and space by our hands, I decided to let my Thesis focus on Space Debris, possibly aiding in finding a solution to the Space Debris problem above our heads.

There, of course, are reasons why there are no solutions flying in Earth orbits at the moment, not the least of which are the technological difficulties involved. The first and most important step of the Thesis was to find the area in which I would do my research and develop concepts. Therefore, I would first of all like to thank my supervisor Kevin Cowan for helping me brainstorm and fine-tune my concept and giving me the freedom to do so. Furthermore, the nights out drinking with my friends probably sparked the idea for the final concept. Therefore, I must thank my friends as well, although they are not worthy to be named.

I would also like to thank Fran, the girlfriend, who stuck with me throughout my studies, although she already started working 2.5 years ago and is waiting impatiently for me to graduate too, so she can finally have a place of her/our own.

Last but not least, I would like to thank my parents for allowing me to study in a foreign country, and for never losing faith in me, although their patience had almost run out.

Michielsen Marijn
Delft, June 2016

Summary

The orbits around the Earth are filled with satellites, space stations and more and many of these objects are non-functioning, non-cooperative objects. For many years, and especially during the cold war, objects have been launched into orbit without an End-of-Life(EOL) strategy and while space stands as a synonym for infinite, the orbits around the Earth are anything but.

Over the last decade the space debris problem has gotten some public awareness, with major newspapers covering stories about the problem and no three months pass by without the International Space Station(ISS) having an impeding collision warning and needs to perform a Just-in-time Collision Avoidance(JCA) manoeuvre. Public awareness, however, is not a guarantee for a quick solution.

While money plays a major part in the reason why there is no solution at hand, the technological challenges involved in removing debris from Earth orbits is definitely not to be overlooked. One of the biggest challenges of removing debris from Earth orbits is that they are rotating over multiple axes at speeds exceeding 10 rpm, making them hard or even impossible to grapple, while non-grappling techniques, like a space harpoon, could achieve a successful de-orbit mission, but due to the penetrative nature of the harpoon it creates smaller pieces of debris, which are untraceable with conventional techniques.

Research papers have stated that, for mechanical docking to become manageable, with the associated relative motion sensing and control, the spin rate should be less than 0.5 rpm. Docking with an uncooperative object would also allow for On-Orbit Servicing(OOS), which could generate more interest in a solution for the space debris problem.

It can, thus, be concluded that there is a need for a solution that can detumble a large amount of the debris population to allow for Active Debris Removal(ADR) missions, because if no measures are taken, then it is not a question if, but when two objects will collide in orbit again.

In order to detumble space debris, eddy current braking(ECB) is chosen as an ideal candidate, primarily because it is a contact-less technology that works both in LEO and GEO and can be used for a large range of shapes and sizes. The major downside of using ECB to brake the rotation of uncooperative objects is that it requires these objects to be partly made out of conductive materials.

Before the detumbling can be simulated, suitable targets need to be found. The most crowded region in Low Earth Orbit(LEO) is located around 950 km above the Earth. This region consists mainly of Kosmos-3M upper stages, which are due to their cylindrical shape and materials, ideal candidates to be detumbled by ECB.

Therefore, this thesis models the shape of the second rocket stages of the Kosmos-3M rockets, which are clustered together in LEO, and simulates the tumbling of these rocket stages to assess the braking force generated by using an ECB, in order to show that large uncooperative objects in space can be detumbled by the use of an ECB. Mainly, it focuses on the detumbling time and magnetic interactions.

An ECB consists of an electromagnet, which generates a magnetic field that needs to be aimed towards the target, which in this case is the Kosmos-3M second stage. First of all, this electromagnet needs to be designed in order to estimate the strength of the magnetic field that can be created. A high-temperature super-conducting electromagnetic coil is the ideal candidate in order to allow a strong magnetic field to be created. More specifically magnesium diboride will be used as the material for the coil. Based on the maximum coil radius, critical current density of MgB_2, number of loops, the maximum configuration of the coil will have a diameter of 1 meter, 500 windings and a current of 68.5 Ampere, which leads to a magnetic field of around 0.022 Tesla being created at the center of the coil. This design is within the power, size and weight constraints and will be used to detumble the Kosmos-3M second rocket stages.

After the magnetic field is simulated, objects can be placed within that magnetic field to assess the braking forces, detumbling time and more. First of all, basic shapes such as the sphere, cylinder and double silo are modelled and their Magnetic Tensor, which describes how a conductive object will react when it is placed in a magnetic field, simulated in order to verify the model. Furthermore, the torque is simulated in order to get an initial impression of the magnitude of the torque and the detumbling time. Different magnetic field vectors and rotational vectors are chosen for the different shapes in order to show different scenarios and their result.

After the detumbling of uncooperative objects in LEO is verified by using basic shapes, the shape of the Kosmos-3M upper stage is used as input in the model, together with a revision of the input parameters in order to better represent the real-life situation in orbit. Specifically, the position of the magnetic field vector relative to the chaser fixed frame in which the target rotates is focused on, and it is shown that for the ideal situation, when the magnetic field vector and rotation vector are perpendicular, that the Kosmos-3M second rocket stage can be detumbled in the space of 7 days.

The simulation of the torques generated by placing the Kosmos-3M in a magnetic field neglects certain forces, torques and perturbations present when using an electromagnet as ECB. The chaser and target fly in formation for the duration of the mission, with formation flying being a proven process. However, the electromagnet presents a new factor, influencing this formation, adding other magnetic interactions to the problem. More specifically, the non-uniformity of the magnetic field leads to a decrease in size in the elements of the Magnetic Tensor, leading to an increase in detumbling time. Furthermore, the interaction of the Earth's magnetic field with the chaser and target is simulated in order to confirm that Attitude Determination and Control Systems(ADCS's) are capable of counteracting the torques generated on the chaser and assess the influence on the detumbling time. And, finally the interaction of the magnetic field generated by the ECB and ferromagnetic materials present in the Kosmos-3M rocket is assessed. A first estimation of the torques due to the interaction of the magnetic field with the ferromagnetic materials on the Kosmos-3M second stage shows that it will have a relatively small influence on the detumbling mission.

The final simulation adds the magnetic interactions to the detumbling mission.

The non-uniformity of the magnetic field has a negative effect on the detumbling time of the Kosmos-3M second rocket stage, with detumbling times being generally around 1.5 times longer. Furthermore, the influence of the Earth's magnetic field is shown to influence the detumbling over the z-axis, decreasing the efficiency of the ECB, with the influence on the rotation over the x- and y-axis being relatively small in comparison, for short term detumbling missions. For missions lasting more than 100 days, the Earth's magnetic field has a stronger influence on all rotations compared to short term missions. And finally the presence of ferromagnetic materials and closed current loops in the target only lead to small disturbances when the rotational velocity of the uncooperative object is close to zero.

Combining all the magnetic interactions, it is concluded that they have a negative effect on the detumbling time and state, with the detumbling taking both longer and converging to a higher rotational velocity compared to the case where no magnetic interactions are considered. Therefore, an alternate mission is proposed that consists of three phases, namely a first detumbling phase lasting 15 days, a realignment of the chaser phase and a final detumbling phase. It is shown that when the angle over which the chaser realigns itself relative to the uncooperative object is close to 90 degrees, all rotations converge to a value close to 0 degrees per second within the space of 31 days.

Contents

Acronyms

AC Alternating Current. 31, 69

ADCS's Attitude Determination and Control Systems. 65, 69

ADR Active Debris Removal. 1, 2, 5–8, 35, 58

ASAT Anti-Satellite Weapon. 6

CERN European Organization for Nuclear Research. 16

CMGs Control Moment Gyros. 69, 70

CoG Center of Gravity. 35, 51, 53, 65, 66, 74, 83

CoM Center of Mass. 8, 11

DC Direct Current. 31, 71

ECB Eddy Current Brake. 1–3, 5, 11, 13, 15–17, 19–23, 25–27, 31, 33, 35, 37–39, 42, 49, 55–60, 62, 65–72, 74, 76, 77, 79

emf Electromotive force. 12

ESA European Space Agency. 6

FEM Finite Element Method. 18

GEO Geostationary Earth Orbit. 2, 7

HTS High Temperature Superconducting wires. 3, 16, 23, 25–27

IADC Inter-Agency Space Debris Coordination Committee. 5

ISS International Space Station. 6

JCA Just-in-Time Collision Avoidance. 6

LEO Low Earth Orbit. 2, 5–8, 16, 23, 51

LMRO's Launch and Mission Related Objects. 7, 8

MRI Magnetic Resonance Imaging. 16

NASA National Aeronautics and Space Administration. 6

NED North-East-Down. 67, 69, 74

OOS On-Orbit Servicing. 1, 5, 6, 8

PET Polyethylene Terephthalate. 45, 54

SATCAT online Satellite Catalog. 7

SR2S European Space Radiation Superconducting Shield. 16

TLEs Two-Line Elements. 7

WMM World Magnetic Model. 67

List of Symbols

α	Azimuthal spherical coordinate	rad
$\delta\theta$	Precession angle	rad
μ_0	Permeability of free space	$\mathrm{mkg/s^2A^2}$
μ_{eff}	Non-homogeneous effect on the Magnetic Tensor	-
ω	Angular velocity	rpm
ω_1	Angular velocity of the coil current	rpm
ω_m	Electric angular frequency	rpm
ω_s	Slip angular frequency	rpm
Φ_2	Inter linkage magnetic flux	Wb
ρ_c	Skin density	$\mathrm{kg/m^3}$
σ	Electrical conductivity	S/m
τ	Characteristic time of decay	s
a	Coil radius	m
A_k	Bar cross section	$\mathrm{m^2}$
B	Magnetic field	T
B_c	Critical magnetic field	T
B_x	X-component of the magnetic field	T
B_y	Y-component of the magnetic field	T
B_z	Z-component of the magnetic field	T
B_{r_c}	Radial component of magnetic field	T
d	Diameter of target	m
D_k	A bar constant	$\mathrm{S \cdot m}$
d_{com}	CoM from the intersection of the fuel cylinder and thruster mechanism	m
e	Thickness of the fuel cylinder	m
f	Induced force	N
H	Angular momentum	$\mathrm{kg\,m^2/s}$
I_0	Current in electromagnet	A

I_c	Critical current	A
I_f	Mass moment of inertia for the fuel cylinder	kg m^2
I_t	Mass moment of inertia for the fuel cylinder top	kg m^2
I_{T1}	Mass moment of inertia for the thruster mechanism	kg m^2
I_{T2}	Mass moment of inertia for the nozzle	kg m^2
J	Electric intensity	A m^4
J_c	Critical current density	T/m^2
j_k	Electric current density	A m^2
L	Total length of the target	m
l_f	Length of the fuel cylinder	m
L_k	Bar length	m
l_n	Length of the nozzle	m
l_t	Length of the thruster	m
l_{sp}	Spacing of the coil windings	m
M	Magnetic Tensor	S m^4
m_c	Total mass of conductive materials	kg
m_f	Mass of the fuel cylinder	kg
m_T	Total mass of the rocket	kg
m_t	Mass of the fuel cylinder top	kg
m_{nc}	Total mass of non-conductive materials	kg
m_{T1}	Mass of the thruster mechanism	kg
m_{T2}	Mass of the nozzle	kg
n_e	Winding number of the electromagnet	-
p	Pole pitch	rad
R	Outer body radius	m
R_0	Radius of the differential eddy current loop	m
r_2	Resistance	Ω
R_S	Inner body radius	m
R_T	Outer radius of nozzle	m
R_{Ti}	Inner radius of nozzle	m

T	Torque	$\mathrm{N \cdot m}$
t	Time	s
v	Velocity of electromagnet	m/s
V_0	Volume of the electrical circuit	$\mathrm{m^3}$
v_m	Relative velocity between coil and target	m/s
w	Width of ECB coil	m
x	Distance between coil and target	m

List of Figures

List of Tables

Introduction

The orbits around the Earth are filled with satellites, space stations and more and many of these objects are non-functioning, non-cooperative objects. For many years, and especially during the cold war, objects have been launched into orbit without an End Of Life (EOL) strategy and while space stands as a synonym for infinite, the orbits around the Earth are anything but.

Over the last decade the space debris problem has gotten some public awareness, with major newspapers covering stories about the problem and no three months pass by without the International Space Station (ISS) having an impeding collision warning and needs to perform a Just-in-time Collision Avoidance (JCA) manoeuvre. Public awareness, however, is not a guarantee for a quick solution. Many similarities can be found between the space debris problem and the junk and plastics floating around in the oceans, which are international waters. There are many parties responsible for said junk, and public awareness is high, yet no one is taking up responsibility to clean it up because in essence it is not their problem, since they float around in international territory. Furthermore, no economical advantage is perceivable, at least not in the near future, for the party that would clean up the oceans. Both of these arguments are also relevant for the space debris problem, with the uncooperative objects floating around in space, which is no one's territory and with only few economical advantages to be perceived. One economical advantage of cleaning the Earth's orbits is On-Orbit Servicing (OOS), which can pose as a significant cost reduction compared to launching a new satellite and is especially noteworthy since in the recent past the debris generated due to on-orbit failures are exceeding the debris created by launch failures.

However, only adding to the problem of space debris removal is international space law, which states that without consent from the owner or country, a non-functioning space object cannot be interfered with regardless of its functional status and regardless of the danger it poses.

As a result, funding for solutions to the junk problem in the oceans and the debris problem in Earth orbits, is lacking and research for both problems is only recently picking up some steam. While money plays a major part in the reason why there is no solution at hand, the technological challenges involved in removing debris from Earth orbits are definitely not to be overlooked. One of the biggest challenges of removing debris from Earth orbits is that they are rotating over multiple axis at speeds exceeding 10 rpm, making them hard or even impossible to grapple, while non-grappling techniques, like a space harpoon, could achieve a successful de-orbit mission, but due to the penetrative nature of the harpoon it creates smaller pieces of debris, which are untraceable with conventional techniques.

Research papers have stated that, for mechanical docking to become manageable, with the associated relative motion sensing and control, the spin rate should be less than 0.5 rpm. Docking with an uncooperative object would also allow for OOS, which could generate more interest in a solution for the space debris problem.

It can be concluded that there is a need for a solution that can detumble and remove or service a large amount of the debris population, because if no measures are taken, then it is not a question if, but when two objects will collide in orbit again.

The objective of this thesis is to prove that a tumbling Kosmos-3M second rocket stage can be detumbled with the use of an eddy current brake by designing an electromagnet or ECB and simulating the generated magnetic field, modelling the shape of Kosmos-3M upper rocket stages, simulating their tumbling motion, and modelling the torque induced by the ECB.

Chapter 1 describes the research in more detail and provides an overview of the steps taken. Chapter 2 presents a literature review of the published papers on the subject. Then the magnetic field generated by the chaser is analysed and discussed in Chapter 3, followed by a simplified initial detumbling mission by an ECB of differently shaped debris in Chapter 4. Chapter 5 analyses the detumbling of a Kosmos-3M second rocket stage and presents an initial conclusion. In Chapter 6 the magnetic interactions are discussed, which includes the influence of the Earth's magnetic field. Finally, the detumbling of the second stage, including the magnetic interactions, of a Kosmos-3M rocket is presented in Chapter 7. The conclusion and recommendations of this Thesis can then be found in Chapter 8.

1
PROJECT DESCRIPTION

This thesis will discuss the principles of an Eddy Current Brake (ECB) and the simulation of the braking force induced by the generation of eddy currents when a conductive, uncooperative tumbling object, such as the second stage of the Kosmos-3M, is placed within the magnetic field generated by the ECB. A more in-depth look at the project and how it was chosen, is provided in this Chapter together with the research, modelling and simulation process used to arrive to the final result.

1.1. WHY DETUMBLING IS NECESSARY

The reason why the Thesis focuses on the magnetic interactions of a chaser, equipped with an ECB, and a target, more specifically the second stage of the Kosmos-3M, is already shortly touched upon in the introduction, but will be discussed further to justify the decision to focus on the detumbling of space debris by means of an ECB.

The definition of space debris covers a wide range of objects floating around in space, from truck-sized satellites to shrapnel no larger than a bullet[1–3]. In Chapter 2 more details on what debris is and the debris population is presented, but the most important conclusion is that all space debris is uncooperative, meaning that their state cannot be controlled without external interference (a chaser)[1]. Additionally most of the debris has a very long lifetime and that without an Active Debris Removal (ADR) strategy, they will take decades to re-enter into the Earth's atmosphere[4]. This re-entry will be uncontrolled, resulting in a chance, however small it may be, that some parts will not burn up in the atmosphere and crash in populated areas. Space debris, thus, not only poses dangers in Earth orbit, but also on the surface of our planet.

In order to mitigate these dangers, a combination of ADR and On-Orbit Servicing (OOS) strategies is necessary. A typical ADR or OOS mission first launches a satellite or chaser, which performs a rendezvous with the selected uncooperative object in order to de-orbit it by means of space harpoons, docking, de-orbiting kits, ion-beam shepherd or some other technology[1, 2, 5–10]. After that object has safely been de-orbited, the same chaser moves to the next target. The sequence of the targets that are to be removed or repaired is crucial to a ADR or OOS mission since the targets are always in motion. However, the success or even possibility of most, if not all, techniques heavily depend on the rotation rate of the uncooperative object to be de-orbited[11]. Most research papers have incorporated some sort of rotational rate of their target objects, however, they mostly assume that the debris rotates over one axis and/or they assume a stable target with a low rotational velocity. These assumptions greatly simplify the actual situation in orbit, where objects can rotate at high velocities over multiple axis, making the alignment of the chaser with the target improbable or even impossible[3]. Furthermore, attempting to grab a rotating target can potentially lead to the grappling arms, or other weaker structural elements, breaking, creating more debris in the process, which is the opposite of what the mission tries to achieve.

Therefore, a prior detumbling phase is necessary. Only few techniques have been proposed in order to detumble debris, but the most promising are: using a brush, ECB, detumbling modules, ion-beam shepherd braking and touchless electrostatic detumbling. However, the brush and detumbling modules both have the same problems and limitations as the ADR techniques, such as the creation of smaller pieces of debris and the difficulty to attach a detumbling kit to a rotating target. Analysing the other techniques for reliability, detumbling time, additional debris creating potential and shape and size dependence, shows that ECB is the most promising technique. Touchless electrostatic is discarded because it is not suitable for missions in Low Earth Orbit (LEO), since the technique only works in Geostationary Earth Orbit (GEO), meaning that it cannot remove objects from the most at-risk regions, which will be discussed in Chapter 2[12]. The ion-beam shepherd technique, on the other hand, poses too many technical challenges and is uncertain to be able to actively control the despin of the target, due to the imprecise knowledge of the target, together with imprecise knowledge of the exhaust characteristics and the exhaust deflecting of time-varying surfaces[12].

1.2. PROJECT OVERVIEW

The detumbling of space debris is a necessary step for a wide range of uncooperative objects in LEO before they can be de-orbited by the use of an ADR technique, with ECB being a promising candidate. However, while an ECB is widely used in train brakes, few research has been performed on the matter, which only recently led to some breakthroughs. Therefore, a project overview and delineation of the most relevant research topics needs to be established, in order to maximize the contribution this thesis can make to the simulation of the working of an ECB in near real-life circumstances.

Detumbling an uncooperative object with the use of an ECB poses many challenges and consists of different steps. This thesis will focus solely on the detumbling mission, meaning that the chaser has been launched and performed a rendezvous with the target object, placing it at a fixed distance from the target. Then the ECB is turned on and the detumbling mission starts. The simulation or detumbling mission stops when all angular velocities have converged.

Placing an object in a magnetic field and generating a magnetic field on a chaser creates different challenges and induces different forces. The most important and vital magnetic interaction is the induced torque on the target generated as a result of placing a conductive target, in this case the Kosmos-3M second stage, in a magnetic field, which generates eddy currents and induces a braking force. This torque will be analysed and simulated for objects of different shapes and sizes to finally be able to detumble the second stage of a Kosmos-3M.

The other magnetic interactions include the influence of the Earth's magnetic field and the presence of ferromagnetic materials in the uncooperative objects.

RESEARCH, MODELLING AND SIMULATION PROCESS

Before the magnetic interactions of a target that is actively being detumbled by an ECB on a chaser, can be modelled and simulated, first a basic understanding of what space debris is and why it poses such a danger to current and future space missions is needed. Then the regions in LEO will be listed with the highest risk of having a collision between two uncooperative objects or an uncooperative object and a functioning satellite or other space object. This will provide a basic understanding of the region in which the chaser, equipped with an ECB will operate.

Secondly, a close analysis of the second rocket stages of Kosmos-3M rockets is performed in order to assess their dimensions, rotational motions and more.

After the region and the target object have been defined, the theory behind and working principle of an ECB is discussed, together with a justification of why the magnetic interactions are an ideal candidate for this thesis research, which concludes the background and theoretical framework.

The first step in modelling an ECB is making a preliminary design for the electromagnet and modelling the magnetic field, which will be based on current technology, including High Temperature Superconducting wires (HTS). The model allows to simulate a wide range of magnetic fields, based on different electromagnets, based on size, coil windings and more. Based on launcher capabilities, the maximum dimensions of such a magnet are defined, which, together with the state of current technology are the only limitations placed upon the electromagnets design.

After the model for the magnetic field is completed, different objects are simulated by the use of a frame model, in order to test the basic detumbling of debris of different shapes, namely a sphere, a cylinder and a cylinder with hemispherical ends, named a double silo. Their Magnetic Tensor will be simulated, which represents the objects sensitivity when placed in a magnetic field, allowing for a fast and accurate simulation of the induced torque and thus detumbling time.

After the model for the basic shapes is verified based on past research, the actual shape of the Kosmos-3M rocket will be modelled by the same method. Its Magnetic Tensor will be determined and an initial simulation takes place, investigating the converged rotational velocities and detumbling times.

Up until this point is has been assumed that the chaser consists either entirely out of conductive non-magnetic materials like aluminum or consist of a combination of conductive and non-conductive, such as plastics, non-magnetic materials. However, as will be discussed in Chapter 2, the second stage of the Kosmos-3M has ferromagnetic elements, leading to a change in attitude of both the target debris and the chaser, while they are slowly pulled towards or pushed away from each other. These effects will be studied, mitigation strategies will be examined and if necessary attitude control strategies will be proposed. Furthermore, the influence of the Earth's magnetic field will be analysed, together with other disturbances like the non-uniformity of the generated magnetic field.

Finally, the final detumbling of a Kosmos-3M rocket can be simulated taking into account all magnetic interactions. The final detumbling is presented and the feasibility of using an ECB to detumble upper rocket stages will be discussed. After which a conclusion and recommendations for future research can be made.

2

Background and theoretical framework

This Chapter explains that there is a need for ADR and OOS due to the ever increasing debris population in LEO. The most crowded region in LEO is located around 950 km above the Earth and mostly Kosmos-3M upper stages reside there. These stages are, due to their cylindrical shape and materials, ideal candidates to be detumbled with the use of an ECB. Therefore, this chapter also presents the theory behind an ECB including the necessary equations and tools required to perform eddy current braking.

2.1. Space Debris

Before explaining the research objective more in depth, first a definition of what space debris is and why they pose (are becoming) a major risk for current and future space missions needs to discussed.

2.1.1. Definition

Defining what space debris is, is a complex matter and an agreed upon definition does not even exist. The Inter-Agency Space Debris Coordination Committee (IADC), whose members are all the major Space Agencies, formulated a technical definition of space debris as follows: "Space debris, also known as orbital debris, are all man-made objects, including fragments and elements thereof, in Earth orbit or re-entering the atmosphere that are non-functional"[13].

However, this definition only covers non-functional objects in space and excludes functional but non-manoeuvrable space objects, which can also be classified as space debris[14]. Additionally this definition is not a legal definition, adding another level of complexity to the space debris problem. Laws and regulations, such as outlined in the Outer Space Treaty, will need to be altered before space debris can be removed from orbit en masse[15].

Furthermore, this definition does not include any differentiation between types of space debris. For example, based on different tracking methods space debris can be categorized into different size classes, with each class having a different source providing information about the objects in that class. The objects in the first category, which include launch stages, spacecraft and other debris, are tracked by established surveillance systems. Most of these objects are monitored on a regular basis and are officially catalogued. The second category, which includes fragmentation debris and others, can be detected by ground-based sensors. Efforts are being made to develop a catalogue-like database for this category. And finally the third category's presence is hardest to track and mostly consist of shrapnel. Collisions with space objects that have returned to Earth, can provide some insight in how many of these objects float around[16].

Due to the, relatively, small size of debris in the third category, an ADR strategy to remove debris from this category is improbable. Therefore, most proposed solutions in research papers aim to de-orbit objects from the first two categories and this Thesis will focus on the Kosmos-3M second or upper stage, which is a member of the first size category.

2.1.2. DANGERS AND CONSEQUENCES

The importance of OOS and ADR was already proven by numerous studies as early as the 1980s and even the National Aeronautics and Space Administration (NASA) realized their importance early on[5]. Yet, only recently the awareness of how big a problem it is or could become is growing.

One reason for the increased public awareness is the media covering stories about the dangers of debris colliding with the International Space Station (ISS). Space stations like the ISS have already performed numerous manoeuvres called Just-in-Time Collision Avoidance (JCA) and will be required to do so in the future[17]. However, not only large objects, but also regular sized satellites are affected. Envisat, for example, has seen an ever growing number of warnings between 2009 and 2011, as can be seen from Figure 2.1. This increase in warnings is due to a combination of the improvement of tracking techniques and an ever increasing space debris population in LEO[18]. Additionally, European Space Agency (ESA) lost contact with Envisat in 2012, making Envisat effectively space debris.

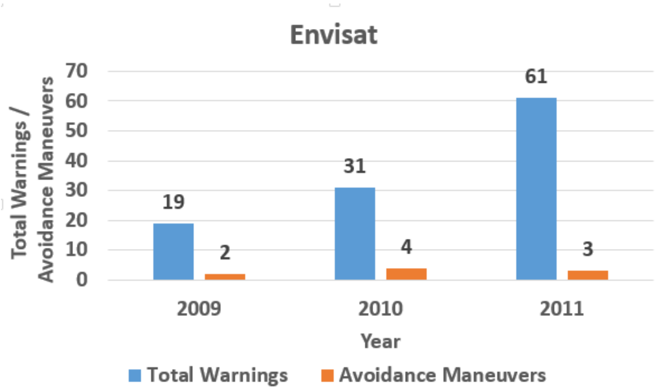

Figure 2.1: Warnings and avoidance manoeuvres Envisat[19]

Since the race to the moon started between the United States of America and the Soviet Union, thousands of satellites have been put in Earth orbits by thousands of launchers and there are no signs that the industry is slowing down, instead it is only accelerating. As already stated, the debris in orbit is steadily increasing over time, but the biggest risk space debris poses is that in-orbit collisions can, have and will generate non-traceable fragments. In recent history there were two events that exponentially increased the number of objects in the third size category and almost doubled the space debris population as a whole. The first being the Chinese Anti-Satellite Weapon (ASAT) test in 2007, which increased the debris population by almost 25%. And the second being the collision of Iridium 33 and Cosmos 2251 in 2009. In Figure 2.2 these two events are clearly visible, with fragmentation debris more than doubling.

The probability of collisions are only increasing and have already seen a dramatic increase over the last years. Not only non-functioning satellites , but also functioning ones are in danger of collisions, due to the many uncooperative objects of the first and second size-categories. In order to stabilize the current environment 5 to 10 objects per year need to be removed, especially in some parts of LEO where we mathematically have surpassed the "critical density"[18].

It can be concluded that in order to assure continued space exploration a space debris reduction program needs to be implemented[20, 21].

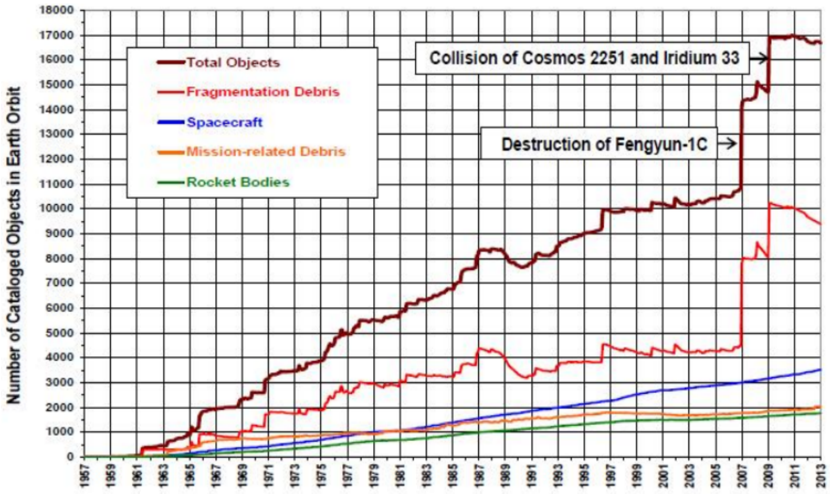

Figure 2.2: History of debris population[18]

2.1.3. CRITICAL ZONES IN LEO

The space debris problem does not also exist in LEO, but also in GEO. However, this thesis will focus on LEO since the most critical regions are located there, with a high spatial ratio of space debris. B. Bastida and H. Krag defined three orbital regions in LEO, which are most critical because of their large concentration of debris[1]. These regions are most likely to trigger the Kessler Syndrome, which is a cascading effect first proposed by Donald J. Kessler in 1978, when he was a NASA scientist. It can be described as the idea that one collision of space debris generates more space debris, which in turn collides with other space debris, until the entirety of LEO is covered with scrap[1].

The three critical regions can be found by using the online Satellite Catalog (SATCAT) as provided by CelesTrak, from which the Two-Line Elements (TLEs) of all present objects in space can be retrieved. This dataset contains only intact objects, i.e. inactive satellites and rocket bodies. Figures 2.3 and 2.4 are a crude representation expressed in % of the spread of debris over LEO in terms of attitude and inclination.

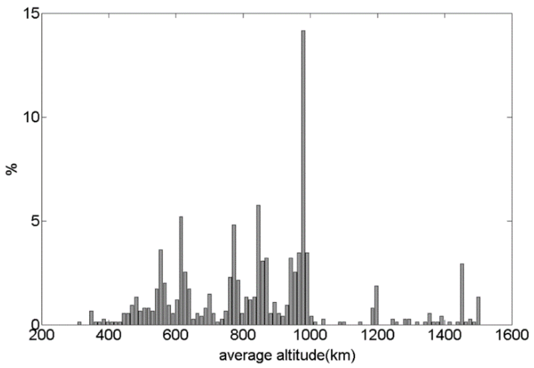

Figure 2.3: Spread of debris in LEO based on altitude[22]

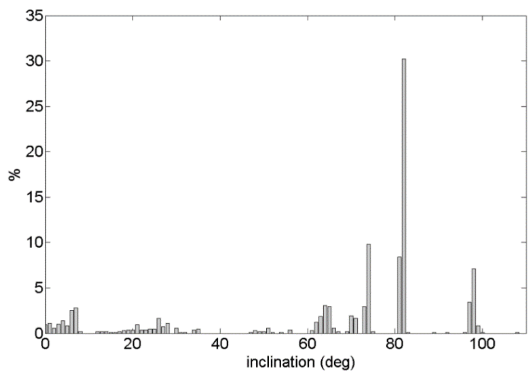

Figure 2.4: Spread of debris in LEO based on inclination[22]

As can be seen from Figure 2.3 the most critical zone lies somewhere between 900 and 1000 km altitude, which has the highest probability that a number of catastrophic collisions will occur in the next 200 years[1]. This region contains 317 objects, most of which are Launch and Mission Related Objects (LMRO's), greatly simplifying the ADR strategy needed, as will be explained in subsection 2.1.4. Many of these objects have a very long lifetime and also belong to the same constellation, while their mass ranges from 500 to 1500 kg[2].

Splitting this region even more, the most critical region is found to be at an altitude between 925 – 999 km with inclinations ranging from 82.83^o to 82.99^o as can be seen in Figure 2.4[4, 23]. This region consists of 135 objects, resulting in the highest spatial density and highest risk of collision. Additionally, this cloud mainly consists of Kosmos-3M upper rocket stages, which simplifies both the legal issues and capture process for ADR.

2.1.4. DEBRIS CHARACTERISTICS AND THE KOSMOS-3M

As discussed in subsection 2.1.3, the most critical region in LEO consists mainly of Kosmos-3M rocket stages. Rocket stages are ideal candidates for ADR and OOS since they have many advantages over non-functioning satellites, such as[2]:

- They have a standard cylindrical or spherical shape
- They have no or few appendages
- They are robust
- They are tolerant to high acceleration loads
- They can be spun to high acceleration rates
- Their center of mass is aligned with the main engine axis
- They have a nozzle extension where a de-orbiting device can easily be installed
- They cannot be confused with functioning satellites
- They are not subject to any confidentiality restrictions

However, even for rocket stages, there are still many uncertainties in the de-orbiting process. For many debris objects no design data is available or they are damaged, and as a result, no detailed mass is available and the inertial characteristics of the target are unknown[11]. As a result, performing ADR is still quite challenging.

Rocket stages are the ideal candidate for a detumbling and subsequent de-orbiting mission, taking into account the advantages LMRO's have compared to non-functioning satellites and the fact that the Kosmos-3M second rocket stages are located in a small critical region in LEO.

In Figure 2.5 the Kosmos-3M rocket is depicted, of which the second or upper stages are located in that critical region in LEO and are orbiting the Earth uncontrolled. The first stages returned back to the surface of the Earth and landed or crashed in non-populated areas right after launch. A real-life Kosmos-3M upper stage can be seen in Figure 2.6, while Figure 2.7 depicts the upper stage in orbit.

Figures 2.5 to 2.7 give us a general idea about the shape and dimensions of the second stage. However, finding detailed information about the materials used, precise size characteristics and more is a challenge since the Kosmos-3M is a Russian rocket and most of the information is in Russian and even some of it is protected. Additionally there are other uncertainties.

For example: not every upper stage will be exactly the same due to manufacturing processes or due to the fact that they have collided with other debris, penetrating it or even tearing parts of. Therefore, in order to compute the other object's characteristics, an idealized model of the Kosmos-3M will be used as is presented in Figures 2.8 and 2.9 to calculate characteristics as Center of Mass (CoM) and moment of inertia matrix, in which all parts of the rocket body are represented as hollow cylinders with a certain thickness, with an evenly distributed mass for each section.

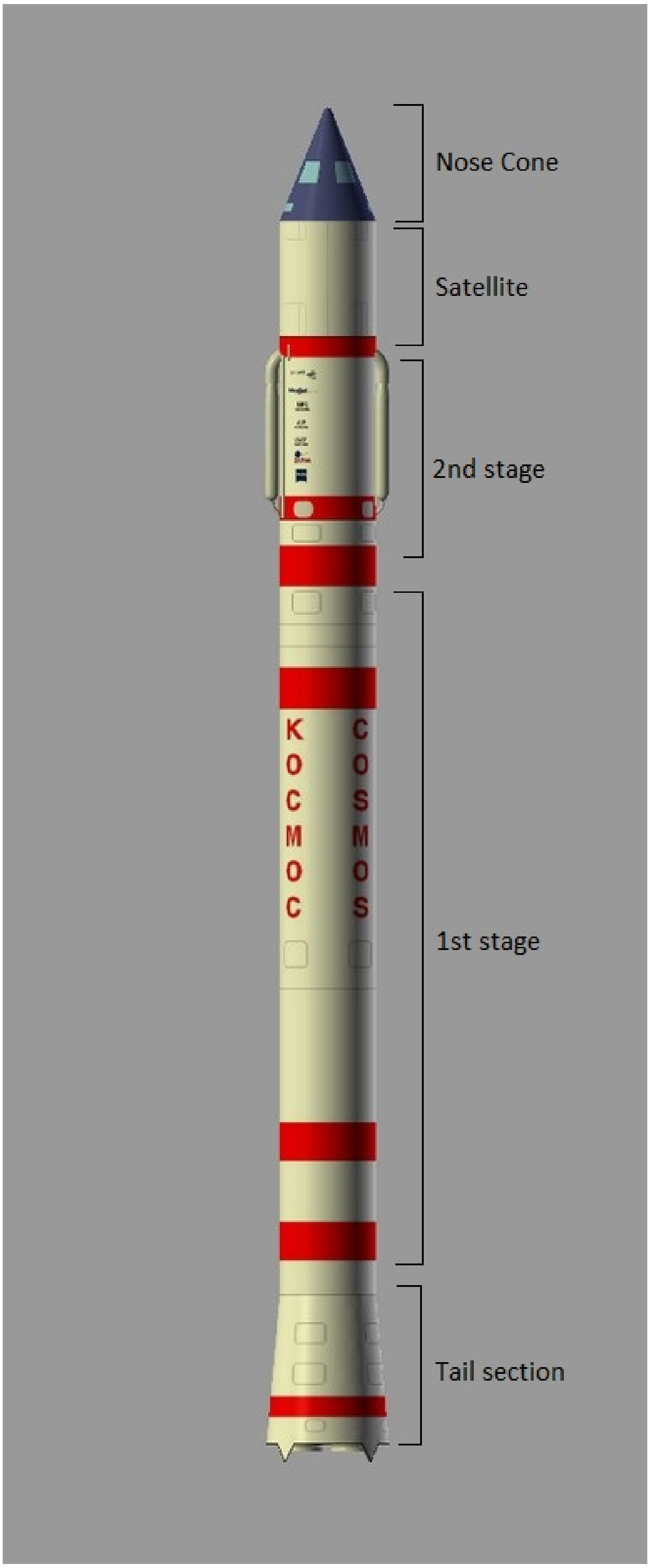

Figure 2.5: Kosmos-3M

Figure 2.6: Kosmos-3M upper stage

Figure 2.7: Komos-3M upper stage in orbit with Rubin 1 mounted on top[23]

In order to model the detumbling of the Kosmos-3M its characteristics need to be known. The data that will be used in this Thesis to model the debris can be found in Table 2.1 and includes parameters like mass, length and mass moment of inertia of the Kosmos-3M second stage, where the rocket body has been broken down into three sections: the propellant cylinder, a thruster combustion section and a nozzle, which is represented in Figures 2.8 and 2.9.

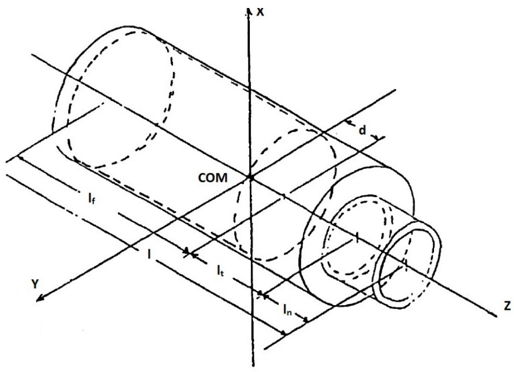

Figure 2.8: Idealized model of the Kosmos upper stage

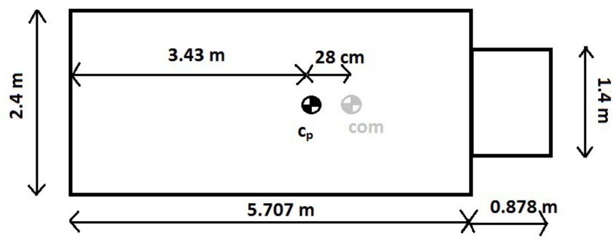

Figure 2.9: Kosmos upper stage centre of pressure and centre of mass

The resulting mass moment of inertia about the x and y axis as depicted in Figure 2.8 can then be found by taking the sum of the mass moment of inertia components as presented in Table 2.1 about the x- and y-axis. The moment of inertia about the longitudinal axis or z-axis as depicted in Figure 2.8, can be found by:

$$I_z = I_{z,t} + I_{z,c} + I_{z,T1} + I_{z,T2} = \frac{m_t R^2}{2} + \frac{m_c}{2}\left(R^2 + R_{in}^2\right) + \frac{m_{T1} R^2}{2} + \frac{m_{T2}}{2}\left(R_T^2 + R_{Ti}^2\right) \tag{2.1}$$

The mass moment of inertia matrix, which represents an important parameter in the detumbling process, of the upper stage then equals:

$$I_{Kosmos} = \begin{bmatrix} 5592.2 & 0 & 0 \\ 0 & 5592.2 & 0 \\ 0 & 0 & 1442.9 \end{bmatrix} kgm^2 \tag{2.2}$$

By combining the mass moment of inertia vector with the angular velocity vector, found through observations, the angular momentum can be computed with the following straightforward relation:

Table 2.1: Parameters idealized model of the Kosmos-3M second stage

Symbol	Description	Value
m_T	Total mass of the rocket stage	1443 [kg]
m_t	Mass of the fuel cylinder top	32.8 [kg]
m_f	Mass of the fuel cylinder	655.9 [kg]
m_{T1}	Mass of the thruster mechanism	655.9 [kg]
m_{T2}	Mass of the nozzle	98.4[kg]
e	Thickness of the fuel cylinder	0.00508 [m]
l_f	Length of the fuel cylinder	4.39 [m]
l_t	Length of the thruster	1.32 [m]
l_n	Length of the nozzle	0.88 [m]
R	Outer body radius	1.2 [m]
R_S	Inner body radius	1.15 [m]
R_T	Outer radius of nozzle	0.7 [m]
R_{Ti}	Inner radius of nozzle	0.6 [m]
d_{com}	CoM from the intersection of the fuel cylinder and thruster mechanism	0.68 [m]
$I_t z$	Mass moment of inertia for the fuel cylinder top	469.7 [kgm^2]
$I_f z$	Mass moment of inertia for the fuel cylinder	3013.5 [kgm^2]
I_{T1z}	Mass moment of inertia for the thruster mechanism	1504.3 [kgm^2]
I_{T2z}	Mass moment of inertia for the nozzle	604.7 [kgm^2]

$$h = I\omega \tag{2.3}$$

Previously in this section it was already discussed that there are still uncertainties concerning the shape, dimensions and materials used due to collisions of the Kosmos-3M second stage with other space debris and an incomplete dataset.

Additionally, objects in space also degrade over time, influencing the shape and thus the detumbling process. The age of Kosmos-3M second stages ranges from 10 years old up until 40 years old, with most of them launched in the 1970's until the 1990's, giving them a higher average age, which, due to outgassing and atomic oxygen, means that the rocket bodies have degraded over time, and will be more fragile than when they were launched, which can play a crucial part in the success of the detumbling mission[2]. For example if the magnetic elements have been degraded, they can be pulled loose when the body is placed in a magnetic field and is therefore an important factor that needs to be taken into account when designing a mission to detumble space debris.

One element of the dataset that is incomplete is the list of materials and their location in the rocket body. The main propellant cylinder is aluminium, but even this big shell contains wiring and other materials[3, 4]. Ferromagnetic materials are bound to be present in an object launched 40 years ago and will influence the detumbling mission due to its interaction with the electromagnet used as an ECB.

Since accurate data is lacking, a conductivity and magnetic ratio will be defined, which will be further discussed in Section 2.2 and will be applied in Chapter 4 and Chapter 6.

2.2. Eddy Current Braking

Before delving into how an ECB works on a mathematical level, the concept will be elaborated upon to create a solid understanding of its working principles and how it can possibly brake the tumbling of an uncooperative object in space. Afterwards, the dynamics needed in order to model the detumbling process will be presented.

The concept of eddy currents and the induced torque created by those currents are based on Faraday's law of induction, which states that by varying the magnetic field with time, an electric current is induced in a conductive loop or coil. This phenomenon is known as electromagnetic induction. Normally, an Electromotive force (emf) is connected to a coil, which generates the current, however, in this example the change of magnetic flux through the coil generates the current and is called an induced emf[24].

Faraday's law of induction states that the induced emf, ϵ, in a coil is proportional to the negative of the rate of change of magnetic flux, Θ_B[24].

$$\epsilon = -N\frac{d\Theta_B}{dt} \tag{2.4}$$

Where N is the number of loops.

Faraday's law of induction, thus, demonstrates that a current is generated in a coil when a magnetic field varies over time. The direction of this induced current can then be found by Lenz's law, which states that the induced current produces magnetic fields which tend to oppose the change in magnetic flux that induces such currents. As a result a magnetic force is generated which opposes the motion[24].

It can thus be concluded that when a conducting loop moves through a magnetic field, a current is induced as a result of changing magnetic flux. When considering a solid conductor, like the Kosmos-3M second stage, the induced current appears to be circulating and is called and eddy current[25].

Eddy currents can be defined as closed loops of induced current circulating in planes perpendicular to a magnetic flux. Thus, eddy currents form when non-magnetic, but conductive object, moves within a static magnetic field. The interaction between the eddy currents and the magnetic field, results in a magnetic force being generated and thus a torque due to the angular velocity of the Kosmos-3M second stages. The red lines in Figure 2.10 represent the eddy currents generated by the magnetic field acting upon the surface, generated by a coil through which a current flows[25].

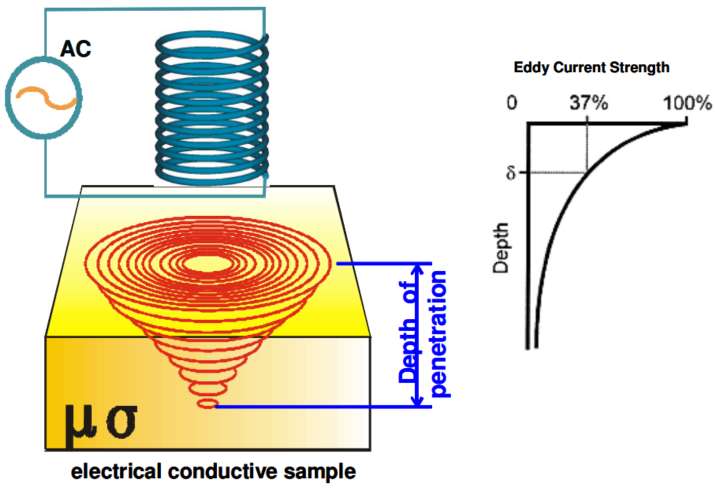

Figure 2.10: Eddy current principle and the skin effect[25]

Furthermore, Figure 2.10 also shows the phenomenon known as the skin effect, which describes how the eddy current density decreases exponentially with depth[25]. This effect will be classified as a perturbation, but due to the small skin thickness compared to the surface area of the Kosmos-3M second stage, this effect will be assumed negligible for the remainer of this Thesis, meaning that the current generated do not diminish with depth due to the electrical resistance in the skin. Future research can be performed to assess if there is any noticeable effect when the skin effect is implemented into the model.

When a rotating object is placed within a magnetic field, eddy currents are generated and an induced torque is created, working in the opposite direction of the rotation and effectively braking the rotational motion. This technique is already used in the braking system of trains, where a magnetic field is applied to a rotating disk (the wheels), which brakes the spinning motion[26].

A schematic representation of eddy currents working on a tumbling uncooperative object can be found in Figure 2.11.

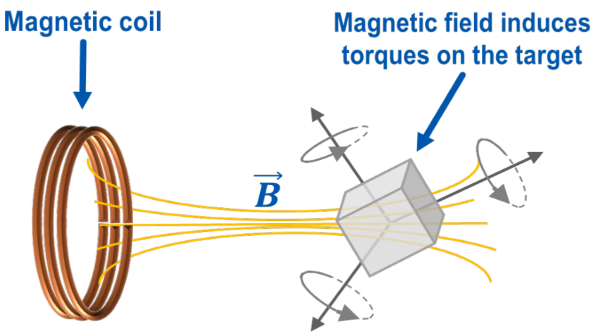

Figure 2.11: A schematic illustration of the detumbling process by using eddy currents[27]

In order to visualize the working principle of an ECB on a rocket body which is rotating over its longitudinal axis a simplified problem set-up is presented in Figure 2.12. In the red circle a simplified uniform magnetic field enters the rocket body from the outside. In order to assess the effect of the magnetic field on the rotating conductive body, four different cases will be looked at where a small portion, of equal size as the area affected by the magnetic field, will enter and then leave the area affected by the magnetic field.

In phase *a*, the circle of skin is not inside the magnetic field and no eddy currents are created.

Phase *b* represents the circle of skin entering the magnetic field. Induced or eddy currents are then created since the circle of skin wants to go back to its previous state (Lenz's law), meaning that it wants to go back to a state where no magnetic fields was present. Therefore, induced currents are created, which generate a magnetic field that cancels the magnetic field working upon it. The interaction of the induced currents with the external magnetic field generates small forces, whose resulting force works in the opposite direction as the rotational motion.

After the piece of skin has passed the magnetic field and has thus been in a state where the area of the magnetic field and the skin area matched, phase *c* begins, which represents the circle of skin leaving the magnetic field. Again, the circle of skin wants to go back to its previous state, which is now to be fully engulfed in a magnetic field. Therefore, induced currents, in the opposite direction of phase *b*, and a resulting magnetic field are created. Similar to phase *b*, the interaction of the induced currents with the external magnetic field generates small forces, whose resulting force works in the opposite direction as the rotational motion.

Finally, phase *d* again represents a moment in time where the circle of skin has left the magnetic field, and no change in state is perceived, thus leading to no eddy currents being created.

Shortcomings of the representation in Figure 2.12 are that it only shows the case where magnetic field lines are going into the cylinder, while they also go out of the back of the cylinder. The induced currents are opposite there, but the forces they create do not cancel the forces, as shown in Figure 2.12, but instead add to those forces, thus only leading to a bigger induced torque. Furthermore, it only shows the case where the debris is rotating over one axis, while there are many potential targets that rotate over multiple axes.

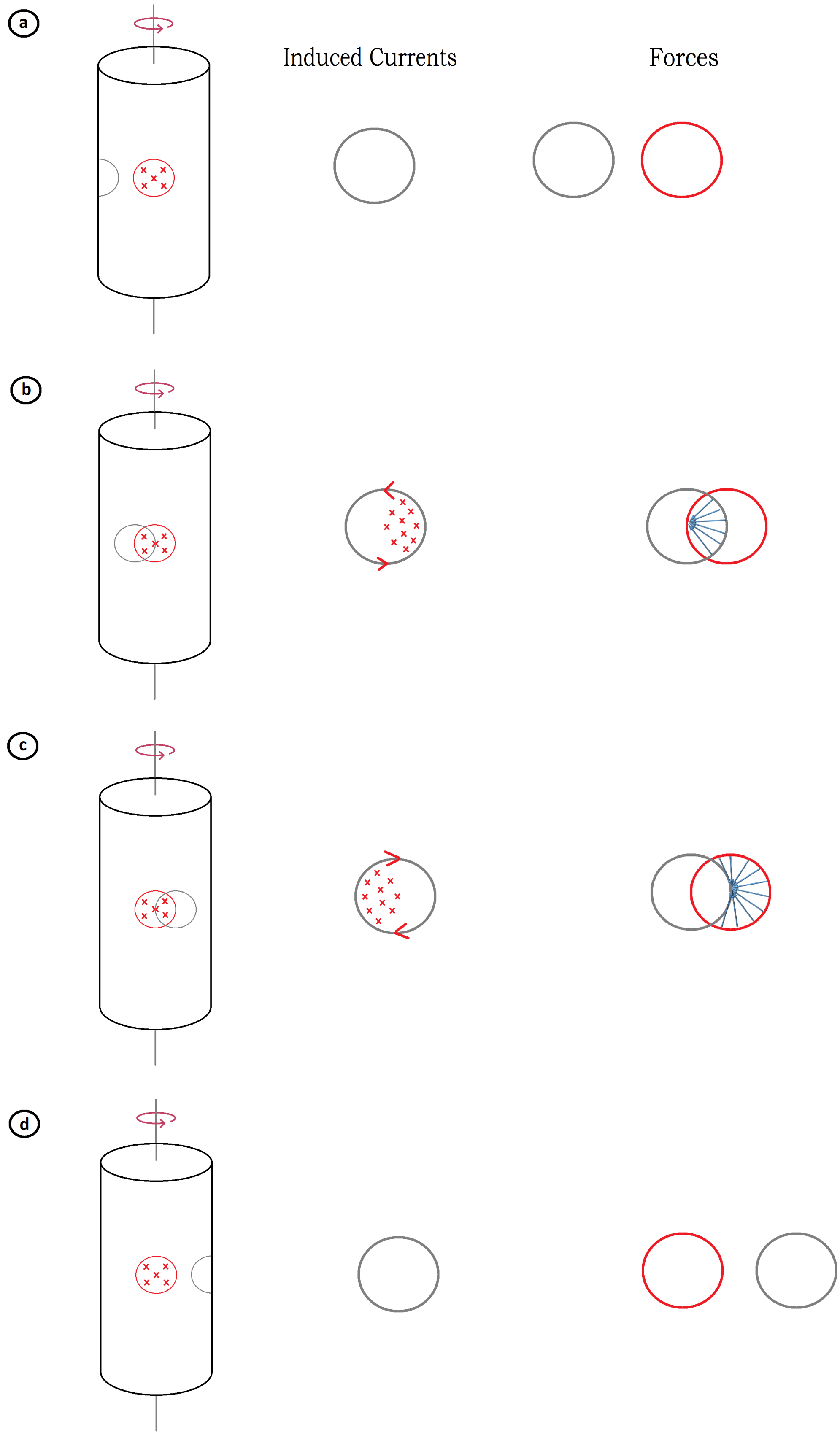

Figure 2.12: Eddy Current Braking on a cylinder rotating about its longest axis

Additionally, research has shown that not only do eddy currents damp the main rotational motion, but can also damp the nutational motion, thus only improving the state of the uncooperative object for capturing[28][29].

Figure 2.13 is a simpler representation of the working principle as shown in Figure 2.12 and visualizes the resulting force.

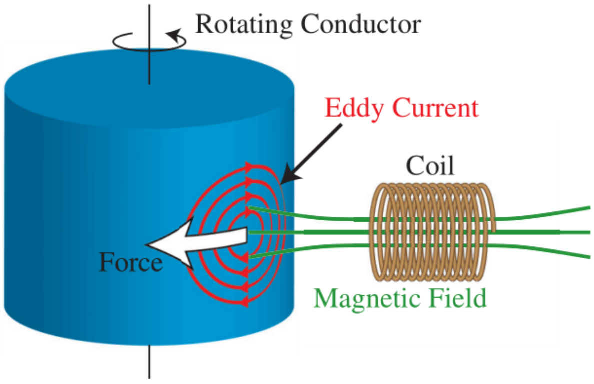

Figure 2.13: Simplified representation of working principles eddy current brake [30]

2.2.1. ELECTROMAGNETS AND THE MAGNETIC FIELD

Before discussing the working principle of the ECB more in depth, first the magnetic field in which the rocket body is placed or which is placed upon the rocket body, needs to be discussed.

Due to the size of the Kosmos-3M upper stages and other potential targets, a strong magnetic field will be needed to be able to detumble the debris in a reasonable amount of time.

A magnetic field can either be trapped or generated. The first option is to use a trapped magnetic field, which does not need an external energy source to operate. Recently a trapped field of 17.6 Tesla has been achieved with two stacked superconducting bulk samples of 25 mm diameter, which is not only lightweight, but also very small in size[31]. Its small size is a big advantage since it is easier to launch, operate, etc. However, the downside of using a trapped magnetic field is that it cannot be turned off, and as a result could affect the orbits of other missions, detumble functioning objects and even attract small pieces of debris, which could possibly penetrate the active chaser. Therefore, a trapped magnetic field is not considered to be a viable option.

The second option to generate a magnetic field is by using electromagnets, of which many different types exist. A disadvantage is that an electromagnet needs an external power source, which needs to be delivered by an on-board power source, possibly shortening the mission lifetime.

The ECB used in train brakes uses electromagnets. Since the objects that need braking (the wheels) are relatively thin, a near-uniform magnetic field can be easily generated, which increases the effectiveness of an ECB. However, in order to create a near uniform magnetic field big enough to engulf a rocket body as large as the Kosmos-3M second stage is nearly impossible. The first option would be to place two equal electromagnets on either side of the debris, similar to a Helmholtz coil, which thus allows a near uniform field to be generated[32]. Another option is to have the debris sit in the center of the electromagnetic coil, where the magnetic field is uniform and strongest. However, for both cases, creating such an electromagnet is impossible due to the high mass and volume requirements of an electromagnetic coil. Launching such a mission, with a coil having a diameter that exceeds 11 meters, is not feasible and is outside the limits of current launching capabilities. As an alternative, deployable coils are being investigated which could possibly allow for coil with a large enough diameter to be launched[28]. However, for the purpose of this Thesis, it will be assumed non-feasible since the technology is not currently available.

It can be concluded that the simplest and most straightforward approach to create a magnetic field is to use a single coil electromagnet and aim it at the target from a certain distance as represented in Figure 2.13. However, the challenge here is that the magnetic field created needs to be strong enough to detumble the rocket body in a reasonable amount of time. Therefore, superconducting coils will be used.

Superconducting magnets are already used in Magnetic Resonance Imaging (MRI) scanners, but most can only operate at temperatures close to 0 Kelvin. And while in space it can get as cold as 2.7 Kelvin, in Earth orbits this is certainly not the case.

Recent progress has seen superconducting magnets operate at higher temperatures, which are called HTS, which can operate at a temperature of up to 77 Kelvin, producing a magnetic field between 5 and 32 Tesla and have a weight up to 2300 kg[33]. The size and weight of the superconducting magnet will thus play an important role in the range of magnets that can be used for space missions.

While superconducting magnets are not yet used for a purpose similar to a space ECB, a recent study at European Space Radiation Superconducting Shield (SR2S), in cooperation with European Organization for Nuclear Research (CERN), is developing a superconducting magnet to protect astronauts from cosmic radiation. The superconducting coils for their prototype are made of magnesium diboride,MgB_2, which is the same type of conductor that was developed for a project at CERN's Large Hadron Collider. The biggest advantage of using MgB_2 is that it can operate at high temperatures of up to about 40 Kelvin[34][35][36].

As already stated, a superconducting magnet operates at temperatures of about 0 Kelvin. In space it can get as cold as 2.7 Kelvin, but in LEO the chaser can get as hot as 395 K when in direct sunlight, but also as cold as 116 K when in the shade[37], which is nowhere near the operating temperature. Therefore, the electromagnet will need to be cooled actively to cryogenic temperatures during operation and/or should passively be shielded against radiation. The temperature differences in orbit will also depend on the speed of the chaser and thus the target. A faster orbital velocity results in a steadier temperature, which means a lower temperature difference overall, simplifying the cooling process. However, the orbital velocity strongly depends on the orbital velocity of the target.

Actively, the electromagnets could be cooled by cryogenic liquids[38], but these require additional subsystems in the chaser, adding to the complexity, and are limited resources, meaning that when the cryogenic liquids run out, the mission ends.

In order to shield the coils (passive cooling), they can be insulated. Traditionally, space missions are equipped with insulation, protecting the vulnerable parts within. As a result, only the outer layers of the insulating blankets are affected and not the craft itself[39]. But completely insulating a thin magnetic coil that is always outside of the body of the chaser is difficult. Additionally, in order to get more concentrated magnetic flux lines, the electromagnetic coils need to be wound with very close spacing. Thus adding more insulation will increase the spacing and thus decrease the effectiveness of the magnet, leading to longer detumble times. Most current electromagnetic coils are coated with enamel insulation[40], but in space mylar, which is used in space blankets, could also be used to seal it from radiation[41].

Furthermore, the instruments on the chaser also need to be protected from the magnetic field it creates. The electric magnet or coil will either be held by a robotic arm or similar deployable structure, or be part of the rigid structure of the chaser. The latter will require shielding of sensitive instruments on the chaser with ferromagnetic material, while the former adds another level of complexity to the chaser[42]. For the purposes of this Thesis the electromagnet will be assumed to be held by a robotic arm at a certain distance from the main body.

The working principle and magnetic field that can be created will be discussed in more depth in Chapter 3.

2.2.2. CONDUCTIVITY OF TARGETS

In Section 2.1 it was explained that few information is available about the materials used in the Kosmos-3M upper stages. However, these materials will influence the detumbling process greatly. In order to find a good estimation of the types of materials in the rocket body, the ratio of conductive materials versus total mass is introduced, where the conductive materials are typically aluminium or titanium alloy. When comparing different upper stages of different rockets, it can be found that they typically have a ratio of conductive material of about 30%[28]. This ratio will be used in order to model the detumbling process and will be extended upon in Chapter 5.

In order to evaluate the influence of the conductivity ratio, the characteristic time of decay is introduced for an uncooperative object with the shape of a spherical shell[28]:

$$\tau = \frac{4\rho_c}{\sigma B^2}\left(1 + \frac{3}{5}\frac{m_{nc}}{m_c}\right) \tag{2.5}$$

Where B is the magnetic field, σ is the conductivity of the sphere, ρ_c is the skin density, m_{nc} is the total mass of non-conductive materials and m_c is the total mass of conductive materials in the rocket body.

Figure 2.14 shows the influence of this ratio on the characteristic time of decay for a spherical shell.

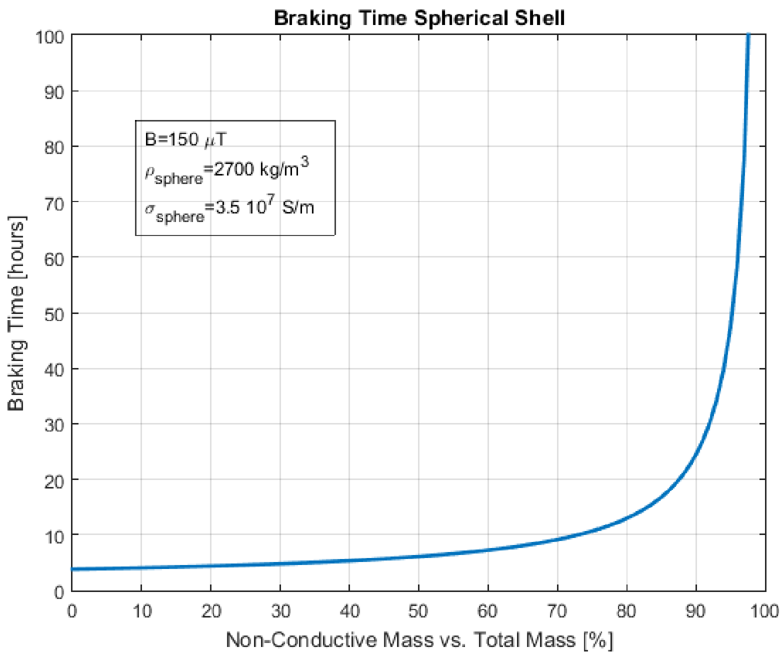

Figure 2.14: Braking time for a spherical shell for different ratios of conductive material[28]

It can be concluded that for an ECB to be feasible, the targets need to have a relatively high conductive material to mass ratio. Preferably uncooperative objects with a ratio of more than 25% or higher should be targeted, making rocket bodies the perfect targets to be detumbled by an ECB.

2.2.3. DYNAMICS OF AN EDDY CURRENT BRAKE

After the basic working principle of an ECB has been explained, a more in depth analysis of the dynamics involved can be presented.

First of all it is important to know which parameters influence the resulting braking force, as mentioned earlier, on the rocket body. The force, applied to the rotating object, as a result of eddy currents, is related to the current in the electric magnet, I_0, the windings of the electric magnet,

n_e, the velocity of the electric magnet, v, and the distance between the coil and the object, x, as follows[30]:

$$f \propto v, \frac{1}{x^2}, I_0^2, n_e^2 \tag{2.6}$$

Modelling the eddy current torque for different shapes and sizes has proven difficult. A general way to evaluate the torque is to use a Finite Element Method (FEM) to divide the volume into a grid and solve the Laplace equation with Neumann conditions. However, it is not practical to solve this problem for each time step and some of these calculations possibly need to be run on-board of the chaser and need to run in near-real time.

An alternative is to use specific formula's which represent the resulting force as a function of the specific shape of the uncooperative object. However, only for a limited range of shape and sizes and specific orientations of the angular velocity vector $\vec{\omega}$ and the Magnetic Field $\vec{B}$ analytical solutions of the eddy current torque have been found[43, 44].

For a spherical shell, the analytical solution of the induced eddy current torque is[43]:

$$\vec{T} = \frac{2 * \pi}{3} \sigma R^4 e (\vec{\omega} \times \vec{B}) \times \vec{B} \tag{2.7}$$

Where R is the radius of the spherical shell, B is the magnetic field, e is the thickness of the shell and σ is the electrical conductivity.

And for an open cylindrical shell, the analytical solution of the induced eddy current torque is[44]:

$$\vec{T} = \pi \sigma B_x \omega R^3 e L \left(1 - \frac{2R}{L} \tanh\left(\frac{L}{2R}\right)\right) \left(B_x \vec{i} - B_z \vec{k}\right) \tag{2.8}$$

Where R is the radius and L the length of the cylinder, e is the thickness and σ is the electrical conductivity.

However, since the object to be detumbled, the Kosmos-3M upper stage, is neither a sphere nor a cylinder, the model to simulate the detumbling process will not make use of these analytical expressions. Instead they will be used to verify the model.

A more promising technique to model the detumbling process of complex shapes is the one developed by N.O. Gomez, namely the Magnetic Tensor, M. This technique also uses a FEM technique, but only at the first time step in order to model the shape of the target, after which only matrix divisions or multiplications are necessary. By introducing a Magnetic Tensor, which describes how a conductive object will react when it is placed in a magnetic field, the complex and time intensive Laplace equation with Neumann conditions can be avoided. Therefore, the Magnetic Tensor technique will be used in this thesis due to its relative simplicity and low computation time.

In order to model the Magnetic Tensor and subsequent induced torque, the target's shape needs to be modelled by use of a frame model.

THE FRAME MODEL AND MAGNETIC TENSOR

The easiest way to model a target's shape, size and characteristics, is to make a simplified frame model of the target to be detumbled, with the possibility to add complexity afterwards.

A frame model can be seen as a simple FEM model, where a rigid body is divided into m bars and n nodes. Each bar has a length L_k, a conductivity σ_k and a cross section A_k[28]. A constant D_k, which is a combination of the conductivity, cross section and length of a bar can then be defined for each bar k as:

$$D_k = \frac{\sigma_k A_k}{L_k} \tag{2.9}$$

A visual representation of a frame model can be found in Figure 2.15.

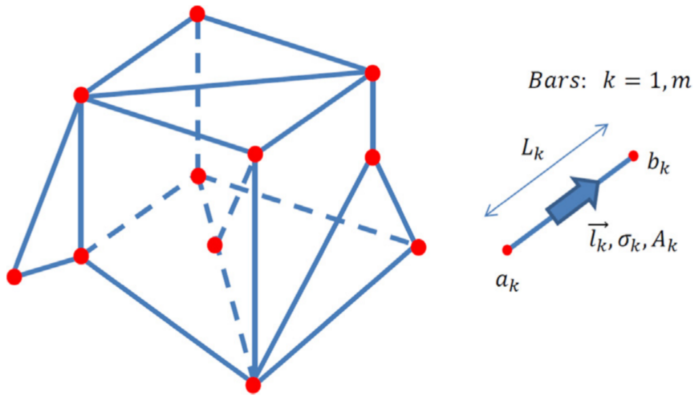

Figure 2.15: Frame model[28]

Only by increasing the number of nodes in the model does the accuracy of the model increase. As a result, the accuracy of the simulation of an ECB working on that model also increases, until it converges.

In order to find the Magnetic Tensor, M, the electric intensity of each bar, J_k, needs to be defined, which relates to the Magnetic Tensor as follows:

$$\vec{\Omega}^t M \vec{\Omega} = \sum_{k=1}^{m} \frac{J_k^2}{D_k} = J^t D^{-1} J \tag{2.10}$$

Where $-\vec{\Omega}^t M \vec{\Omega}$ is the dissipative energy per unit time due to the eddy currents, $\vec{\Omega} = \vec{\omega} \times \vec{B}$ is the electrical current density vector, $\vec{B}$ is the magnetic field vector and $\vec{\omega}$ is the rotation vector.

In order to find the electric intensity of each bar, first the coordinates of the center of the target need to be defined. Then each bar can be assigned a local coordinate l_k, and a center of gravity given by the position vector $\vec{r_k}$.

$$\vec{r_k} = \vec{L_k}/L_k \tag{2.11}$$

Then, the electric intensity of each bar, J_k, is the product of the electric current density j_k and the cross sectional area of the bar.

$$J_k = A_k j_k \tag{2.12}$$

A general solution for the current density vector $\vec{j}$, can be found to be[28]:

$$j_k = \vec{j_k}\vec{l_k} = D_k \left[\frac{1}{2} (\vec{r_k} \times \vec{L_k}) \vec{\Omega} - \Delta\phi_k \right] \tag{2.13}$$

Where $\phi_k = \phi_b k - \phi_a k$ is the effective potential difference between the nodes a_k and b_k of bar k.

Equation (2.12) can be rewritten as a matrix so it accounts for all bars as follows:

$$J = D\left(\frac{1}{2} S\,\vec{\Omega} - \Delta\phi\right) \tag{2.14}$$

Where J becomes a vector $(m \times 1)$ with the intensities of each bar. D is a diagonal matrix $(m \times m)$ with $D = diag(D_k)$, S is a matrix $(m \times 3)$ that contains the cross product $\vec{r_k} \times \vec{L_k}$ and $\Delta\phi$ is a vector $(m \times 1)$ that contains the effective potential difference.

This results in a linear system of n equations with m unknown variables. Introducing a matrix H which links all the bars, the linear system can be expressed as follows:

$$H.J = 0 \tag{2.15}$$

$$\Delta\phi = -H^T\phi \tag{2.16}$$

And J can then be found to be:

$$J = \frac{1}{2}(I - D\,F)D\,S\vec{\Omega} \tag{2.17}$$

Where:

$$F = H^T K^{-1} H = H^T\left(HDH^T\right)^{-1} H = F^T \tag{2.18}$$

Finally, the Magnetic Tensor can be found by filling in Equation (2.17) into Equation (2.10):

$$M = \frac{1}{4}S^T D(1 - FD)D^{-1}(I - DF)DS \tag{2.19}$$

From Equation (2.19) it is clear that the Magnetic Tensor only depends on the geometry and conductivity of the target and has dimensions of $[S.m^4]$, where S is the Siemens unit. The magnetic tensor is a 3x3 matrix. A special property of the Magnetic Tensor occurs when the object can be mirrored over all three axis, making the Magnetic Tensor a diagonal matrix, which will be used to test the model in Chapter 4:

$$M = \begin{bmatrix} M_1 & 0 & 0 \\ 0 & M_2 & 0 \\ 0 & 0 & M_3 \end{bmatrix} Sm^4 \tag{2.20}$$

The Magnetic Tensor can then be used to find the force and the induced torque on the target as the result of an ECB. The eddy current torque can be expressed as the cross product of $\vec{m}$ and $\vec{B}$, where magnetic moment vector, $\vec{m}$, can be found by finding i-component m_i of the magnetic moment by[28]:

$$m_i = \sum_{j=1}^{3} M_{ij}\Omega_j \tag{2.21}$$

The induced torque then equals:

$$\vec{T} = \left(M\vec{\Omega}\right) \times \vec{B} = \vec{r} \times \vec{r} \tag{2.22}$$

Where $\vec{f}$ is the force vector and r is the position vector from the point where the force is working relative to the axis of rotation.

In order to better grasp the different aspects of detumbling a conductive target with the use of an ECB and provide a proof of concept, an experimental approach is presented.

AN EXPERIMENTAL APPROACH

An experimental approach to detumble an uncontrolled satellite with a contactless force by using an ECB has been executed by F. Sugai, et al and will be used to prove that the theory presented does work in real-life applications[29, 30]. The goal of this experimental approach is to show that the Climate Satellite Himawari 5 can be detumbled using an ECB.

This satellite has a mass of 345 kg, a diameter of 2.15 m and a height of 3.54 m.

In order to prove the Climate Satellite Himawari 5 can be detumbled with the use of an ECB, an experimental set-up was used, which can be found in Figure 2.16, where an ECB acts upon a tumbling target, which is a hollow cylinder. More specifically, an aluminium plate with a width of 50 mm and a thickness of 0.5 mm was affixed to an acrylic cylinder. The acrylic cylinder was set on a one axis spinning motion table, which spun the cylinder up to 3π rad/s with constant acceleration. Furthermore, instead of an electromagnet, three permanent magnets were used, which were placed in a row at a distance of 1 mm from the aluminium plate[29, 30].

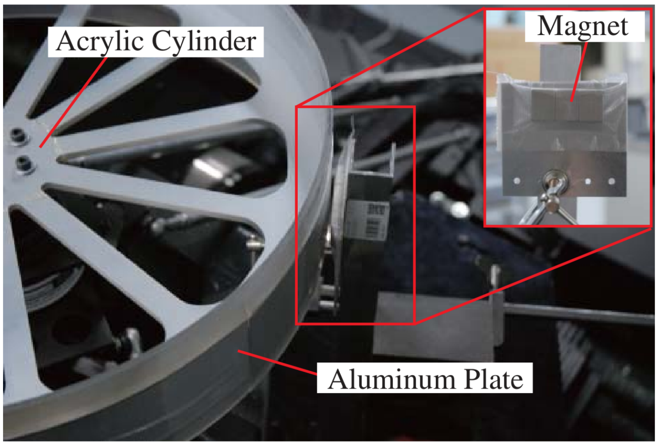

Figure 2.16: Experimental set-up

Since the cylinder in the experimental set-up is not rotating in free space, but instead being spun up at constant acceleration to an angular velocity of 3π rad/s, the torque was measured for the case with and without the magnets. Without magnets only anti-torque was measured, while with magnets a maximum torque of 0.13 Nm was observed, which can be seen in Figure 2.17.

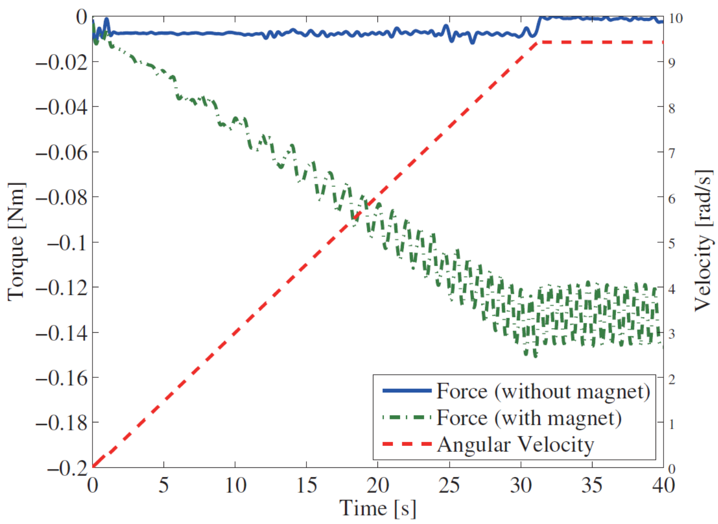

Figure 2.17: Experimental Torques[29]

Furthermore, as can also be seen from Figure 2.17, does the induced torque linearly increases with angular velocity.

F. Sugai, et al then translated the experimental result into a simulation to detumble the Climate Satellite Himawari 5[29, 30]. As initial conditions, the target was rotating at a spin rate of 100 rpm and has a nutation angle of 30 degrees, which is represented in Figure 2.18. Then, assuming the magnets have the same capabilities as those in the experimental set-up, **??** shows that the total angular velocity converges to zero after a little more than 5 hours, with the angular velocity rapidly decreasing when the nutation angle has converged to zero.

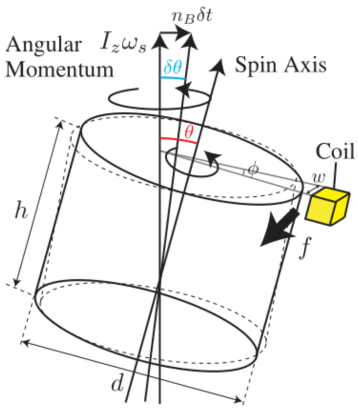

Figure 2.18: Tumbling target with Eddy Current Brake[30]

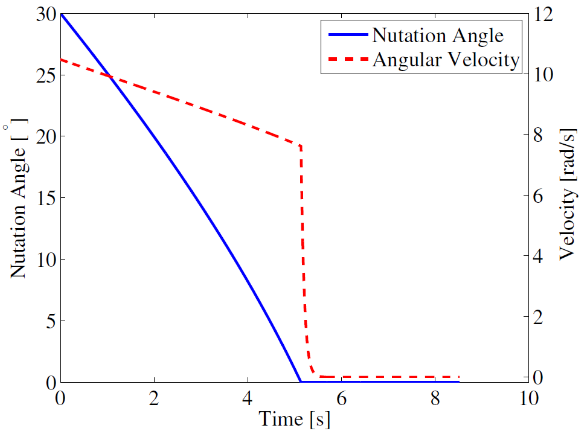

Figure 2.19: Simulation result

The experimental approach, thus, proves that a large object can be detumbled with the use of an ECB even when it is tumbling over multiple axes.

However, due to an incomplete dataset, the results presented by F. Sugai, et al, are only used as a proof of concept in this thesis.

3

MAGNETIC FIELD MODEL

In Section 2.2 it was concluded that an electromagnetic HTS coil is the ideal candidate to generate the magnetic field. More specifically magnesium diboride will be used as the material for the coil. This Chapter will model the magnetic field with the general relation of the vector magnetic field of a circular current loop as developed by R. A. Schill[45], which allows for a variety of electromagnets to be designed. Based on the maximum coil radius, critical current density of MgB_2, and number of loops, the configuration of the coil which generates the strongest magnetic field, will have a diameter of 1 meter, 500 windings and a current of 68.5 Ampere, which leads to a magnetic field of around 0.022 Tesla being created at the center of the coil. This design is within the power, size and weight constraints and will be used to detumble the Kosmos-3M second rocket stage.

3.1. GENERAL RELATION FOR THE VECTOR MAGNETIC FIELD OF A CIRCULAR CURRENT LOOP

In order to model the magnetic field, generated by a circular current loop, first a coordinate system needs to be defined. A cylindrical coordinate system is chosen because of the circular shape of the coil. The cylindrical coordinate system,(r_c, Φ, z), will have the loop axis of the coil along the z-axis in the $z = z_0$ plane, where the current I_0 is oriented to flow in the Φ direction.

An important characteristic that influences the magnetic field generated, is the permeability of free space, μ_0, which is a global variable and for use of an ECB in LEO will be assumed to be[45]:

$$\mu_0 = 4\pi\ 10^{-7} \tag{3.1}$$

In order to model the magnetic field, the procedure as described in Figure 3.1 will be used.

As can be seen in Figure 3.1 the first step in modelling a magnetic field is generating a mesh, which defines the spatial density of the model, after which the radial component r_c can be calculated for every point in the mesh.

$$r_c = \left((x - x_c)^2 + \left(y - y_c\right)^2\right)^5 \tag{3.2}$$

Where x_c, y_c and z_c are the coordinates of the coils center point and are assumed to lie at the center of the mesh for this model.

Then, the radial component and the z-component of the magnetic field can be found:

$$B_{r_c}(r_c, \phi, z) = \frac{\mu_0 I_0}{2\pi} \frac{(z - z_c)}{r_c \left[(r_c + a)^2 + (z - z_c)^2\right]^{\frac{1}{2}}} \left[-K(k_c) + \frac{r_c^2 + a^2 + (z - z_c)^2}{(r_c - a)^2 + (z - z_c)^2} E(k_c)\right] \tag{3.3}$$

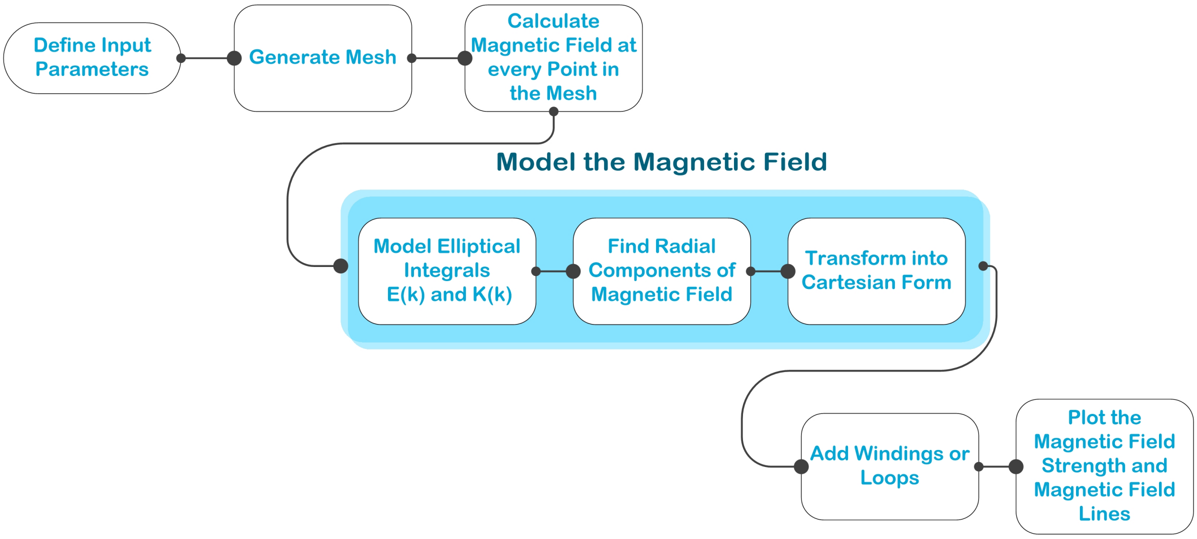

Figure 3.1: Magnetic field modelling procedure

$$B_z(r_c,\phi,z) = \frac{\mu_0 I_0}{2\pi\left[(r_c+a)^2+(z-z_c)^2\right]^{\frac{1}{2}}}\left[K(k_c) - \frac{r_c^2-a^2+(z-z_c)^2}{(r_c-a)^2+(z-z_c)^2}E(k_c)\right] \tag{3.4}$$

Where $K(k)$ and $E(k)$ are the elliptic integral function of the first and second kind and a is the coil radius.

In order to convert the radial components into Cartesian form the following relationships can be used:

$$B_x = B_{r_c}\frac{x-x_c}{r_c} \tag{3.5}$$

$$B_y = B_{r_c}\frac{y-y_c}{r_c} \tag{3.6}$$

As a result the magnetic field vector and strength are modelled for every point on the mesh when a current loop is placed at the center of the mesh.

In order to find the magnetic field generated by a coil with multiple loops or windings, the components of the magnetic field, B_x B_y and B_z, are either multiplied times the amount of loops or each winding is represented as a separate current loop, which are placed at a fixed distance from each other. For the sake of simplification, the magnetic field will be multiplied times the number of windings.

The model as presented in Figure 3.1, now needs to be verified. However, in order to model the magnetic field vectors and strength, first the different parameters that influence it need to be presented:

- The coil radius a
- The coil current I_0
- The coordinates of the coils center point x_c, y_c and z_c
- The amount of loops n_e
- The spacing of the windings l_{sp}

The magnetic field model needs to be able to easily simulate a large range of magnetic fields based on these parameters. In order to limit the amount of design possibilities, design ranges for every parameter will be introduced.

Firstly, the design range for the coil radius, a, is influenced by the launch capabilities of the launchers. In Section 2.2 it was mentioned that expandable coils were being researched. However, it was chosen that in this Thesis expandable coils will not be used in order to give a more realistic representation of the working of an ECB. Therefore, the upper limit of the coil radius is chosen to be 1 meter, while the lower limit is chosen to be 0.2 meter, since it needs to be large enough to create a magnetic field of relative strength.

Secondly, the coil current is limited by both the material of the coil and the power source on the chaser. Since the coil will be HTS, there exists a critical current density, where the superconductor starts to act like a normal conductor. This is due to the fact that magnetic fields kill superconductivity, meaning that a superconductor has a critical field strength at which it becomes a normal conductor. The critical current and critical current density can be found in Equations (3.7) and (3.8) [46].

$$I_c = 2\pi a B_c \tag{3.7}$$

$$J_c = 2\frac{B_c}{a} \tag{3.8}$$

$$B_c = B_c(0)\left[1-\left(\frac{T}{T_c}\right)^2\right] \tag{3.9}$$

Which is thus dependent on the coil radius, a, and on the critical magnetic field, B_c, the operating temperature, T, and the critical temperature of the coil, T_c[46].

The critical magnetic field, thus, is heavily dependent on the effectiveness of the cooling system.

The coordinates of the coil center point will be, for simplicity, chosen to be $(0,0,0)$.

The design range for the amount of loops, n_e, is limited by weight, size and manufacturing constraints.

And finally the spacing of the windings will, as discussed in Section 2.2, need to be kept as small as possible and are dependent on the coating used for the wires in order to keep the HTS in operating temperature. This design space will range from zero to several millimetres.

In order to verify that the model for the magnetic field is correct, the magnetic field strength of the model for different mesh points will be compared to the magnetic field strength computed using another approach.

First, the magnetic field strength at the center of the loop, which coincides with the (0, 0, 0) point of the mesh, can be verified by using the Biot-Savart law for a magnetic field from a current element[47]:

$$dB = \frac{\mu_0 I_0 dL \sin\theta}{4\pi a^2} \tag{3.10}$$

Which can be simplified because the angle θ is 90 degrees for all points of the mesh and the distance to the field point is constant[47]:

$$B = \frac{\mu_0 I_0}{4\pi a^2} 2\pi a = \frac{\mu_0 I_0}{2a} \tag{3.11}$$

The parameters in Table 3.1 are then used as input for model as described in Figure 3.1 and Equation (3.11) for the verification of the magnetic field strength at the center of the coil.

For the model, the magnetic field in the center of the mesh, which is also the center of the coil, is compared to the value found by Equation (3.11). Both lead to a value of 3.141610^{-4} Tesla, which is exactly π to the power minus four, which is due to the fact that the permeability of free space is

Table 3.1: Input parameters verification magnetic field model

a	2	[m]
I_0	1000	[A]
n_e	1	[-]
l_{sp}	0	[m]
(x_c, y_c, z_c)	(0,0,0)	[m]

dependent on π. It can thus be concluded that the magnetic field strength calculated by the model at the center of the mesh and thus the coil, is verified.

In Chapter 2 it was defined that the electromagnet will be placed at a certain distance from the Kosmos-3M second rocket stage. Therefore, the magnetic magnetic field strength modelled at a certain distance from the center of the coil needs to be verified.

In the model and the mesh, the magnetic field lines are assumed to be flowing through the current loop from the negative to the positive z-axis.

In order to find the magnetic field strength of a current loop at a certain distance along the z-axis from the center of the coil, the Biot-Savart law for the z-component can be used[47, 48]:

$$dB_z = \frac{\mu_0 I_0 dL}{4\pi} \frac{a}{\left(z^2 + a^2\right)^{\frac{3}{2}}} \tag{3.12}$$

Where only the distance element dL is not constant, leading to:

$$B_z = \frac{\mu_0}{4\pi} \frac{2\pi a^2 I_0}{\left(z^2 + a^2\right)^{\frac{3}{2}}} \tag{3.13}$$

Again using the parameters in Table 3.1 and varying the distance, z, the model can be verified by comparing the value found by the model at a distance, z, to the values found by Equation (3.13). The results of the verification can be found in Table 3.2.

Table 3.2: Input parameters verification magnetic field model along the z-axis

z [m]	Model [T]	Biot-Savart [T]
2	$1.107\ 10^{-4}$	$1.107\ 10^{-4}$
4	$2.8099\ 10^{-5}$	$2.8099\ 10^{-5}$
6	$9.9346\ 10^{-6}$	$9.9346\ 10^{-6}$
8	$4.4820\ 10^{-6}$	$4.4820\ 10^{-6}$

The values generated by the model and values from the Biot-Savart equations match perfectly. It can thus be concluded that the model is verified, meaning that it can be used for the modelling of the magnetic field for an ECB.

3.2. THE DESIGN OF AN HTS COIL AND ITS MAGNETIC FIELD

In Section 3.1 the design ranges for the different input parameters of the model for a HTS coil were discussed. In order to design an electromagnetic HTS coil that can generate the strongest magnetic field within the design ranges of the input parameters, these parameters need to be discussed more in-depth.

In order to design an electromagnet, first the material of the electromagnetic coil needs to be chosen. The material magnesium diboride, MgB_2 is chosen as a baseline, as discussed in Chapter 2, which has a critical magnetic field strength at zero Kelvin $B_c(0)$ of 14.8 Tesla and a critical temperature of 39 Kelvin [49], after which it is no longer a superconductor. From these data, the critical magnetic field strength and critical current can be found, which are dependent on operating temperature and the material used. For this thesis, an operating temperature of 20 Kelvin is chosen, since only current technology HTS coils will be used and in order to achieve a strong magnetic field. In order to achieve a temperature of 20 Kelvin, the electromagnetic coil needs to be cooled with passive and active cooling systems.

The critical current and accompanying critical magnetic field strength in terms of the coil radius can then be computed by using Equations (3.7) and (3.9).

If the maximum value of the design range of the diameter is used, 2 meters, then the critical current density is around 68.5 Ampere. Furthermore, based on literature, the number of windings is chosen to be 500[28]. The input parameters for the model for configuration A, which is the maximum configuration, can then be found in Table 3.3.

Table 3.3: Input parameters magnetic field model for configuration A

a	1	[m]
I_0	68.5	[A]
n_e	500	[-]
l_{sp}	0	[m]
(x_c, y_c, z_c)	(0,0,0)	[m]

The spacing of the windings will thus be assumed to be zero, which simplifies the model and minimizes the computation time, while still resulting in an accurate result[45].

When the electromagnetic coil is placed at the center of the mesh in the xy-plane, with the magnetic field lines flowing from negative to positive on z-axis and the x-axis pointing upwards, the magnetic field strength in the y- and z-direction can be plotted and is presented in Figure 3.2. The dashed yellow lines are the transition lines from areas with a certain magnetic field strength to another.

Finally, the magnetic field strength in z-direction is plotted, since the ECB will be assumed to aim the magnetic field's centreline, the z-axis in the model, at the target. Thus, the values of the magnetic field strength along this centreline will be used in Chapter 4 and following chapters. Figure 3.3 shows the strength of the magnetic field in the z-direction along the centreline of the current loop.

It can thus be seen that magnetic field strength rapidly decays and slowly converges to zero at a distance of 6 meter from the center of the coil.

However, the magnetic field will not be uniform over the entire surface of the uncooperative object. Therefore, in order to visualize the flow of a magnetic field, the field is plotted as a vector flow, which is shown in Figure 3.4. The influence of the non-uniformity on the working of an ECB will be discussed further in Chapter 6.

Since there is no baseline for an electromagnet that can be used as an ECB to detumble the Kosmos-3M second stages, a different configuration of the electromagnet will also be modelled, called configuration B. For this configuration the diameter is chosen to be four times smaller than that of configuration A, which drastically decreases the size of the chaser. In the following chapters, configuration B can possibly be used when fast detumbling times are measured and a weaker magnetic field can also detumble the target in a reasonable amount of time.

The parameters of configuration B can be found in Table 3.4.

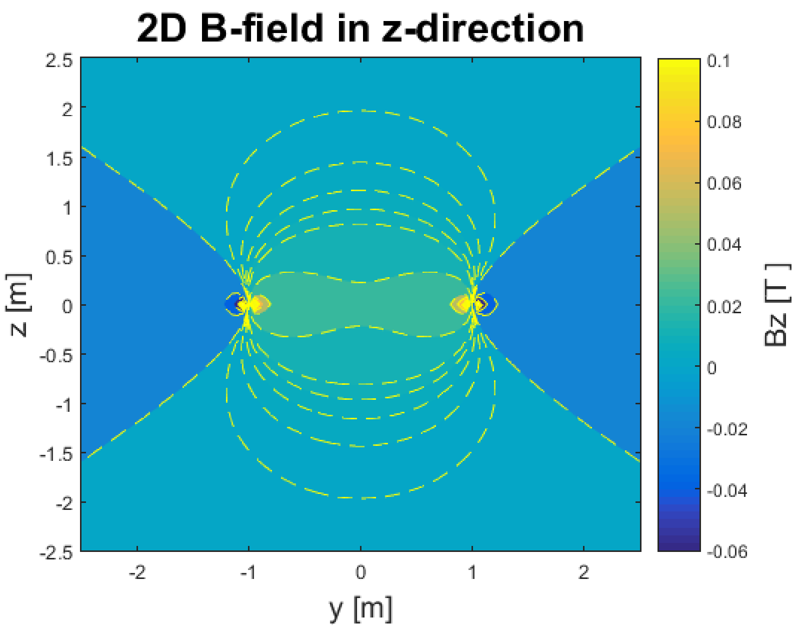

Figure 3.2: Strength of the magnetic field in the yz-frame in configuration A

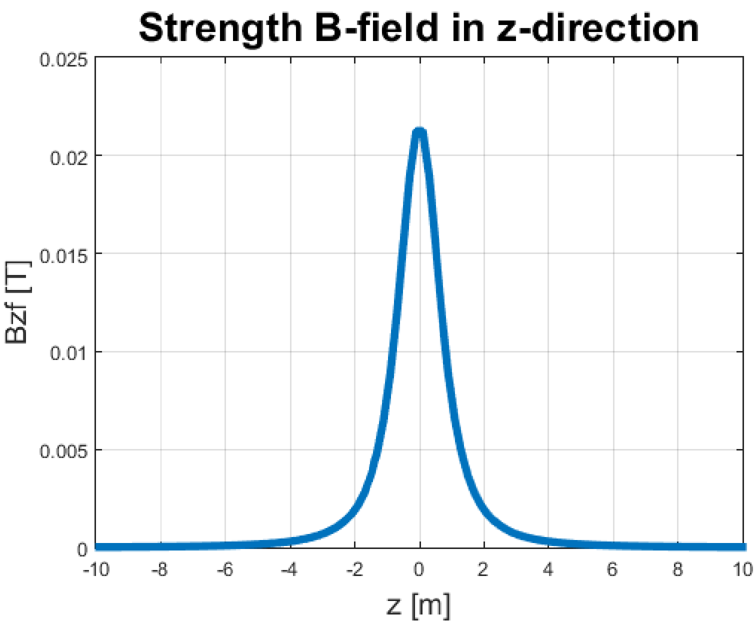

Figure 3.3: Magnetic field strength along the z-axis of the current loop in configuration A

Table 3.4: Input parameters magnetic field model for configuration B

a	0.5	[m]
I_0	34.3	[A]
n_e	500	[-]
l_{sp}	0	[m]
(x_c, y_c, z_c)	(0,0,0)	[m]

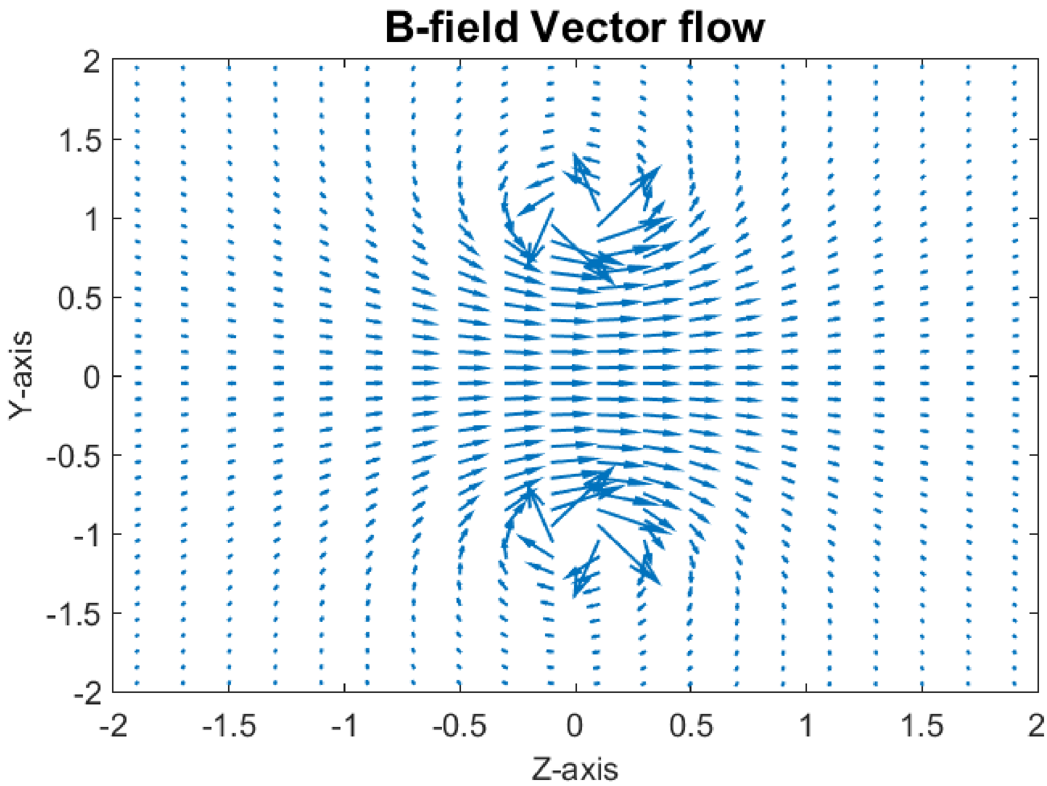

Figure 3.4: Vector flow in the yz-frame in configuration A

For this configuration the strength of the magnetic field in the y- and z-direction is plotted in Figure 3.5. Furthermore, the strength of the magnetic field in the z-direction along the centreline of the current loop, is shown in Figure 3.6.

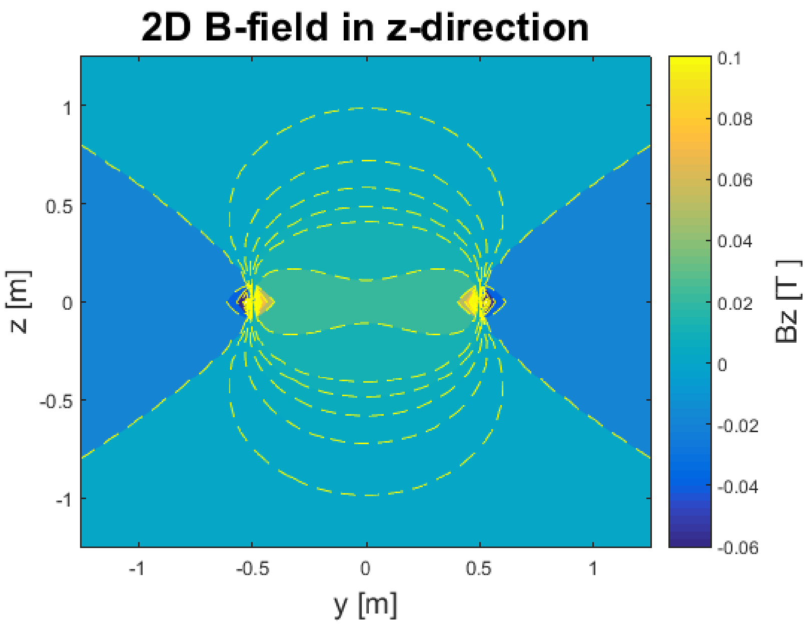

Figure 3.5: Strength of the magnetic field in the z-y frame in other configuration

When comparing the two configurations, it is immediately noticeable that, while the magnetic

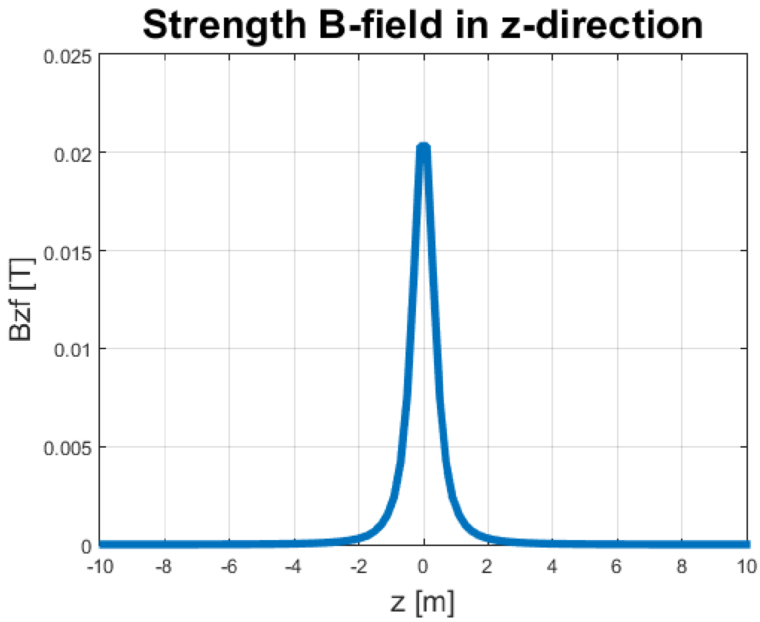

Figure 3.6: Magnetic field strength along the centreline of the current loop in other configuration

field strength at the center of the coil is comparable, the magnetic field strength decays faster over distance. Increasing the number of loops can achieve a stronger magnetic field close to the center of the coil. However, the trend at which the magnetic field strength converges to zero remains the same, as can be seen in Figure 3.7. However, this is a relative representation, meaning that the strength of the magnetic field is relatively small at a distance of 5 meter compared to the strength of the magnetic field at the center of the coil. In the following Chapters, it will be investigated if the magnetic field is strong enough to detumble a large target such as a Kosmos-3M second stage.

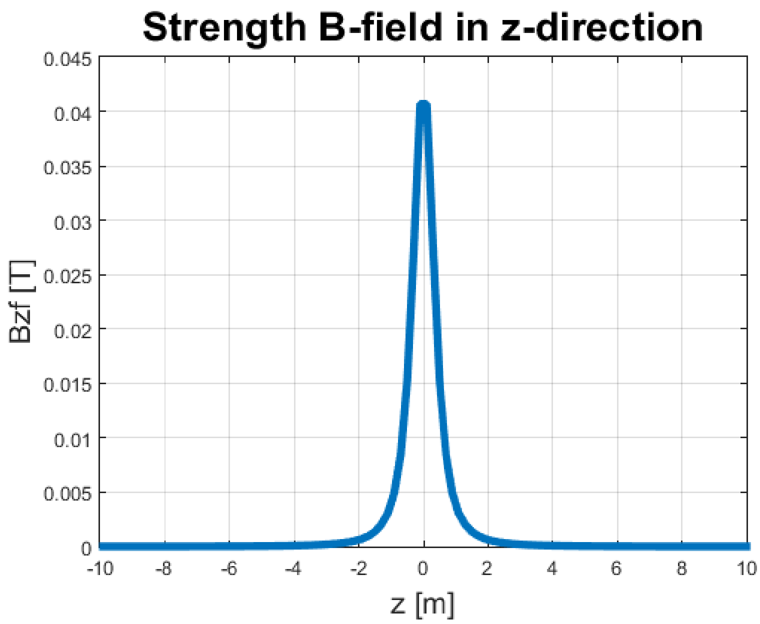

Figure 3.7: Magnetic field strength along the centreline of the current loop in other configuration with 1000 loops

FINAL DESIGN

In order to achieve a fast detumbling time of the Kosmos-3M rocket, the configuration A of the coil will be used initially, as presented in Table 3.3, which generates the strongest magnetic field. However, other constraints placed upon operation of the electromagnet need to be discussed in order to assess the viability of this chosen configuration.

The most important constraint is the power supply. In order to supply the power needed to operate the electromagnet a Direct Current (DC) or Alternating Current (AC) power supply can be used. An AC power supply has the advantage of cancelling some forces generated by the ECB as will be discussed in Chapter 6. However, in practice, any voltage change through the electromagnet, will result in a voltage spike across the eddy currents and even mechanical stresses in the windings, possibly leading to a magnetic quench. As a result, current changes need to be done gradually in order to limit the voltage spikes and avoid a magnetic quench, which partially voids the usefulness of using an AC power supply.

Therefore, a high current, very low voltage DC power supply will be used. A low voltage is present, due to the resistance of the feeder wires. In order to estimate the voltage created, distributors of power supplies and their products for superconducting magnets are looked at, leading to the conclusion that for a current between 60 and 80 Ampere, a voltage of around 10 Volts will be created[50, 51].

Another important aspect is the power needed in order to operate the ECB. This power can be divided into two categories, being: the power needed for the electromagnet and the power needed to cool the electromagnet.

The power needed for the electromagnet can easily be found by multiplying the voltage with the current, which leads to around 700 Watts needed to operate the ECB without cooling.

Secondly, the power needed to cool the electromagnet is dependent on the cooling system chosen, the size of the magnet, windings, etc. As a result, this research will not provide an estimation of this power, but instead will include some safety factor in the design.

Finally, the feasibility of a satellite continuously providing around 1000 Watts of power while operating the ECB can be assessed, by comparing the power to that of operational satellites. For example, typical research satellites operate with only 200 to 800 Watts of electricity generated by sunlight and solar panels carried by the satellites[52]. As a result, it can be concluded that the chaser's ECB can be powered by solar panels. However, future research is necessary in order to design the chaser in more detail.

The parameters of the final design of the electromagnet can then be found in Table 3.5.

Table 3.5: Parameters magnetic field model for the final design

a	1	[m]
I_0	68.5	[A]
V	10	[V]
P	685	[W]
n_e	500	[-]
l_{sp}	0	[m]
(x_c, y_c, z_c)	(0,0,0)	[m]

4

Detumbling of generic, uncooperative objects

In Chapter 3 the magnetic field was modelled for the ECB. In this chapter, basic shapes, such as the sphere, cylinder and double silo will be modelled and their Magnetic Tensor and the torque simulated in order to verify the model. Different magnetic field strength vectors and angular velocity vectors will be chosen for the different shapes in order to provide an overview of the capabilities of an ECB.

4.1. Modelling procedure

Before the basic shapes will be discussed, first the process of modelling the Magnetic Tensor and simulating the induced torque needs to be discussed, which can be found in Figure 4.1. It describes how the basic model functions and which elements of the model are verified.

First the target/shape needs to be chosen. The basic shapes used in this Chapter will be a sphere, a hollow cylinder and a hollow cylinder with two half spheres on either side, which will be called the double silo. In Chapter 5 and following the Kosmos-3M second rocket stage shape will be used as input.

After the shape has been chosen, their characteristics, which will differ based on the shape chosen, and the input parameters of the model need to be defined. The input parameters are:

- Radius of both sphere and cylinder R
- Length of cylinder L
- Skin thickness e
- Magnetic field strength $\vec{B}$
- Angular velocity of target $\vec{\omega}$
- Conductivity of target σ

The shapes can then be modelled using a frame model consisting of nodes and bars, as discussed in Chapter 2. The most important parameter influencing this model is the mesh size, which defines how accurately the object is presented by the model. Increasing this mesh size will increase the accuracy of the solution, but also increase the computation time. Therefore, a trade-off will take place to define the ideal mesh size for the different objects, taking computational time and accuracy of the solution into account.

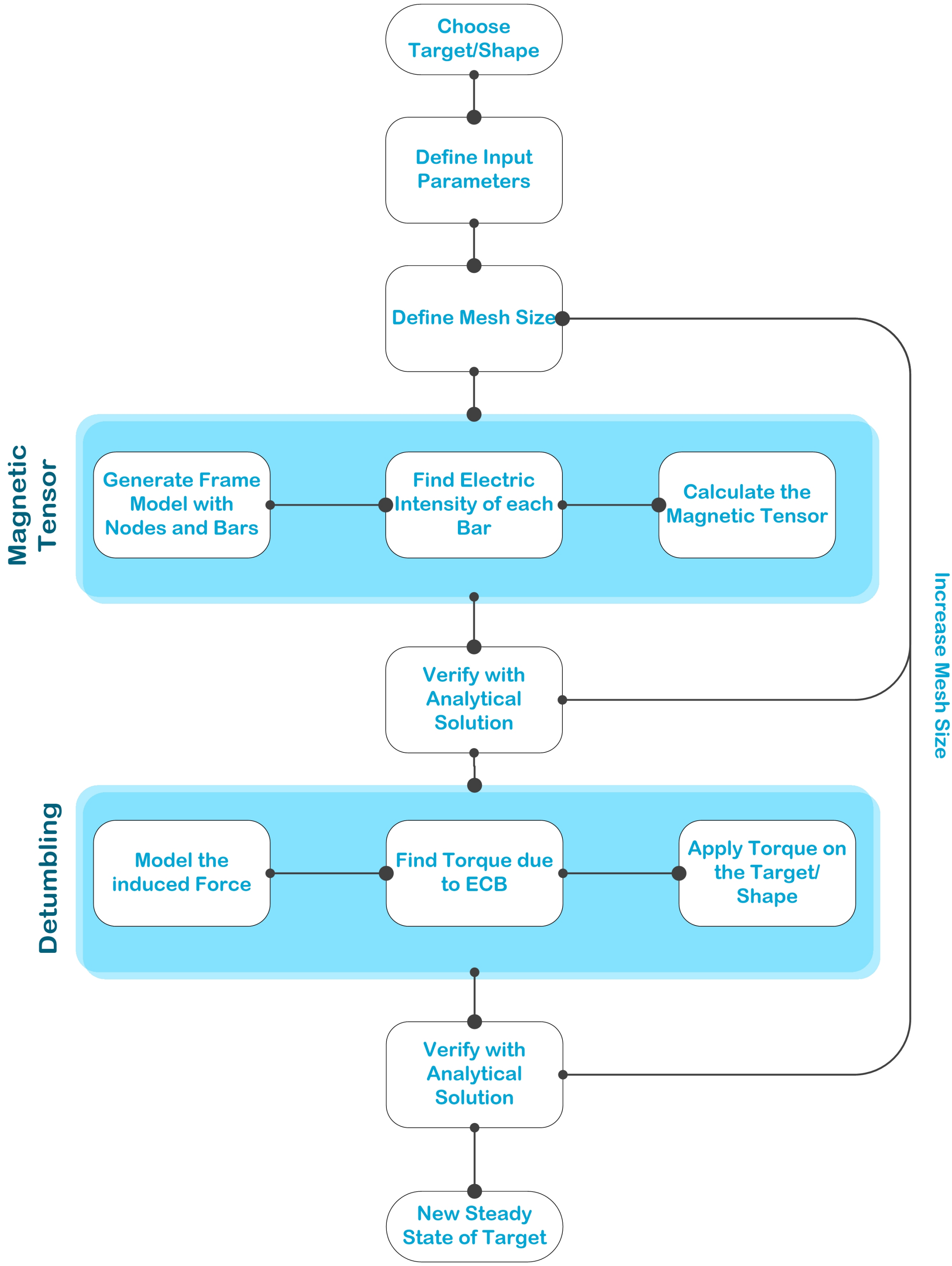

Figure 4.1: Detumbling and Magnetic Tensor modelling procedure

When a mesh has been chosen and the shape has been modelled, the Magnetic Tensor of the target can be calculated by using the method described in Section 2.2, where first an electric intensity J is assigned to every bar in the frame model.

Analytical expressions for both sphere and cylinder, listed in Section 2.2, can then be used to verify the solution of the Magnetic Tensor obtained by the model. If no good match has been found the mesh size has to be increased and the Magnetic Tensor calculated again until a good match has been achieved.

After the Magnetic Tensor has been found and is verified, the induced force and the resulting torque can be simulated. This torque can then be applied to the target/shape in order to model the detumbling.

Again, using analytical expressions as presented in Section 2.2, the torque found by the model can be verified. And similarly, if no good match has been found, the mesh size needs to be increased, the new Magnetic Tensor calculated and a new resulting torque applied to the shape.

The detumbling of the target then leads to a new steady state of the target, after which it is either safe to capture or is still tumbling over axes that were not damped to zero by the ECB. In order to damp all angular velocities, the direction of the magnetic field needs to be altered and the force and torque calculated over again until all angular velocities are sufficiently small for an ADR mission.

4.2. BASIC SHAPES

In order to verify and validate the model as described in Figure 4.1, basic shapes will be used as reference shapes. These shapes will be symmetric over all axes of the body reference frame, making the Magnetic Tensor a diagonal matrix as discussed in Section 2.2. However, before discussing the basic shapes, first the reference frames that will be used in this and subsequent chapters need to be discussed.

The target will be tumbling in an orbital reference frame, with its origin in the Center of Gravity (CoG) of the target, with the x-axis pointing in the along track velocity, the z-axis pointing in nadir direction, and with the y-axis being perpendicular to the orbital plane. Furthermore, this reference frame is assumed to be fixed to the reference frame of the electromagnet carried by the chaser, where the center of the coil is the origin, and the axes are pointing in the same direction as the reference frame of the fixed at the CoG of the target. The chaser and target and thus their orbital reference frames are assumed to be at a fixed distance from each other for the duration of the detumbling mission. For simplicity, the reference frame in which the targets rotate will be called the chaser fixed frame.

Additionally, a body reference frame, which moves together with the target's rotation will be used, with the origin in the CoG of the object, the z-axis running along the longitudinal axis and the x- and y-axis perpendicular to each other and the z-axis.

This Thesis aims to prove that an ECB is a viable option to detumble debris. In order to simulate and prove the workings of an ECB other accelerations and torques as a result from perturbations present for objects operating in Earth orbits, of non-magnetic nature are neglected. This assumption can be made since satellites flying in formation already orbit the Earth with success and it can be assumed that with current technology, the relative distance between chaser and target can be retained.

4.2.1. SPHERE

The most basic shape is the sphere, which can be approximated as a 3D frame model. In Section 4.1 it was explained that increasing the number of nodes increases the accuracy of the model, which can be seen in Figures 4.2 and 4.3, where the sphere is plotted in the body reference frame. The first frame model uses 171 nodes and the second 4851 and are both plotted in the body frame.

In order to model Figures 4.2 and 4.3, the radius of the Kosmos-3M cylinder tank is used, in order to get a reasonable representation of the detumbling of the Kosmos-3M second stage. Furthermore, configuration A of the MgB_2 coil will be used together with the skin thickness of the Kosmos-3M, as presented in Chapter 3 and the sphere will be placed at at an arbitrary distance of 8 meters from the

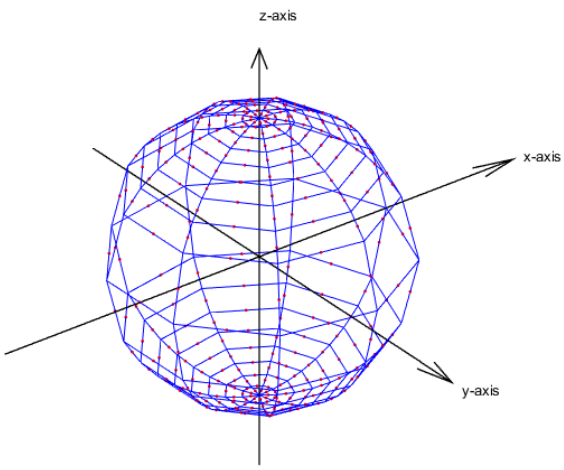

Figure 4.2: Frame model sphere with 171 nodes

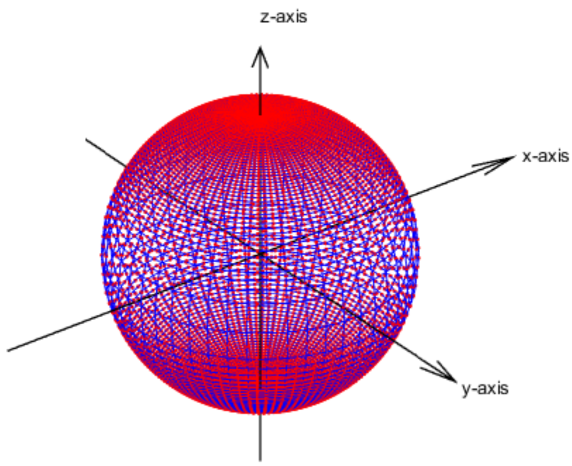

Figure 4.3: Frame model sphere with 4851 nodes

coil. The rotational motion of the sphere will be assumed to be over the x- and y-axis, as discussed in Section 2.2 and finally, the target is assumed to be made entirely of aluminium, which, together with the temperature (for now assumed to be 293.15 Kelvin), defines the electrical conductivity σ.

The input parameters of the model can be found in Table 4.1.

Table 4.1: Input parameters sphere

R	1.2	[m]
e	0.05	[m]
$\vec{B}$	[0 37.8 0]	[μ T]
$\vec{\omega}$	[72 72 0]	[deg/s]
σ	3.5 10^7	[S/m]

Using the frame model in Figure 4.2 and the method in Figure 4.1 the Magnetic Tensor, using the body reference frame, can be found to be:

$$M_{S_{171}} = \begin{bmatrix} 7.4942 & 0 & 0 \\ 0 & 7.4962 & 0 \\ 0 & 0 & 6.7556 \end{bmatrix} 10^6 [Sm^4] \tag{4.1}$$

Since a sphere is symmetric over any imaginable axis that runs through its center, the Magnetic Tensor will only have elements on its diagonal and those elements are equal[28]. It can already be concluded that Figure 4.2 is not a good representation of a sphere, which translates itself in the Magnetic Tensor. In order to find a good representation of a sphere, the mesh size will be increased until it closely matches the Magnetic Tensor calculated using the analytical method. In order to verify the solution, the torque calculated with the analytical model and the torque calculated by the model will be compared.

The analytical solution of the Magnetic Tensor of a spherical shell is[28]:

$$M_{ver} = \frac{2\pi}{3}\sigma R^4 e \begin{bmatrix} 1 & 0 & 0 \\ 0 & 1 & 0 \\ 0 & 0 & 1 \end{bmatrix} [Sm^4] \tag{4.2}$$

Using the parameters in Table 4.1, the analytical solution for Magnetic Tensor becomes:

$$M_{ver} = \begin{bmatrix} 7.6001 & 0 & 0 \\ 0 & 7.6001 & 0 \\ 0 & 0 & 7.6001 \end{bmatrix} 10^6 [Sm^4] \tag{4.3}$$

As can be seen from the Magnetic Tensor obtained via the analytical method, the elements of its diagonal equal. Furthermore, when comparing it to the Magnetic Tensor obtained via the model with 171 nodes, it can be concluded that the first two elements of the diagonal already match those of the analytical solution closely. However, in order to find a good match, the mesh size is increased stepwise until the solution converges and the error between the analytical solution match. The mesh size is defined by a trade-off between computation time and accuracy.

The final shape of the sphere was decided to be the frame model defined in Figure 4.3 which has 4851 nodes. As a result, the Magnetic Tensor becomes:

$$M_{S_{4851}} = \begin{bmatrix} 7.5929 & 0 & 0 \\ 0 & 7.5929 & 0 \\ 0 & 0 & 7.5711 \end{bmatrix} 10^6 [Sm^4] \tag{4.4}$$

The diagonal elements of the Magnetic Tensor are now closely matched, indicating that the model approaches the shape of a sphere, with an error smaller than 0.4%.

From the Magnetic Tensor, the torque can be calculated by using Equation (2.22), which is dependent on the Magnetic Tensor, the magnetic field (which are both assumed to be constant over time for this example) and the rotation rate of the sphere. As a result the torque varies over time since the objects angular velocity is slowly decaying over time due to the ECB. Furthermore, Equation (2.22) also indicates that the rotation rate can never truly become zero, but instead will slowly converge to zero, since a torque is only created when there is a relative motion between the electromagnet and the target.

This torque, working on the sphere, affects the angular velocity vector, which changes the torque in return. In order to find this rate of change a relation for the rotation rate is needed, which can be found in Equation (4.5)[53].

$$\vec{\omega}_{t+1} = \vec{\alpha}\,\Delta t + \vec{\omega}_t \tag{4.5}$$

Where the factor α is the angular acceleration over an axis, which equals the torque on that axis divided by the inertia of the object on that axis. The moment of inertia of targets that can be mirrored over every axis will only have non-zero elements on its diagonal. However, for more more complex shapes, such as the Kosmos-3M second rocket stage, the inertia matrix will also have other non-zero elements, reflecting its asymmetry.

In order to find the angular acceleration, the relation of the angular acceleration and the torque needs to be found, which are based on Newton's three fundamental law's of motion. When considering a particle with a momentum $\vec{p}$ and a position vector $\vec{r}$, which is measured from the axis of rotation, a variable $\vec{l}$ can be defined[53, 54]:

$$\vec{l} = \vec{r} \times \vec{p} \tag{4.6}$$

After differentiation, a torque equation is found:

$$\vec{T} = \vec{r} \times \vec{F} \tag{4.7}$$

And using the following relation, the torque in relation to the angular acceleration can be found[53, 54]:

$$\frac{d\vec{v}}{dt} = \vec{a} = \vec{\alpha} \times \vec{r} \tag{4.8}$$

$$\vec{T} = I\vec{\alpha} \tag{4.9}$$

Where $\vec{a}$ is the acceleration vector. The above relation is valid for both a single particle and for larger rigid bodies composed of a large number of particles[53, 54].

In this thesis, in order to simplify the calculations the inertia matrix will be assumed to only have non-zero values on its diagonal. This assumption can be made since the non-zero elements that are not on the diagonal are small compared to those on the diagonal. As a result, Equation (4.9) can be rewritten to compute angular acceleration over the x-, y- and z-axis:

$$\vec{\alpha} = \vec{T} I^{-1} \tag{4.10}$$

Alternatively, since the inertia matrix will only have non-zero values on its diagonal and all diagonal elements will be non-zero, this equation can be rewritten as:

$$\alpha_i = \frac{T_i}{I_i} \tag{4.11}$$

For a sphere, the mass moment of inertia I is the same for every axis and can be calculated by:

$$I_{x,y,z} = \frac{2}{3} M_{tot} R^2 \tag{4.12}$$

Where the total mass of the spherical shell, M_{tot}, can be found by multiplying the volume of the spherical shell by its density, which is 2700 kg/m^3 for aluminium.

As can be seen from Table 4.1 the magnetic field vector is pointing in the positive y-direction and the sphere is rotating over both the x- and y-axis in the chaser fixed frame. As a result there will only be a torque generated for the rotation over the x-axis, since the magnetic field vector is perpendicular to the x-axis and parallel to the y-axis. Furthermore, there is no initial angular velocity over the z-axis, therefore there is also no torque present during the time the ECB is active, since there needs to be a relative motion between the ECB and the object in order to exert a torque. The angular velocity over the y- and z-axis will thus remain the same.

The analytical expression for the torque produced by an ECB working on a sphere has been given in Equation (2.7). Furthermore, the analytical solution of the Magnetic Tensor can be used together with Equation (2.22) to obtain the solution via a different route, which will also be used to check the value of the model against.

In order to check this reasoning, the torque needs to be simulated. The analytical expression for the torque for a sphere as found in Equation (2.7), with input parameters listed in Table 4.1, results in the following torque vector:

$$T_{v_{ana}} = \begin{bmatrix} -0.0136 & 0 & 0 \end{bmatrix}^T [Nm] \tag{4.13}$$

As predicted the torque only works over the x-axis, thus damping only the angular velocity over the x-axis. In order to assess the Magnetic Tensor model, the torque vector obtained by using the analytical solution of the Magnetic Tensor, as found in Equation (4.3), can be calculated by Equation (2.22) and be compared to the analytical solution of the torque.

$$T_{v_{tens}} = \begin{bmatrix} -0.0136 & 0 & 0 \end{bmatrix}^T [Nm] \tag{4.14}$$

As can be seen the torque matches perfectly, which leads to the conclusion that the Magnetic Tensor model is verified.

In order to verify the model built for this Thesis, the torque found by the model at the start of the detumbling mission, when the magnet has just been turned on, will be compared to the analytical and Magnetic Tensor torques found above. The torque vector found by the model at the time $t = 0$.

$$T_{m_{t=0}} = \begin{bmatrix} -0.0135 & 0 & 0 \end{bmatrix}^T [Nm] \tag{4.15}$$

In order to verify the model and simulate and accurate detumbling mission, the torque vectors are compared. The values of the torque vector found by the model closely match the torque vectors found by using the analytical approach, with the error being smaller than 0.01%. This error exists because the frame model of the sphere does not represent a perfect sphere. However, for the purposes of this thesis, the error is assumed to be small enough to prove that a large conductive target can be detumbled with the use of an ECB.

It can thus be concluded that the model is verified for a spherical shell. However, in order to make sure the model works for different and more complex sizes, additional shapes will also need to be verified.

Now that the model has been checked, the torques can be modelled, and are presented in Figure 4.4. When the magnetic field vector is perpendicular to an angular velocity, the largest torque is generated, which is ideal for the detumbling time as presented in Figure 4.5.

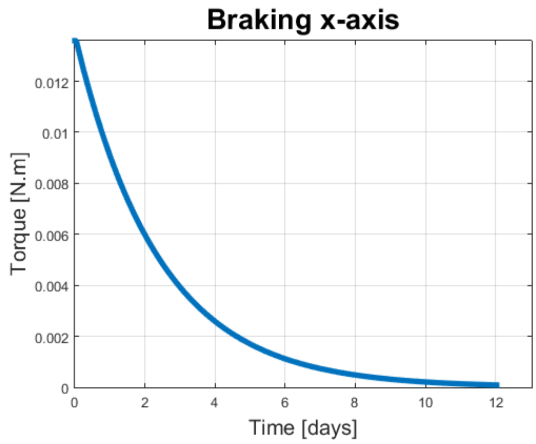

Figure 4.4: Absolute torque over time on the sphere in the x-direction

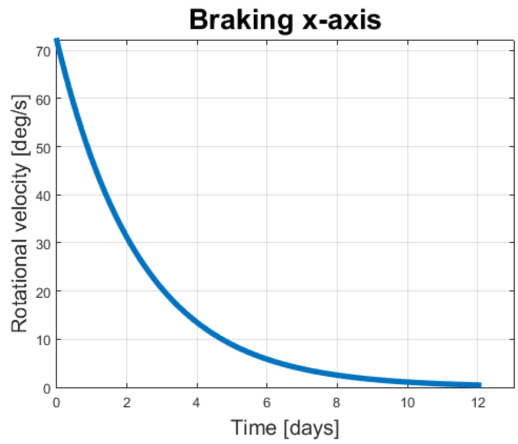

Figure 4.5: Angular velocity over time of the sphere in the x-direction

Another way to represent the detumbling of the sphere is to look at the total angular velocity over time, which can be found in Figure 4.6. Since there was no initial angular velocity over the z-axis, and the angular velocity over the x-axis was completely damped as presented in Figure 4.5, the total angular velocity decreases over time until only the velocity over the y-axis remains.

However, the object will realign itself during the detumbling motion due to the fact that an angular velocity over one axis is not damped while the others are gradually damped over time. As a result, the object will realign itself gradually over an angle of 45 degrees over the x-axis from the initial angular velocity vector, which needs to be the case since the initial angular velocities over the x and y-axis are equal.

In order to be able to damp the total rotation of the sphere, a subsequent detumbling phase is necessary, in which the chaser realigns itself to the target in such a way that the magnetic field generated by the ECB is perpendicular to the angular velocity of the object. This will not be simulated here, but will be further discussed for different cases in the subsequent Chapters, which try to eliminate the need to move the chaser relative to the target in order to damp all angular velocities.

4.2.2. CYLINDER

Another basic shape is a hollow cylinder with no tops. Again, the shape of the cylinder will be approximated by the model by using a frame model, where an increase in the number of nodes increases the accuracy of the model.

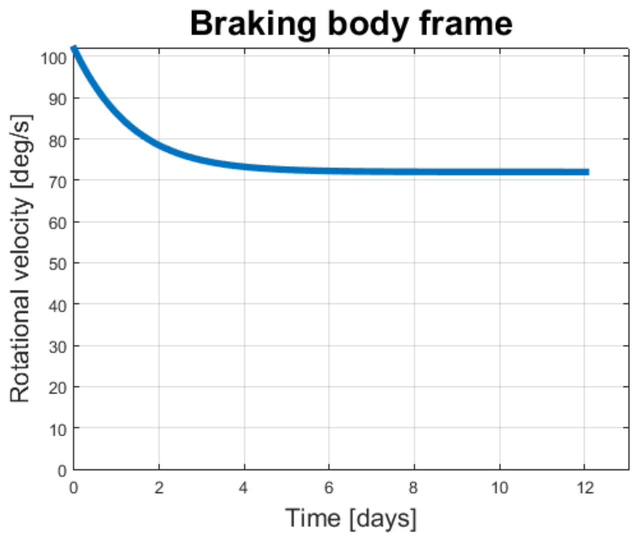

Figure 4.6: Resulting angular velocity of the sphere over time

Figure 4.7 uses 100 nodes and Figure 4.8 uses 4900 nodes, and represent both the initial position of the cylinder in the chaser fixed reference frame and the object in the body reference frame, which is fixed to the cylinder.

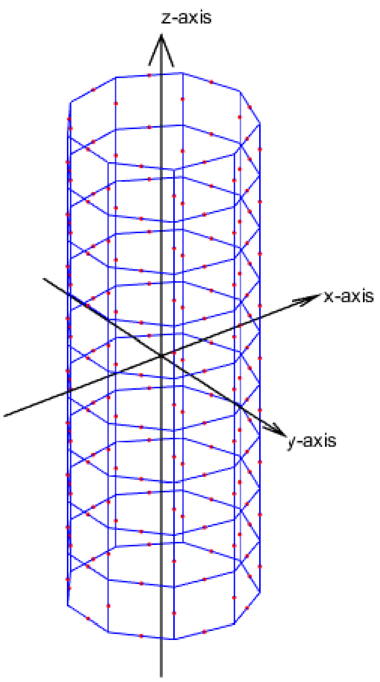

Figure 4.7: Frame model cylinder with 100 nodes

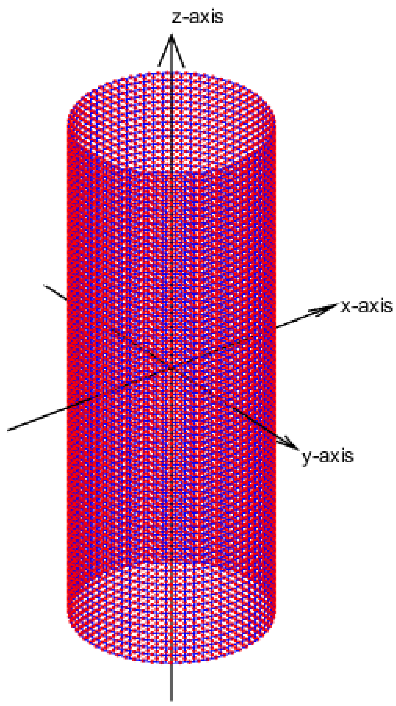

Figure 4.8: Frame model cylinder with 4900 nodes

Similarly to the sphere, the cylinder will be modelled to best represent the shape of the Kosmos-3M second stage. Furthermore, the cylinder will be assumed to be made entirely of aluminium, the magnetic field will be working upon the object in the x and z-direction and the cylinder will rotate over its z-axis. This different set-up of magnetic field and angular velocity is chosen in order to represent what happens to the rotation of the object in different set-ups.

The input parameters of the model for the cylinder can then be found in Table 4.2.

Table 4.2: Input parameters cylinder

R	1.2	[m]
L	6.585	[m]
e	0.05	[m]
$\vec{B}$	[37.8 0 37.8]	[μ T]
$\vec{\omega}$	[0 0 72]	[deg/s]
σ	3.5 10^7	[S/m]

Using the frame model in Figure 4.7, the Magnetic Tensor can be found to be:

$$M_{C_{100}} = \begin{bmatrix} 4.8676 & 0 & 0 \\ 0 & 4.8676 & 0 \\ 0 & 0 & 2.2217 \end{bmatrix} 10^7 [Sm^4] \tag{4.16}$$

A cylinder is symmetric over all diametral axes, resulting in the first two elements of the Magnetic Tensor being equal. The cylinder is also symmetric over the z-axis, resulting in a smaller Magnetic Tensor element compared to the first two.

Again, it can be concluded that Figure 4.7 is not a good representation of a cylinder, which translates itself in the Magnetic Tensor. The number of nodes needs to be increased in order to find an accurate Magnetic Tensor. Similarly to the sphere, in order to find a good representation of a cylinder, the mesh size will be increased up until it closely matches the Magnetic Tensor calculated using the analytical method.

The analytical solution of the Magnetic Tensor of a cylindrical shell is[28]:

$$M_{C_{ver}} = \pi\sigma R^3 eL \begin{bmatrix} \gamma & 0 & 0 \\ 0 & \gamma & 0 \\ 0 & 0 & \frac{1}{2} \end{bmatrix} [Sm^4] \tag{4.17}$$

Where:

$$\gamma = 1 - \frac{2R}{L}\tanh\frac{L}{2R} \tag{4.18}$$

This analytical solution confirms the fact that the first two elements of the diagonal are equal. Using the parameters in Table 4.2, the analytical solution for Magnetic Tensor becomes:

$$M_{C_{ver}} = \begin{bmatrix} 3.9946 & 0 & 0 \\ 0 & 3.9946 & 0 \\ 0 & 0 & 3.1279 \end{bmatrix} 10^7 [Sm^4] \tag{4.19}$$

In order to verify the model, the mesh size is gradually increased until the error lies below 1%. Using the frame model in Figure 4.3 with 4900 nodes, the Magnetic Tensor becomes:

$$M_{C_{4900}} = \begin{bmatrix} 3.9985 & 0 & 0 \\ 0 & 3.9985 & 0 \\ 0 & 0 & 3.0356 \end{bmatrix} 10^7 [Sm^4] \tag{4.20}$$

The solution obtained by the model closely matches the analytical solution, with an error of around 1%. It can thus be concluded that the model can simulate the Magnetic Tensor of a cylinder accurately given a high enough number of nodes in the frame model.

From the Magnetic Tensor the torque vectors can be calculated using the same procedure as the one used for the sphere, except that the elements of the diagonal of the inertia matrix need to be calculated differently as shown in Equations (4.21) to (4.23).

$$I_z = \frac{M_{tot}}{2}\left((R-e)^2 + R^2\right) \tag{4.21}$$

$$I_x = I_y = \frac{M_{tot}}{12}\left(3\left(R^2 + (R-e)^2\right) + L^2\right) \tag{4.22}$$

$$I = \begin{bmatrix} I_x & 0 & 0 \\ 0 & I_y & 0 \\ 0 & 0 & I_z \end{bmatrix} \tag{4.23}$$

From the magnetic field vector and the initial angular velocity vector it can be concluded that a torque will work on both x- and z-axis, while there will be no torque on the y-axis due to the absence of both magnetic field and initial angular velocity.

Using the analytical expression for the Torque of an ECB working on a cylinder, as given in Equation (2.8), this reasoning can be checked.

The analytical expression for the torque, for a cylinder with input parameters listed in Table 4.2, results in the following torque vector:

$$T_{c_{ana}} = \begin{bmatrix} 0.0717 & 0 & -0.0717 \end{bmatrix}^T [Nm] \tag{4.24}$$

The analytical torque shows that there is indeed no torque working over the y-axis.

Secondly, the analytical solution of the Magnetic Tensor can be used together with Equation (2.22) to obtain the solution via a different route in order to check the Magnetic Tensor method and to provide another data point to which the model's solution can be compared to.

$$T_{c_{tens}} = \begin{bmatrix} 0.0717 & 0 & -0.0717 \end{bmatrix}^T [Nm] \tag{4.25}$$

These torque vectors can then be compared to the torque found by the model at the start of the detumbling mission when the magnet has just been turned on. The torque vector found by the model at the time $t = 0$.

$$T_{m_{t=0}} = \begin{bmatrix} 0.0717 & 0 & -0.0717 \end{bmatrix}^T [Nm] \tag{4.26}$$

The values of the torque vector found by the model closely match the torque vectors found by using the analytical approaches. It can thus be concluded that the model is verified for a cylindrical shell without tops.

After the torque is verified, the torque and detumbling over time can be simulated. The absolute values of the torque working on rotation over the x and z-axes is represented in Figures 4.9 and 4.10. Again, there is no torque in the y-direction since there is no magnetic field working on nor an angular velocity over the y-axis.

Different from the sphere, due to a different magnetic field and angular velocity, the torque on the cylinder is working on the x- and the z-axis. However, earlier it was said that an ECB requires a relative rotational motion between the chaser and the target in order to exert a torque and initially there is no angular velocity over the x-axis. Yet, as can be seen in Figure 4.9, there is a torque working on the x-axis. This is due to the fact that the object slowly aligns itself over time to the magnetic field vector, which lies at an angle of 45 degrees from the x-axis in the xz-plane, as can be seen in Figure 4.11. Therefore, there is a relative motion between chaser and target over the x-axis and thus a torque will be present.

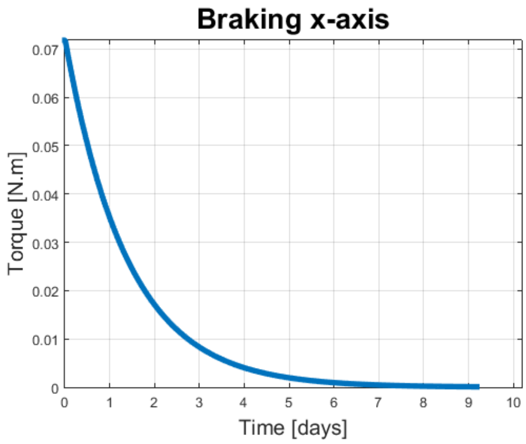

Figure 4.9: Absolute torque on the cylinder in the x-direction

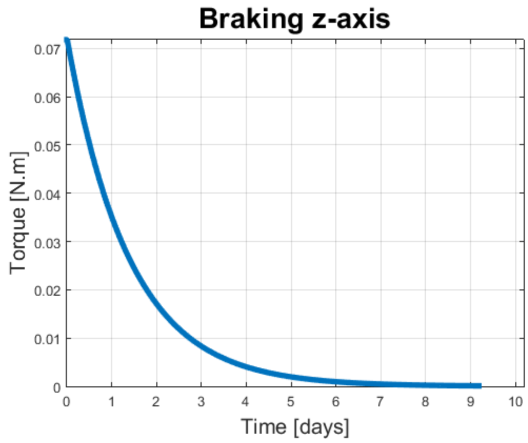

Figure 4.10: Absolute torque on the cylinder in the z-direction

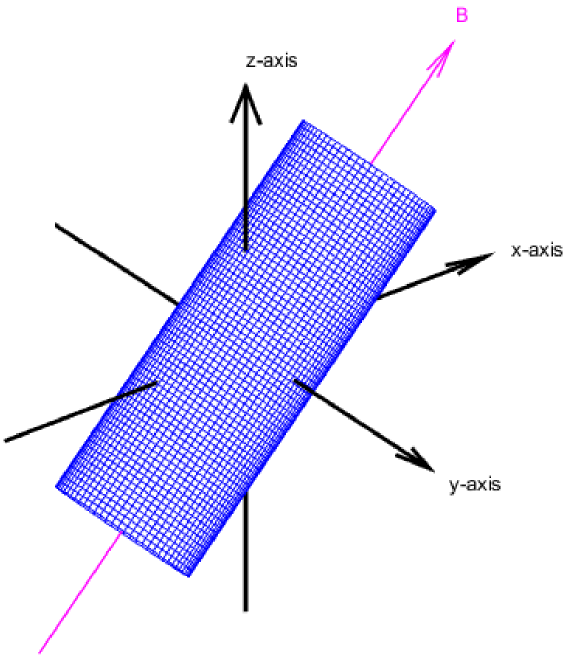

Figure 4.11: Cylinder aligning itself with magnetic field

As a result, the angular velocity over the x-axis increases, while it decreases over the z-axis, as can be seen from Figures 4.12 and 4.13.

Due to the fact that the object aligns itself to the resulting magnetic field vector, the cylinder's rotation will not completely be damped, as is again represented in Figure 4.14. Instead it converges to another constant angular velocity, meaning that the rotational motion is parallel to the magnetic field, resulting in no torque being produced.

This approach shows that the object will rotate to realign itself parallel with the magnetic field vector, whenever this magnetic field vector and the angular velocity vector are not perpendicular.

As a result, a subsequent detumbling phase will be needed with a magnetic field working on the object from a direction that is perpendicular to the target's angular velocity. A magnetic field in the y-direction would be the ideal candidate to damp both of these remaining angular velocities.

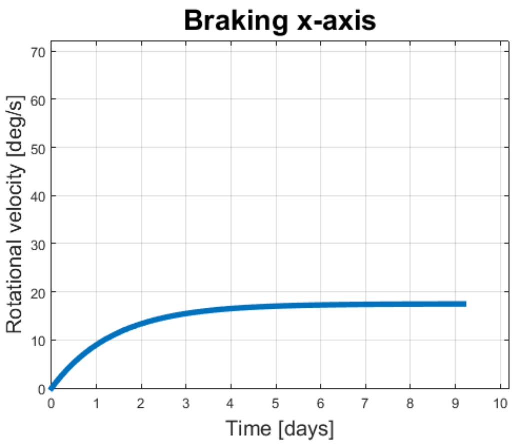

Figure 4.12: Absolute torque on the cylinder in the x-direction

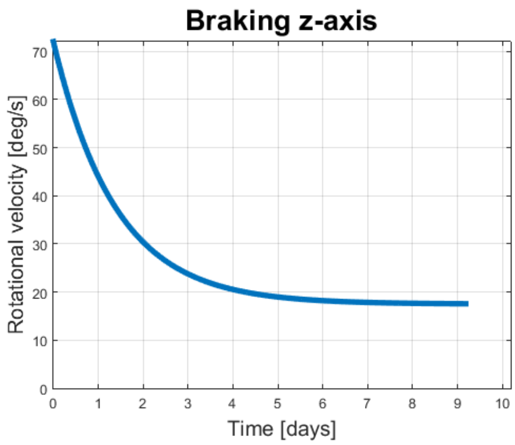

Figure 4.13: Absolute torque on the cylinder in the z-direction

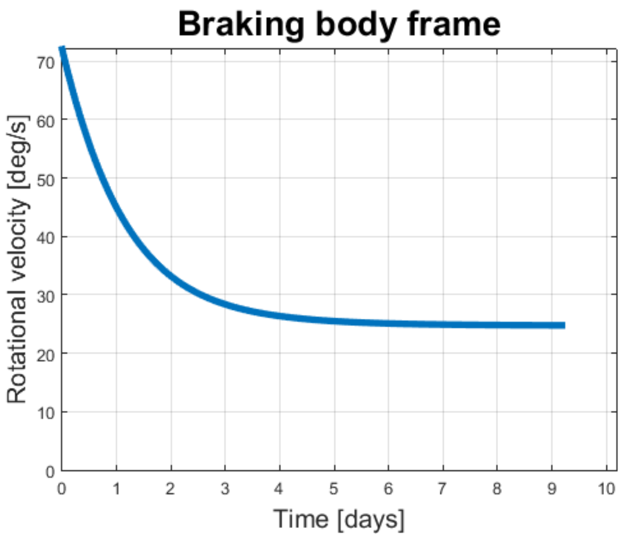

Figure 4.14: Angular velocity of the cylinder in the body frame

4.2.3. DOUBLE SILO

The two basic shapes have verified the model. The double silo, which is essentially a combination of the sphere and cylinder, will try to approach the shape of the Kosmos-3M second stage as close as possible in order to have a reference point to which the results obtained in Chapter 5 can be compared.

The shape of the double silo will be approximated by a frame model, where Figure 4.15 uses 180 nodes and Figure 4.16 uses 4900 nodes.

The sphere and cylinder were assumed to be made completely of aluminium. However, in Chapter 2 it was stated that the Kosmos-3M consists out of aluminium, but also other, non-conductive, materials. Therefore, in order to approximate the Kosmos-3M rocket better, the double silo will not be modelled to be made entirely out of aluminium, but instead its body will have a certain percentage of aluminium, as described in Section 2.2. For initial modelling parameters, the amount of aluminium in the body is 25% of its total mass, which will be randomly distributed over the body as an initial guess, but will be adapted to match reality better in Chapter 5. The conductivity of the body will be included in the model by using a random generator, which generates uniformly distributed random numbers, where the value $'1'$ means conductive material and a $'0'$ means non-conductive

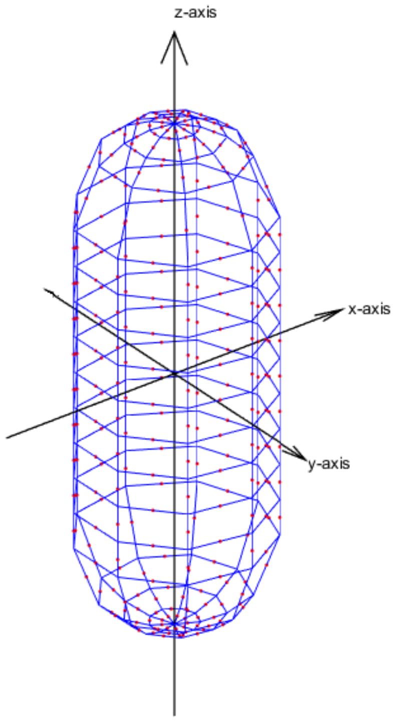

Figure 4.15: Frame model double silo with 180 nodes

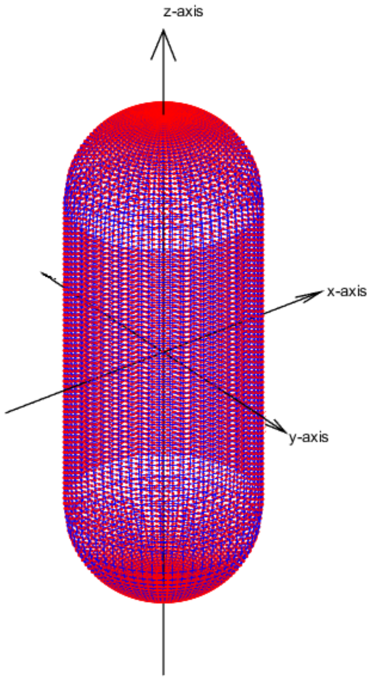

Figure 4.16: Frame model double silo with 4900 nodes

material. The conductive bars are assigned the value of the electric conductivity as found in Table 5.2. The bars that are not have been labelled as non-conductive material are not assigned a zero value, since everything can be considered a conductor, with for example Polyethylene Terephthalate (PET) having an electrical conductivity of $10^{-21} S/m$. The eddy currents will not follow the path of least resistance, since current will follow any path that is available to it-. However, more current will flow through the path of least resistance compared to the path with higher resistance.

The input parameters of the model for the double silo can then be found in Table 4.3, where the radius of the cylinder is also the radius for the top and bottom half-spheres of the silo. In order to stay compare the Magnetic Tensor of the double silo to those of the sphere and cylinder, the wall thickness will be assumed to be 5 cm. In Chapter 5, these input parameters will be revised to match the Kosmos-3M second rocket stage.

Table 4.3: Input parameters double silo

R	1.2	[m]
L	4.185	[m]
e	0.05	[m]
$\vec{B}$	[37.8 0 0]	[μ T]
$\vec{\omega}$	[0 72 72]	[deg/s]
σ	3.5 10^7	[S/m]

There exist no analytical solutions or different methods for the Magnetic Tensor simulated by using double silo as input for the model. However, N.O. Gomez and S.J.I. Walker simulated the Magnetic Tensor and detumbling times for the Ariane 4 H10 Upper Stage as a double silo.

The input for their simulation can be found in Table 4.4

Table 4.4: Input parameters Ariane 4 H10 Upper Stage

R	1.3	[m]
L	4.772	[m]
e	0.01	[m]
$\vec{B}$	[37.8 0 0]	[μ T]
$\vec{\omega}$	[28.8 28.8 28.8]	[deg/s]
σ	3.5 10^7	[S/m]
I	[28000 28000 3000]	[kgm^2]
m_{con}	32.5	[%]

Their simulation resulted in a Magnetic Tensor as can be found in Equation (4.27).

$$M_{S_{Alu}} = \begin{bmatrix} 5.908 & 0 & 0 \\ 0 & 5.908 & 0 \\ 0 & 0 & 1.951 \end{bmatrix} 10^6 [Sm^4] \tag{4.27}$$

Using the input parameters as defined in Table 4.4 in the model as described in Figure 4.1, with the conductive mass equalling 32.5% of the total mass and being randomly distributed, the following Magnetic Tensor is found by gradually increasing the number of nodes until the solution converges:

$$M_{S_{ver}} = \begin{bmatrix} 6.4612 & 0.0395 & 0.0581 \\ 0.0395 & 6.4612 & 0.0216 \\ 0.0518 & 0.0216 & 2.4180 \end{bmatrix} 10^6 [Sm^4] \tag{4.28}$$

The converged solution uses 4900 nodes, and while the two Magnetic Tensors are similar, they do not match perfectly with an error of around 9%. This is due to the fact that the ratio of conductivity in the body has been defined by N.O. Gomez and S.J.I. Walker, but not how the conductive material is distributed over the body. For example, more conductive material could be present in the cylindrical part, compared to the two half spheres, which results in a different Magnetic Tensor[28].

Furthermore, they assume that the conductive materials are still distributed in a symmetric manner in the body, which results in a Magnetic Tensor with with only non-zero elements on its diagonal, while the rest of the elements are zero. For this double silo, with the conductive mass equalling 32.5% of the total mass and being randomly distributed, the object is not symmetric over any axis, leading to the Magnetic Tensor only having non-zero elements.

However, since the Magnetic Tensors are of the same order of magnitude, it is a good indicator that the model works for different shapes and sizes, which is further supported by comparing the detumbling times of both Magnetic Tensors.

Figure 4.17, shows the evolution of the angular velocity vector, between the target body reference frame and the orbital reference frame leading to a changing direction in the angular velocity over time, for angular velocity over the x- and z-axis. The detumbling times in the orbital reference frame resulting from the model can be found in Figures 4.18 and 4.19.

When comparing Figure 4.17 with Figures 4.18 and 4.19, the detumbling times closely match.

As an additional verification step, first the Magnetic Tensor of the object, when made entirely out of aluminium will to be simulated. The model was verified for both sphere and cylinder by using analytical approaches, which allows more complex shapes as input for the model. However, as a check, an analytical expression for the Magnetic Tensor of a double silo cannot be used, since it has not been found yet, but instead the Magnetic Tensor will be compared to the one of the cylinder. Additionally, since both sphere and cylinder approached the shape within a certain error margin

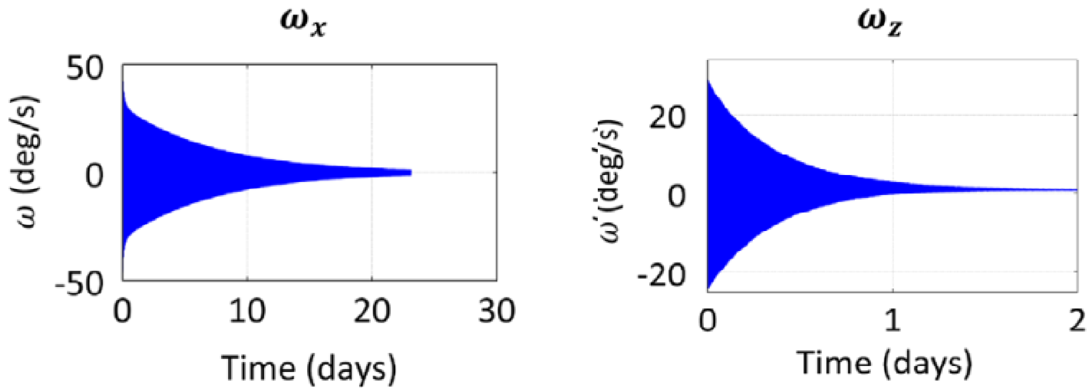

Figure 4.17: Angular velocities over the x- and z-axis between the target body reference frame and the orbital reference frame as found by N.O. Gomez and S.J.I. Walker [28]

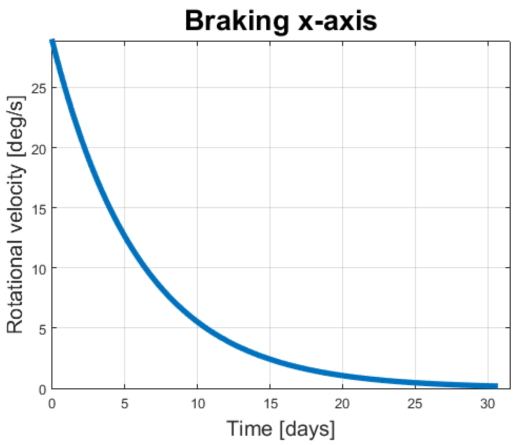

Figure 4.18: Angular velocity over the x-axis for Ariane4 H10 upper stage

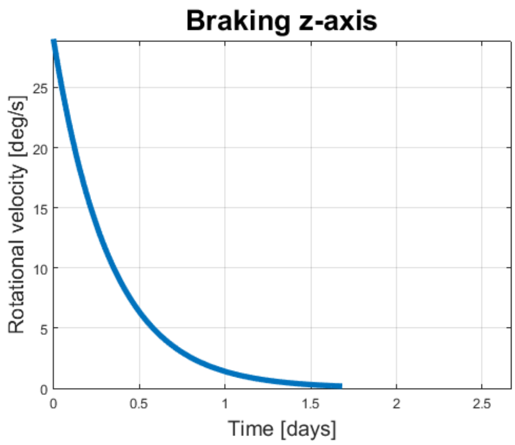

Figure 4.19: Angular velocity over the z-axis for Ariane4 H10 upper stage

when using 4900 nodes and the Magnetic Tensor of the double silo of the Ariane 4 upper stage converges to a solution at 4900 nodes, the Magnetic Tensor of the double silo will be simulated by using 4900 nodes.

$$M_{S_{Alu}} = \begin{bmatrix} 6.70565 & 0 & 0 \\ 0 & 6.70565 & 0 \\ 0 & 0 & 2.7039 \end{bmatrix} 10^7 \, [Sm^4] \tag{4.29}$$

As can be seen the Magnetic Tensor still only has elements on its diagonal, due to its symmetry, with the first two elements being equal and the third being smaller than the first two. Since the object has increased in length due to the addition of the tops, the third element is relatively smaller compared to the first two elements than that of the Magnetic Tensor of the cylinder. Furthermore, the first two elements have increased because of the object's increase in size, which can be verified since the Magnetic Tensor of the cylinder is bigger than that of the sphere due to the increase in size.

In order to approximate the shape and materials of the Kosmos-3M second rocket stages, 25% of the bars in the frame model will, randomly, with the random generator discussed previously, be assigned to be aluminium and the other to be non-conductive. As a result, the Magnetic Tensor will no longer only have elements on its diagonal due to the objects conductive materials not being symmetrically distributed over the body.

The Magnetic Tensor of the double silo with 25% conductive materials then becomes:

$$M_{S_{Alu_{25}}} = \begin{bmatrix} 115.76 & -2.915 & -2.5971 \\ -2.915 & 218.22 & 3.7223 \\ -2.5971 & 3.7223 & 69.583 \end{bmatrix} 10^5 [Sm^4] \tag{4.30}$$

When looking at the magnetic field vector and initial angular velocity vector, it can be seen that there is no initial angular velocity over the x-axis and that the magnetic field is parallel to the x-axis, leading to the conclusion that no torque will be induced over the x-axis.

For Chapter 5 and subsequent Chapters, the effect the amount of conductive material in the target has on the detumbling time is investigated. Therefore, the detumbling time in both the y- and z-direction is plotted in Figures 4.20 to 4.23, for the two cases discussed above.

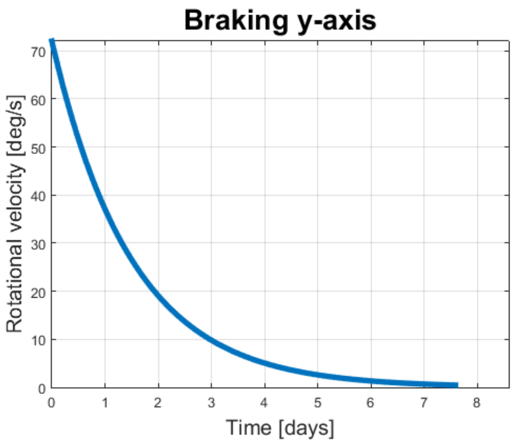

Figure 4.20: Angular velocity of the silo made entirely out of aluminium in the y-direction

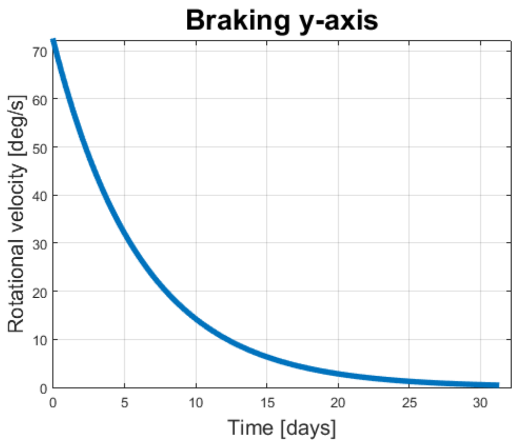

Figure 4.21: Angular velocity of the silo made 25% out of aluminium in the y-direction

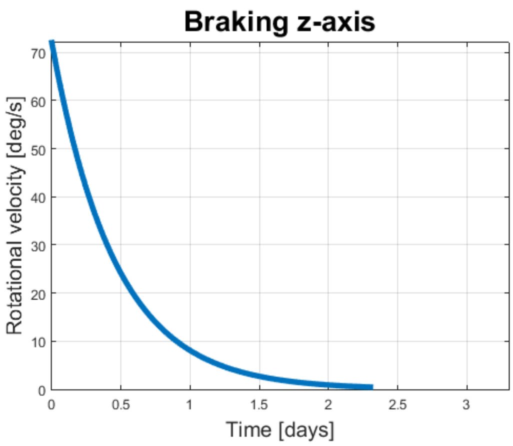

Figure 4.22: Angular velocity of the silo made entirely out of aluminium in the z-direction

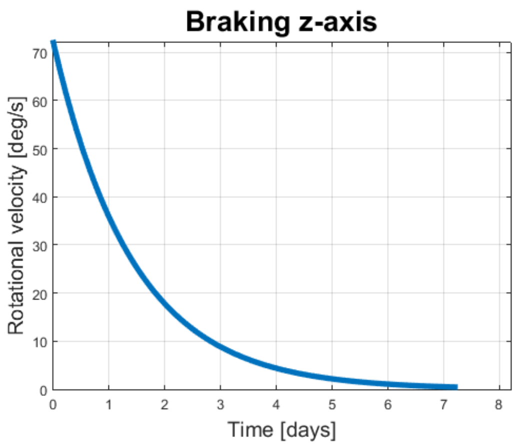

Figure 4.23: Angular velocity of the silo made 25% out of aluminium in the z-direction

As can be seen, the angular velocity over the z-axis converges to zero more quickly than the angular velocity over the y-axis. For this case, the angular velocity over the z-axis gets damped 3.5 times quicker, because the magnetic field vector points in the along track direction and the z-direction is perpendicular to the orbital plane. For the cylinder, this effect was not noticeable since the angular velocity was not damped to zero and the object slowly turned to align itself to the magnetic field vector.

Furthermore, when the body has less conductive materials, 25% in this case, the body will be detumbled more slowly, since weaker eddy currents and therefore, a weaker torque will be produced by the ECB. Over the z-axis, this results in a detumbling time around 3 times as large, while for the y-axis a detumbling time of 4 times the detumbling time of a fully conductive object is found.

As can be seen from Figures 4.21 and 4.23, the rotational velocities converge to zero over time, and since there was no initial angular velocity over the x-axis and no torque present on the x-axis, the total angular velocity will converge to zero, as is presented in Figure 4.24.

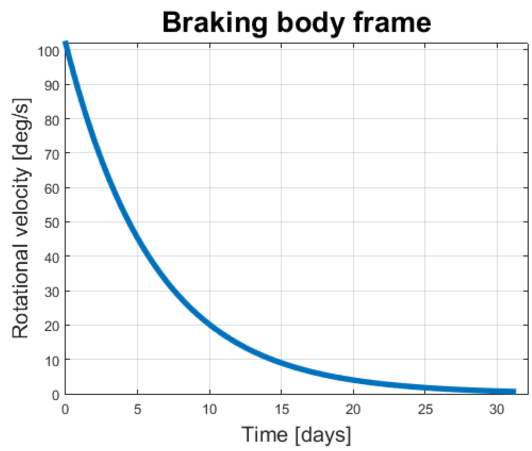

Figure 4.24: Angular velocity of the double silo in the body frame

Finally, since both angular velocities are perpendicular to the magnetic field working on the object, the object will not realign itself over time, but will remain in its initial position, as can be seen in Figure 4.25.

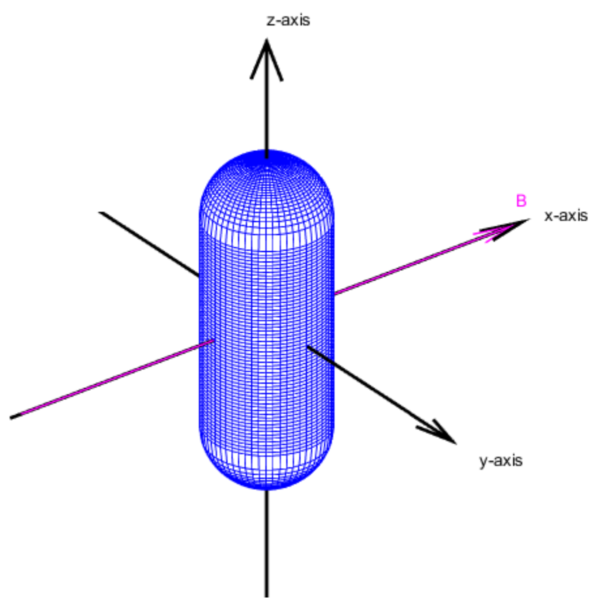

Figure 4.25: Influence of magnetic field on the initial position of the double silo

4.3. CONCLUSION

The model is verified for both basic shapes, being the cylindrical shell and the spherical shell, together with a more complex shape, being the double silo. As a result, the Kosmos-3M upper stage shape can be used with confidence as an input for the Magnetic Tensor model. More specifically, a 3D frame model of the Kosmos-3M second stage will be designed, which defines the Magnetic Tensor.

Furthermore, the combination of the magnetic field vector and initial angular velocity vector, defines the new state to which the angular velocity vector converges over time. Chapter 5 will further investigate the influence of the magnetic field vector and the initial angular velocity vector on the detumbling mission.

5

Initial detumbling of Kosmos-3M second stages

In Chapter 4 the model to simulate the detumbling of uncooperative objects in LEO was tested and verified by using basic shapes. In this Chapter the shape of the Kosmos-3M upper stage is used as input in the model, together with a revision of the input parameters in order to better represent the real-life situation in orbit. Specifically, this Chapter focuses on the position of the magnetic field vector relative to the chaser fixed frame in which the target rotates and it is shown that for the ideal situation, when the magnetic field vector and angular velocity vector are perpendicular, that the Kosmos-3M second rocket stage can be detumbled in the space of 7 days.

5.1. The Kosmos-3M second stage and input parameters

In order to simulate the detumbling of the Kosmos-3M second stage, the shape of the upper stage needs to be approximated by the use of a frame model. In Figures 5.1 and 5.2 the shape of the Kosmos-3M upper stage is approximated by using, respectively, 220 and 9060 nodes. When comparing this model to Figures 2.6 and 2.7, the major noticeable difference is the absence of the fuel cylinders, which have been excluded due to the difficulties in approximating a shape by the use of a mesh.

The first noticeable change compared to the objects in Chapter 4 is that the CoG and thus the reference frame does not lie precisely in the center of the object, as defined in Table 2.1. This change will not affect the Magnetic Tensor, but does affect the detumbling process, as will be further discussed in this and subsequent chapters.

Before the detumbling of the Kosmos-3M can be simulated, first all the input parameters need to be revised, since certain assumptions have been made in Chapter 4 in order to simplify the simulations. In Chapter 4 only crude estimations of some of the parameters were used, therefore, these parameters will need to be properly estimated in order to match the reality better.

First of all, the electric conductivity, σ, was calculated for aluminium at room temperature, which is not the case in space.

As stated in Chapter 2, objects in LEO can get as as cold as 116 Kelvin or as warm as 395 Kelvin. The temperature affects the conductivity of the materials, as it will fluctuate as the satellite orbits the Earth and the Earth orbits the sun. For the simulation, the temperature could be set as time dependent, however, this would require a Magnetic Tensor to be computed at every time instant, leading to computation times exceeding a week. Therefore, an average temperature of 255 Kelvin is chosen as the temperature of the Kosmos-3M upper stages. In Equation (5.1) the dependence of electrical resistivity on temperature is presented.

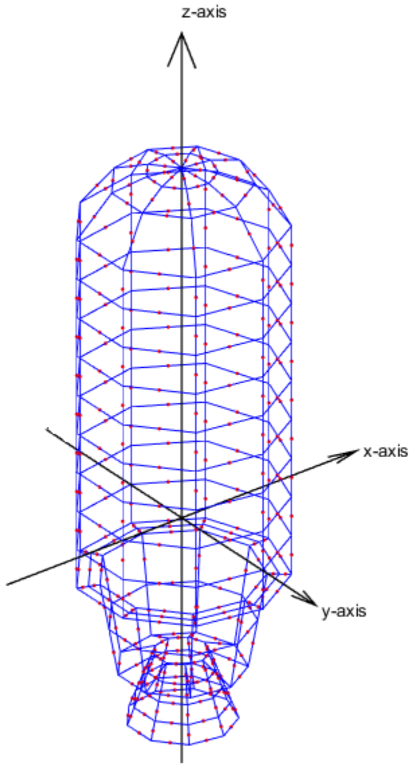

Figure 5.1: Frame model of the Kosmos-3M upper stage with 220 nodes

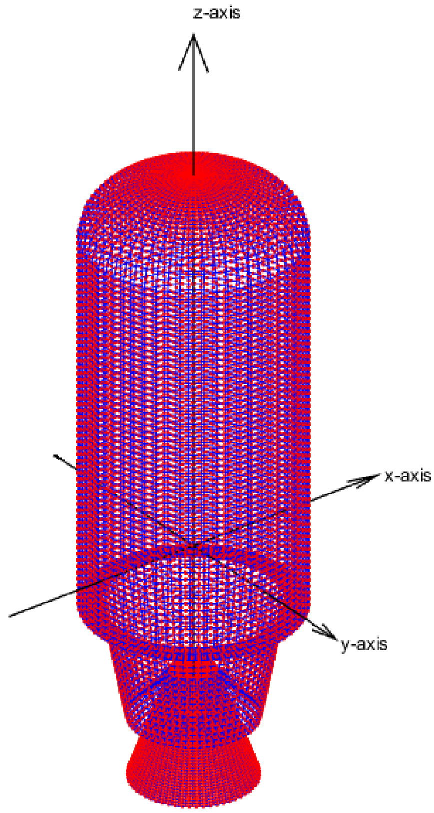

Figure 5.2: Frame model of the Kosmos-3M upper stage with 9060 nodes

$$\rho = \rho_0 \left(1 + \alpha_T \left(T - T_0\right)\right) \tag{5.1}$$

Where ρ is the electrical resistivity, ρ_0 is the electrical resistivity at room temperature, α_T is a temperature coefficient which is dependent on the material (aluminium for this case), and T and T_0 are the actual and room temperatures. The values of the unknowns can be found in Table 5.1.

Table 5.1: Parameters that influence the electrical conductivity of the upper stage

T_0	293.15	[K]
T	255	[K]
α_T	0.00429	[-]
ρ_0	2.6510^{-8}	$[\Omega m]$

The electrical conductivity can then be found by using Equation (5.2):

$$\sigma = \frac{1}{\rho} = 4.512\ 10^7\ \frac{S}{m} \tag{5.2}$$

Comparing this electrical conductivity coefficient to the one used in Chapter 4 shows that in a colder environment aluminium becomes more conductive, which results in a bigger electrical conductivity coefficient. In turn, this will have a positive influence in terms of detumbling time.

Secondly, the minimum distance between the chaser and the target needs to be defined, which will influence the strength of the magnetic field.

The Kosmos-3M rocket as modelled is 6.9159 m tall, however, it will be rotating over its CoG. The maximum length from the CoG to any part of the outer shell of the object can be found by using the data in Table 2.1 and equals 4.41 m, which means that depending on the angular velocity of the object, the magnetic coil needs to be located at least 4.41 meter from the CoG of the object. Adding some safety factor to it, this means that the chaser will be located at a distance of 5 meter or more from the target.

The magnetic field that will be used can then be determined. For initial detumbling, the maximum configuration of the coil will be used as defined in Chapter 3, which means it will have a radius of 1 meter and 500 windings.

Thirdly, when comparing the Magnetic Tensor of the double silo based on Kosmos-3M upper stage dimensions versus the one using Ariane 4 H10 upper stage dimensions, a large difference is found. This is due to the fact that the thickness of the skin was given an arbitrary value of 5 cm, while in fact it equals 5.08 mm, which will make the Magnetic Tensor considerably smaller, leading to longer detumbling times.

And finally, the Kosmos-3M rockets can be tumbling up to speeds of 12 rpm and are known to mostly rotate about their major axis of inertia which is their diametral axis, meaning that in the chaser fixed frame, the object will rotate over the x- and y-direction, while only a small or even no angular velocity is present over the z-axis. Furthermore, in Chapter 4, different tumbling speeds over different axis were simulated, where all initial tumbling speeds were set as 12 rpm, while for the real mission to detumble the Kosmos-3M mission the total angular velocity will equal 12 rpm.

All the initial input parameters for the model of the Kosmos-3M upper stages can then be found in Table 5.2.

Table 5.2: Input parameters Kosmos-3M upper stage

R_{cyl}	1.2	$[m]$
L_{cyl}	4.39	$[m]$
L_{tr}	1.32	$[m]$
L_{COM}	3.71	$[m]$
e	0.00508	$[m]$
$\vec{B}$	[162.4 0 0]	$[\mu T]$
$\vec{\omega}$	[50.63 50.63 7.53]	$[deg/s]$
σ	$4.512\ 10^7$	$[S/m]$
I	[5592.2 5592.2 1442.9]	$[kgm^2]$
m_{con}	25	[%]

5.2. DIFFERENT CONFIGURATIONS OF THE UPPER STAGE

Before modelling the actual Magnetic Tensor of the Kosmos-3M upper stages, first the Magnetic Tensor is calculated where a skin thickness of 0.05 m is used and the object is assumed to be fully conductive, in order to compare it to the Magnetic Tensor of the double silo in Equation (4.29).

Due to the increase in complexity of the shape, the number of nodes has also been increased to 9060 in order to ensure that the Magnetic Tensor has converged and that the error is small.

In Equation (5.3) the Magnetic Tensor, modelled by using a frame model with 9060 nodes and a skin thickness of 0.05m, is presented.

$$M_{Kosmos_{ver}} = \begin{bmatrix} 7.8776 & 0 & 0.0563 \\ 0 & 7.8776 & 0 \\ 0.0563 & 0 & 2.4953 \end{bmatrix} 10^7 Sm^4 \tag{5.3}$$

Due to the shape of the object and the fact that it is no longer symmetric over its diametral axes, the Magnetic Tensor has two non-zero elements besides the diagonal elements, representing this asymmetry.

When comparing this Magnetic Tensor, to that of the double silo in Chapter 4 it can be concluded that they are of the same order of magnitude. Similar to the comparison of the Magnetic Tensors of the double silo and the cylinder, the Magnetic Tensor of the Kosmos-3M first two elements of its diagonal are larger and the third element is smaller due to the increase in length of the object.

The Magnetic Tensor for the Kosmos-3M upper stage, with input parameters as defined in Table 5.2, will be smaller, since the skin thickness decreases by a factor ten, which will also drastically increase the detumbling time. The Magnetic Tensor, where the Kosmos-3M upper stage is entirely made out of aluminium, can be found in Equation (5.4).

$$M_{Kosmos_{100}} = \begin{bmatrix} 10.318 & 0 & 0.0737 \\ 0 & 10.318 & 0 \\ 0.0737 & 0 & 3.268 \end{bmatrix} 10^6 Sm^4 \tag{5.4}$$

As can be seen, is Equation (5.3) around the order of ten times larger than Equation (5.4), which is the result of the skin thickness decreasing.

In order to model the Magnetic Tensor to better represent the real object, 25% of the bars in the frame model will be considered conductive materials, as was defined in Chapter 2. This will be included in the model by using a random generator, which generates uniformly distributed random numbers, where the value $'1'$ means conductive material and a $'0'$ means non-conductive material. The non-conductive materials will be assigned a small electric conductivity, while the others are assigned the value of the electric conductivity as found in Table 5.2. The bars that are not made out of conductive material are not assigned a zero value, since everything can be considered a conductor, with for example PET having an electrical conductivity of $10^{-21} S/m$.

This results in a smaller Magnetic Tensor, as presented in Equation (5.5).

$$M_{Kosmos_{25}} = \begin{bmatrix} 2.5162 & -0.1122 & -0.0359 \\ -0.1122 & 2.5162 & -0.0275 \\ -0.0359 & -0.0275 & 0.8043 \end{bmatrix} 10^6 Sm^4 \tag{5.5}$$

For Equation (5.5), the random generator, as discussed previously, has assigned which bars are considered conductive and which are not, meaning the bars are randomly distributed over the body. However, for the real upper Kosmos-3M stage, most of the conductive material is located in the cylinder, with only a fraction located at the top and bottom parts. Therefore, a new and final Magnetic Tensor is modelled where 75% of the conductive material is located in the cylinder, and the other 25% is randomly distributed over the remaining elements of the body.

$$M_{Kosmos} = \begin{bmatrix} 1.9993 & 0.0835 & 0.0377 \\ 0.0835 & 1.9153 & -0.0288 \\ 0.0377 & -0.0288 & 1.0022 \end{bmatrix} 10^6 Sm^4 \tag{5.6}$$

As can be seen are the first two elements on the diagonal of the Magnetic Tensor smaller than in Equation (5.5), while over the z-direction it is bigger. This is due to the fact that the conductive part of the object resembles the shape of a cylinder, virtually decreasing the length of the object, due to most of the conductive materials located in the cylindrical part, with the other conductive material located randomly at the top and bottom part of Figure 5.2.

It can be concluded that the Magnetic Tensor in Equation (5.6) best represents the Kosmos-3M upper stage and will, therefore, be used in this and subsequent Chapters to model the detumbling of the rocket stage.

Now that the Magnetic Tensor of the Kosmos-3M upper stage has been finalised, the detumbling can be simulated. Using the values as in Table 2.1, the detumbling over the y- and z-axis is presented in Figures 5.3 and 5.4.

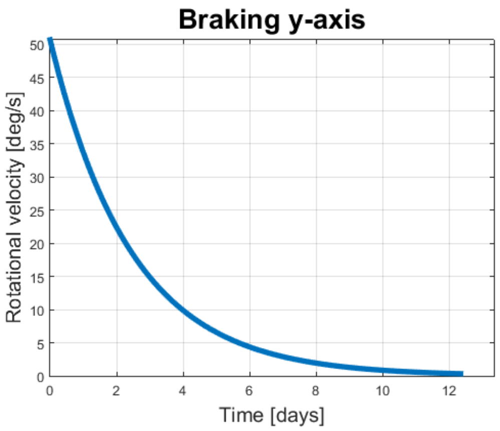

Figure 5.3: Detumbling of Kosmos-3M upper stage over the y-axis

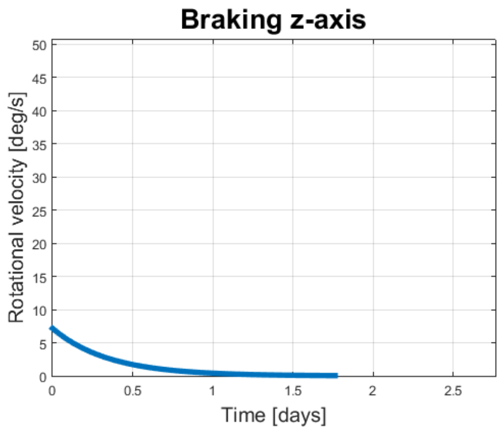

Figure 5.4: Detumbling of Kosmos-3M upper stage over the z-axis

As expected, the angular velocity over the x-axis is not damped, which is similar to the detumbling of the sphere in Chapter 4. Furthermore, the angular velocity over the z-axis is already damped after 2 days, while for the y-axis it takes close to 12 days. This is both due to the difference in initial detumbling speed and due to the fact that the angular velocity in the z-direction is perpendicular to the along track direction in which the magnetic field vector lies, which is comparable to the detumbling mission of the double silo as described in Chapter 4.

Furthermore, due to the detumbling by the ECB and the damping of the angular velocity over the y- and z-direction, the object realigns itself over time, as can be seen in Figure 5.5.

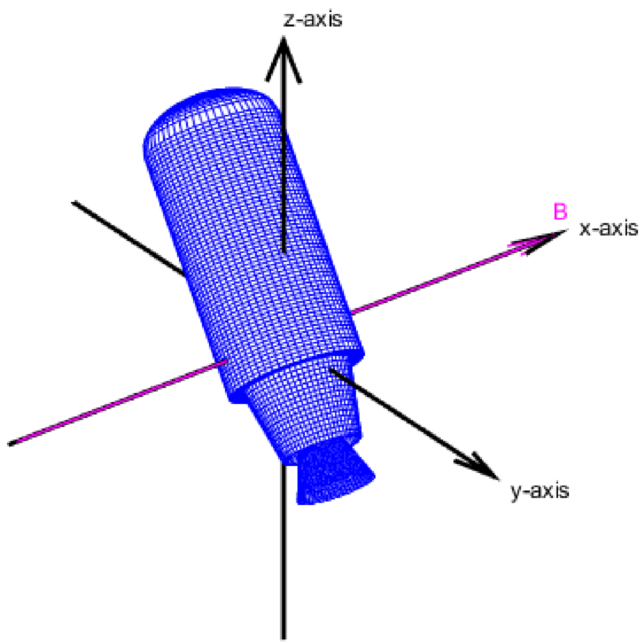

Figure 5.5: Influence of magnetic field on the initial position of the Kosmos-3M upper stage

It can thus be concluded that detumbling a real object in space, in this case the Kosmos-3M second stage, is possible in a reasonable time frame of 12 days. However, the angular velocity over the x-axis is not damped, which means that a subsequent detumbling mission is necessary. Additionally, the magnetic field created by the ECB carried by the chaser can be pointing in a different direction, thus influencing the detumbling process. Therefore, Section 5.3 will investigate how detumbling is influenced when the magnetic field vector points in different directions.

5.3. THE DETUMBLING TIMES OF THE KOSMOS-3M UPPER STAGE

It is possible to detumble the Kosmos-3M upper stage given the initial position as given in Table 5.2. However, the magnetic field vector can also be pointing in a different direction than shown in Figure 5.5, which will affect the torque vector and thus the detumbling time. Therefore, this Section will look at how the placement of the electromagnetic coil relative to the reference frame influences the detumbling time.

This will help formulate an answer to the question whether the state and angular velocity of the object need to be known beforehand and thus a prior detection phase needs to be performed before the ECB is turned on, or if the object is detumbled after a certain period of time regardless of where the Magnetic Field vector is pointing. This would be ideal, since it would allow the ECB to be used on wide variety of objects with different rotation rates over different axis, which would be a big step forward in finding a solution to the debris problem.

First the magnetic field vector, $\vec{B}$ will be altered and the resulting detumbling time analysed for ten different cases. In Table 5.3 the different magnetic field vectors used for this analysis are presented.

Table 5.3: Selection of magnetic field vectors

Case	Magnetic field vector $[\mu T]$
1	$[162.4\ 0\ 0]^T$
2	$[0\ 162.4\ 0]^T$
3	$[0\ 0\ 162.4]^T$
4	$[81.2\ 81.2\ 114.8]^T$
5	$[81.2\ {-81.2}\ 114.8]^T$
6	$[81.2\ {-81.2}\ {-114.8}]^T$
7	$[-12\ {-12}\ 161.5]^T$
8	$[0.2\ 0.2\ 162.4]^T$
9	$[114.2\ 114.2\ 17]^T$
10	$[112.3\ 112.3\ 33.8]^T$

The first three cases have the magnetic field vector pointing in the positive direction along the major three axis, with the first case already simulated in Section 5.2.

The second case will be very similar to the first case, since the initial angular velocity over the x- and y-axis is the same, with the only difference being that not the angular velocity over the y-axis is damped, but the one over the x-axis. Simulation confirmed that the object is detumbled over the x- and z-axis and that the detumbling times match that of case 1 exactly.

For the third case, both the angular velocity over the x- and y-direction are perpendicular to the magnetic field, leading to both angular velocities being damped completely, as can be seen in Figures 5.6 and 5.7. This only leaves the angular velocity over the z-axis, which is not damped over time since the magnetic field and the rotation axis are parallel.

The fourth case is different since the magnetic field vector does not point along the major axis, but instead is located at a certain angle from those axes. In this case, the magnetic field vector lies

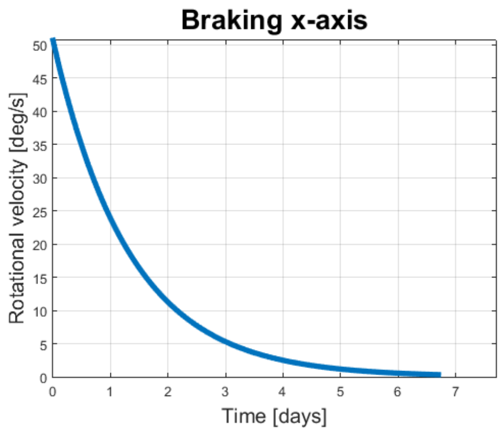

Figure 5.6: Detumbling of Kosmos-3M upper stage for case 3 over the x-axis

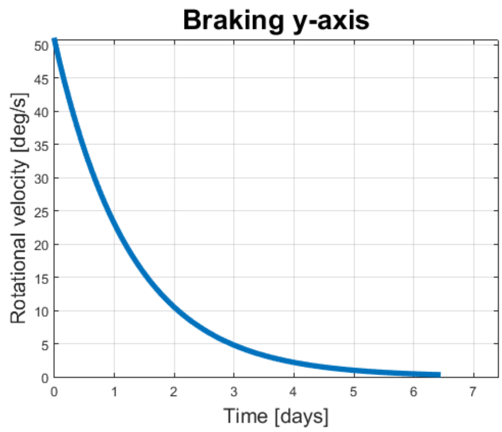

Figure 5.7: Detumbling of Kosmos-3M upper stage for case 3 over the y-axis

at an angle of 45 degrees from every axis. And as can be seen in Table 5.3, this leads to a magnetic field in x, y and z-direction, where the magnetic field in the z-direction is the square root of the two others and the resulting magnetic field vector equals 162.4 μT.

The detumbling simulation for the fourth case over the x and z-axis can be found in Figures 5.8 and 5.9, where the simulation of the ECB over the y-axis is equal to the one over the x-axis, and is thus not shown. As can be seen from the two figures, the angular velocity does not converge to zero, but instead converges to a new steady state. For the x- and y-axis the angular velocity is damped to 10 degrees per second, while the angular velocity over the z-axis increases to 13 degrees per second, resulting in an angular velocity of around 18 degrees per second. This is due to the fact that the object aligns itself over time to the magnetic field vector, resulting in the torques generated converging to zero, which is similar to the cylinder case discussed in Chapter 4.

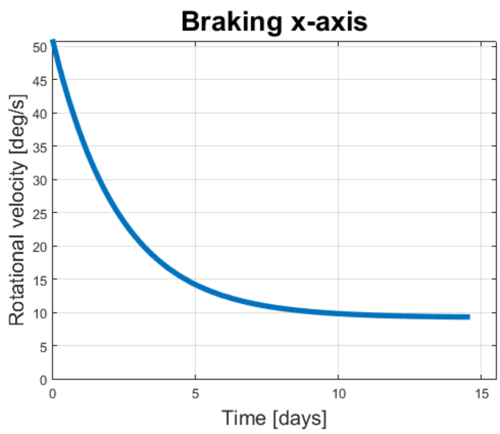

Figure 5.8: Detumbling of Kosmos-3M upper stage for case 4 over the x-axis

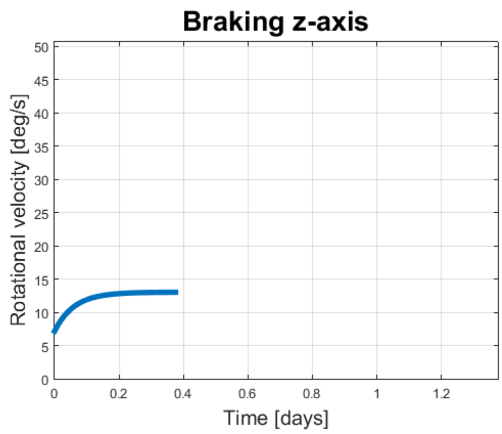

Figure 5.9: Detumbling of Kosmos-3M upper stage for case 4 over the z-axis

Case 5 is similar to the fourth case, with the difference that the magnetic field vector is pointing to another quadrant of the reference frame. For the fourth case, the resulting angular velocity vector was located at an angle smaller than 45 degrees from the magnetic field vector, leading to the object aligning itself over time to the magnetic field vector. However, for the magnetic field vector lying in quadrants which are not the negative of the quadrant in case 4, this angle will be bigger than 45 degrees, leading to the object not aligning itself, but instead damping the angular velocity over all axes. The angular velocity over the x and z axis are shown in Figures 5.10 and 5.11. It can be concluded that the total angular velocity is damped in under 10 days, which means it is ready for ADR.

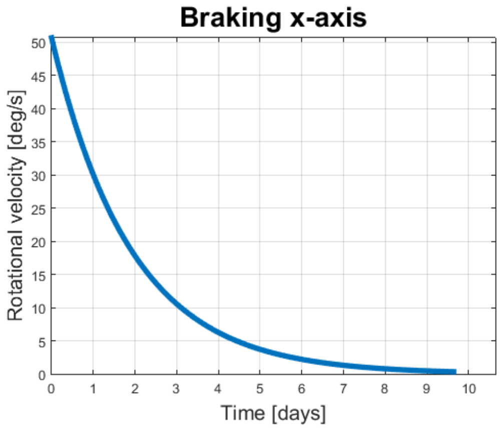

Figure 5.10: Detumbling of Kosmos-3M upper stage for case 5 over the x-axis

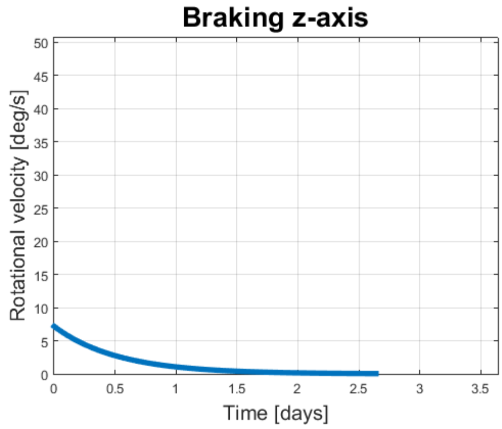

Figure 5.11: Detumbling of Kosmos-3M upper stage for case 5 over the z-axis

Case 6 is similar to case 5, except that the angle between the magnetic field vector and the angular velocity vector is close to 90 degrees, meaning that it will detumble the object faster. For case 6, the angular velocity over the y-axis converges to zero after 9 days, which is also the total detumbling time for the object.

For case 7, the magnetic field vector lies in the plane perpendicular to the initial angular velocity vector. This plane represents the optimal configuration of the ECB for the parameters as described in Table 5.2. Case 7 should thus lead to the fastest detumbling time, which is presented in Figures 5.12 and 5.13. The angular velocity over all axes is damped after 6.8 days. When comparing this detumbling time to the others, it is found that case 3 detumbles the object faster over the x- and y-axis. However, it does not damp the angular velocity over the z-axis, which means that the total angular velocity does not converge to zero. This leads to the conclusion that case 7, and all other cases where the magnetic field vector is perpendicular to the angular velocity vector, are the optimal solutions to detumble the Kosmos-3M rocket over all axis.

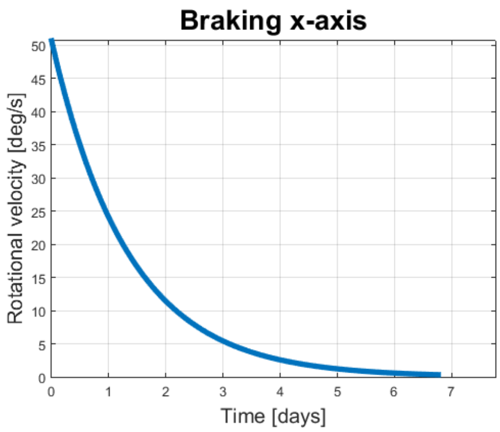

Figure 5.12: Detumbling of Kosmos-3M upper stage for case 7 over the x-axis

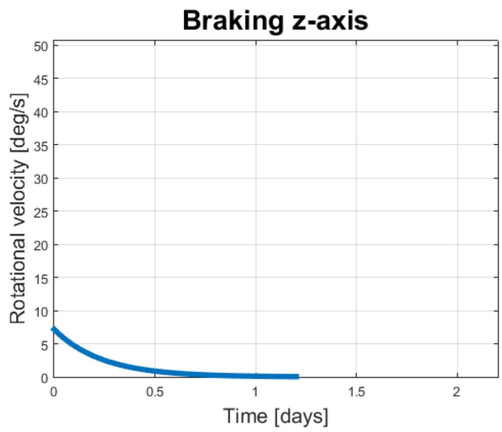

Figure 5.13: Detumbling of Kosmos-3M upper stage for case 7 over the z-axis

Other interesting cases present themselves when the magnetic field vector is close to parallel with one of the major axes of rotation. In case 8, the magnetic field vector is near parallel with the z-axis in the orbital reference frame. The result of the simulation can be found in Figure 5.14. As can be seen, the angular velocity over the z-axis converges to a similar value as in case 4, only for this case the detumbling time is a lot longer before it converges.

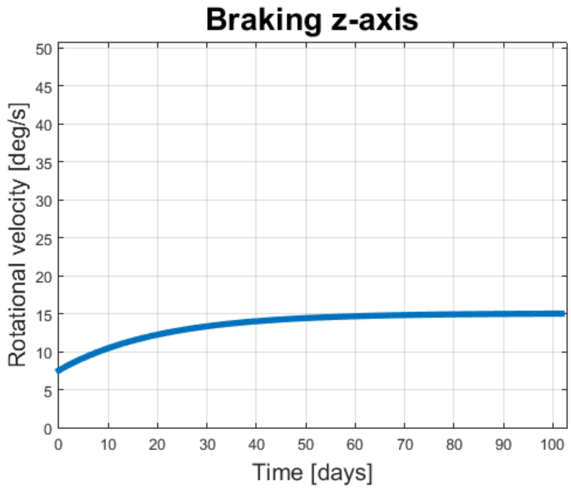

Figure 5.14: Detumbling of Kosmos-3M upper stage for case 8 over the z-axis

For case 9, the resulting magnetic field vector and the initial angular velocity vector perfectly align, which leads to no torques being generated and thus no angular velocities being damped.

If there is only a small angle between these two vectors, the objects angular velocity vector will align itself to the magnetic field vector as presented in case 10, resulting in a new steady state, where the rotational motion is only damped slightly. Case 10, thus, represents the case where the magnetic field vector is close to parallel to the initial angular velocity vector, and is presented in Figures 5.15 to 5.17.

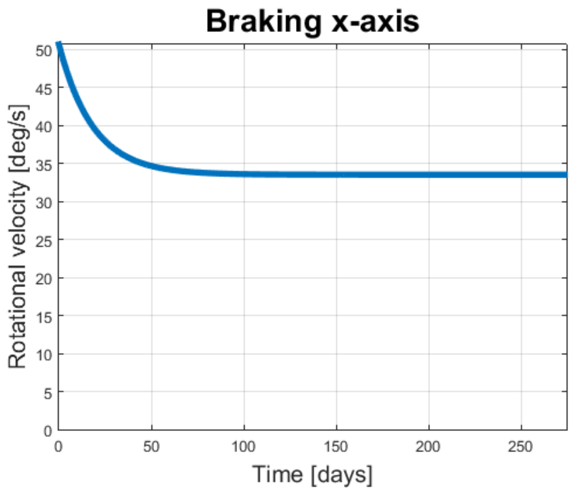

Figure 5.15: Detumbling of Kosmos-3M upper stage for case 10 over the x-axis

It can be concluded that the position of the initial acceleration vector relative to the resulting magnetic field vector has a large influence on the effectiveness of the ECB. The ten cases paint a clear picture as to how the detumbling time is affected in terms of the relative position between these two vectors, but an overview is still missing.

Therefore, the rotational velocity the model converges to for magnetic field vectors in fixed planes is plotted over 360 degrees in order to provide an overview of the detumbling times. Multiple planes, in which the magnetic field vectors lie, are used in order to get a 3D 360 degrees overview of

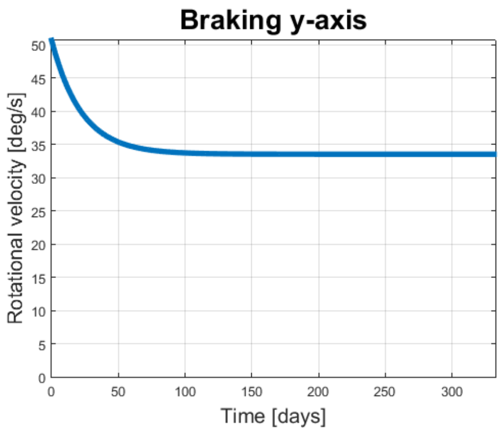

Figure 5.16: Detumbling of Kosmos-3M upper stage for case 10 over the y-axis

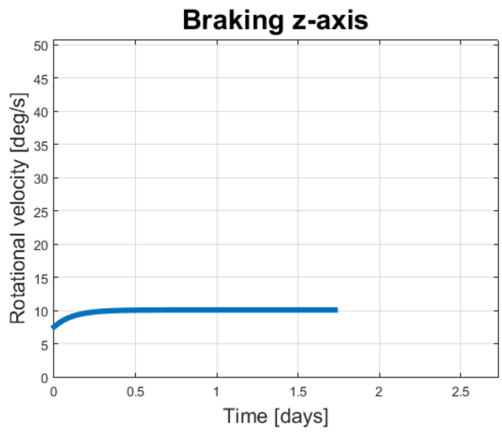

Figure 5.17: Detumbling of Kosmos-3M upper stage for case 10 over the z-axis

how effective the ECB is to detumble the Kosmos-3M second stage.

Figures 5.18 and 5.19 present an overview of the converged rotational velocity and matching detumbling time where the magnetic field vector plane is rotated 0 degrees over the y-axis. Since the plane is rotated 0 degrees over the y-axis, it is perpendicular to the y-axis, resulting, for the entire 360 degrees, in the angular velocity over the y-axis being damped completely. On the other hand, the angular velocity over the x-axis and z-axis are only damped in certain areas, while in other areas it even increases. Figure 5.18 shows that when the magnetic field vector is under a positive angle, relative to the yz-plane of around 90 degrees until around 180 degrees, the rotational velocities over every axes are damped to zero. Furthermore, it also shows that the converged angular velocity from zero to 180 degrees, perfectly matches that of 180 to 360 degrees.

Another important aspect besides the converged rotational velocity is the time it takes the ECB to detumble the target to that velocity, which is presented in Figure 5.19. The detumbling time for the rotational motion around the y- and z-axis does, relatively, require less time, compared to the angular velocity over the x-axis, which can require detumbling times up to 3000 days or close to 9 years, which is due to the fact that the magnetic field vector approaches the x-axis of rotation at certain instances. Around 180 degrees the figure shows some peaks and valleys. The first valley goes exactly to zero for an angle of 180 degrees, which corresponds to the point where the angular velocity over the x-axis is parallel to the magnetic field vector, meaning no torque is being generated on the x-axis. The first high peak is the result of the angle between the magnetic field vector and the x-axis being close, but not parallel, leading to extremely high converge times. The second peak, located around 180 degrees, is due to the fact that the magnetic field vector and the rotational velocity vector are close to parallel leading to long converge times. No additional valley is to be found around 180 degrees, since the magnetic field vector and the rotational velocity vector never truly align.

For the second set of converged detumbling velocities and times, the angle of the plane over the y-axis equals 45 degrees, which results in the converged rotational velocities over both x- and y-axis to match perfectly for the total range of 360 degrees, which can be seen in Figure 5.20. This is due to the fact that the magnetic field vectors are located precisely in the middle of the x- and y-axis. Furthermore, the detumbling times for the angular velocity over the x- and y-axis in Figure 5.21 follow the same trend. The second valley and accompanying peaks again correspond to the magnetic field vector being perpendicular to both x- and y-axis, while the first peak is located at some degrees from 180, equal to the square root of 6, with 6 degrees being the rotation angle of the angular velocity vector over the xy-plane.

The third set of converged detumbling velocities and times, presented in Figures 5.22 and 5.23, with the angle of the plane over the y-axis equalling 90 degrees, results in a copy of the first set,

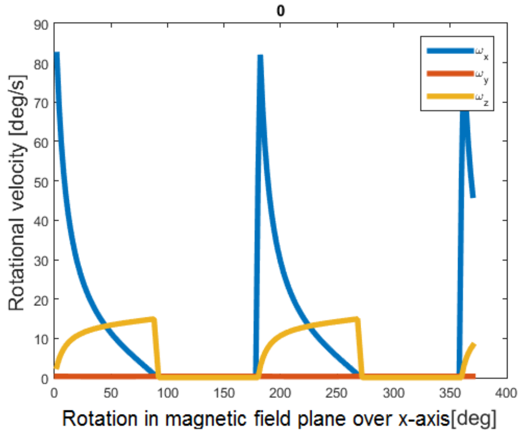

Figure 5.18: Converged rotational velocity for a magnetic field vector plane at 0 degrees over the y-plane

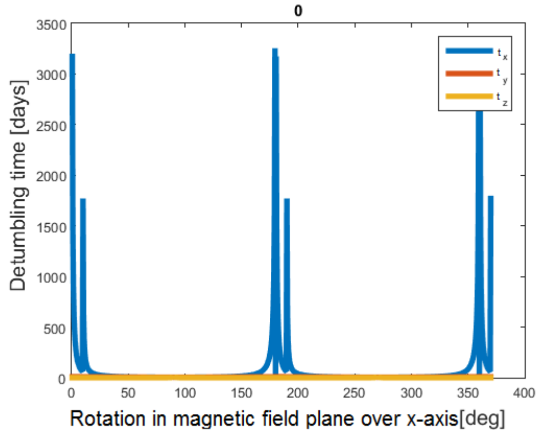

Figure 5.19: Detumbling time in a magnetic field vector plane at 0 degrees over the y-axis

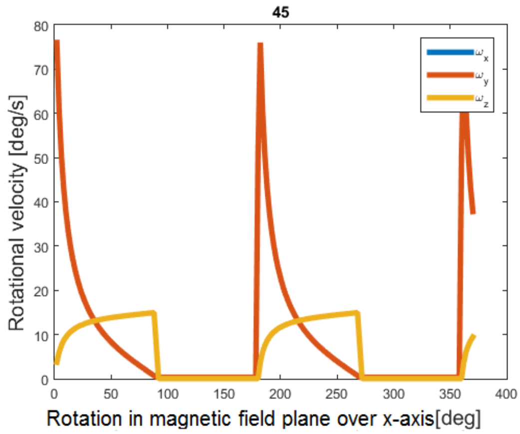

Figure 5.20: Converged rotational velocity for a magnetic field vector plane at 45 degrees over the y-plane

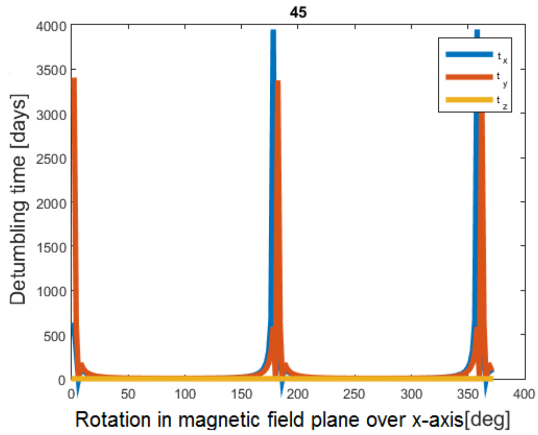

Figure 5.21: Detumbling time in a magnetic field vector plane at 45 degrees over the y-axis

apart from the fact that now the trend over the x-axis equals that over the y-axis of the first set and vice-versa.

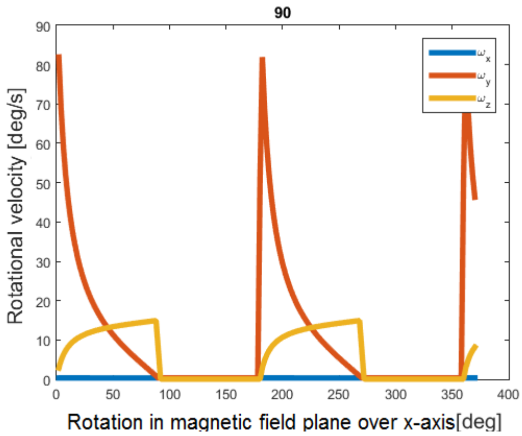

Figure 5.22: Converged rotational velocity for a magnetic field vector plane at 90 degrees over the y-plane

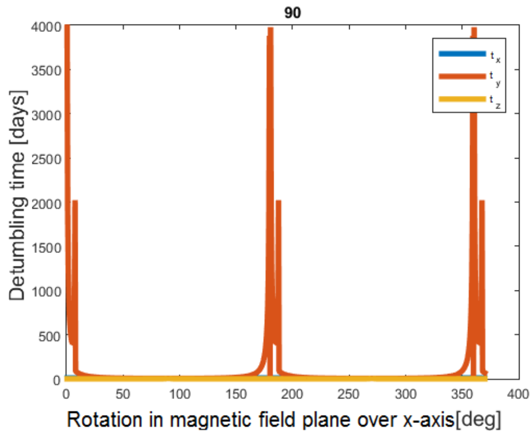

Figure 5.23: Detumbling time in a magnetic field vector plane at 90 degrees over the y-axis

Set four, shown in Figures 5.24 and 5.25, presents a case where the angle of the plane over the y-axis equals 135 degrees, which means that the magnetic field vector is close to perpendicular to the rotational velocity vector, leading to almost all rotational velocities being damped completely over the entire 360 degrees. The peak for both detumbling time and rotational velocity is due to the fact that the magnetic field vector and the rotational velocity vector are close, but not perfectly aligned.

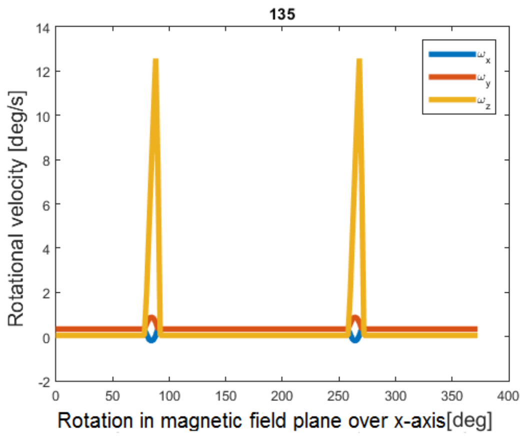

Figure 5.24: Converged rotational velocity for a magnetic field vector plane at 135 degrees over the y-plane

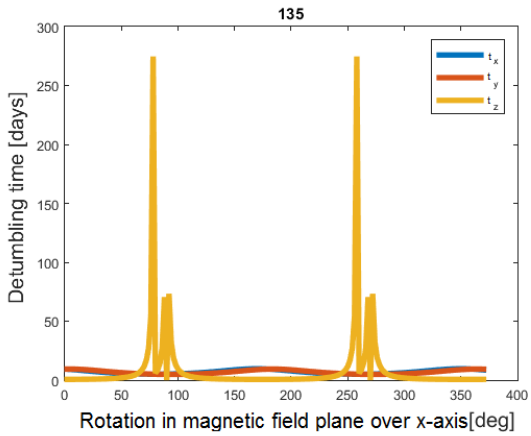

Figure 5.25: Detumbling time in a magnetic field vector plane at 135 degrees over the y-axis

Finally, the fifth set presents the case where the angle of the plane over the y-axis equals 180 degrees. When comparing Figures 5.26 and 5.27 with Figures 5.18 and 5.19 it can be seen that they are mirrored, which is as expected, since the two planes are located at an angle of 180 degrees from each other, meaning that they are at an equal but opposite distance from the angular velocity vector.

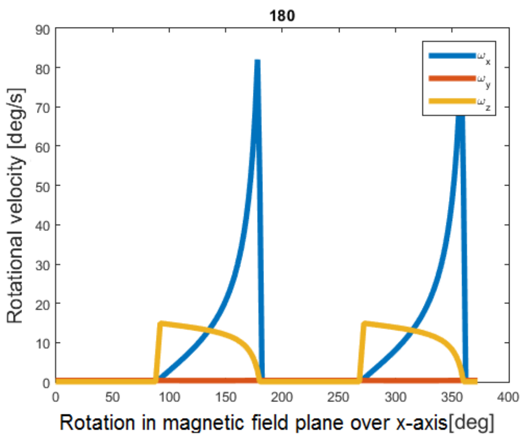

Figure 5.26: Converged rotational velocity for a magnetic field vector plane at 180 degrees over the y-plane

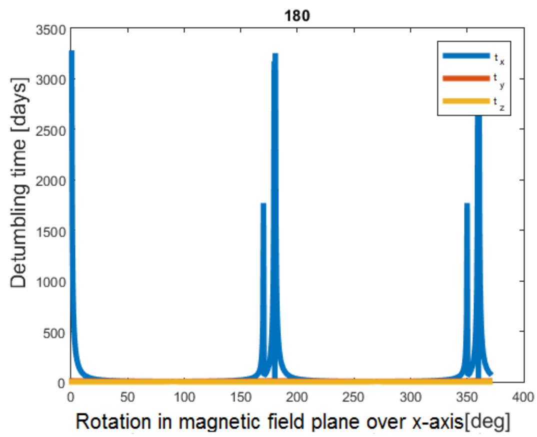

Figure 5.27: Detumbling time in a magnetic field vector plane at 180 degrees over the y-axis

5.4. CONCLUSION

The Kosmos-3M second stage can be detumbled with the use of an ECB in a span of 7 days when the magnetic field vector is perpendicular to the initial angular velocity vector. However, the detumbling time is strongly influenced by the position of the ECB relative to the target. Depending on the position of the magnetic field vector the angular velocity either converges to zero or converge to a new steady state over time. Furthermore, when the magnetic field vector approaches any of the major axes of rotation, or the angular velocity vector, long detumbling times are measured, which exponentially increase with diminishing angle between the angular velocity vector and the magnetic field vector.

It can be concluded that in order to detumble the Kosmos-3M second stage in a reasonable amount of time (<30 days) a prior state determination mission is necessary, or that the chaser must reposition itself over time in order to detumble the target completely. Chapter 7 will simulate the possibilities of realigning the chaser during the detumbling mission and optimize said realigning in order to damp all angular velocities independent of the initial position of the chaser and the target.

However, in this and previous chapters, other magnetic interactions have been ignored for the sake of simplicity. In Chapter 6 these interactions will be investigated and their influence on the detumbling mission assessed. As a result, a final detumbling of the Kosmos-3M second stage can be simulated using more accurate data in Chapter 7.

6

MAGNETIC INTERACTIONS

In Chapter 5 the Kosmos-3M was detumbled for a simplified model that neglected certain forces, torques and perturbations present when using an electromagnet as ECB.

The chaser and target fly in formation for the duration of the mission, with formation flying being a proven technology. However, the electromagnet presents a new factor, influencing this formation. Therefore, this Chapter will focus on the magnetic interactions, besides eddy currents, in order to assess their influence on the detumbling mission. More specifically, the non-uniformity of the magnetic field will be discussed, showing that due to the non-uniformity the elements of the Magnetic Tensor decrease in size, leading to an increase in detumbling time.

Furthermore, the interaction of the Earth's magnetic field with the chaser and target is simulated in order to confirm that Attitude Determination and Control Systems (ADCS's) are capable of counteracting the torques generated on the chaser and the influence on the detumbling time will be assessed.

Finally the interaction of the magnetic field generated by the ECB and ferromagnetic materials present in the Kosmos-3M rocket is assessed. A first estimation of the torques shows that it will have a relatively small influence on the detumbling mission.

6.1. NON-UNIFORMITY OF THE MAGNETIC FIELD

In Section 2.2 it was discussed that by using a single coil which has a limited diameter due to launch and weight constraints, no uniform magnetic field can be achieved, meaning that the magnetic field vectors are not parallel and that the magnetic field strength varies over the length of the target.

As a result, the non-uniformity of the magnetic field influences the ECB mission. In previous chapters, it was assumed that the magnetic field was of uniform strength along the entire object and that the magnetic field lines were parallel. The value of the magnetic field strength was, for each shape, chosen to be the magnetic field strength at the CoG of the object, while the magnetic field strength at the top and bottom are significantly different.

The non-uniformity cannot be incorporated in the magnetic field vector, since it varies over the surface of the target. Therefore, an efficiency factor μ_e for the Magnetic Tensor is introduced, which represents this uniformity.

However, modelling this efficiency factor is a complex and intensive process. Therefore, it is chosen to only focus on the efficiency factors of the Magnetic Tensor's diagonal, as shown in Equation (6.1). Ignoring the influence of the efficiency factors of the other elements of the Magnetic Tensor only leads to a small error since the size of those other elements are less than 1% of the size of the diagonal elements. As a result, the efficiency factors for the diagonal will still introduce a good approximation of the Magnetic Tensor under a non-uniform magnetic field.

$$M_e = \begin{bmatrix} \mu_{e_{x,y}} M_{11} & M_{21} & M_{31} \\ M_{12} & \mu_{e_{x,y}} M_{22} & M_{32} \\ M_{13} & M_{23} & \mu_{e_z} M_{33} \end{bmatrix} Sm^4 \tag{6.1}$$

N. Ortiz Gómez and S.J.I. Walker developed a relationship to model these efficiency factors, which shows that μ_e is dependent on the radius of the differential eddy current loop, R_0, and the distance between the chaser coil and the target and the shape and size of the target[28].

A non-homogeneous field acting upon a target is presented in Figure 6.1, where the red circle is the differential eddy current loop, R_0.

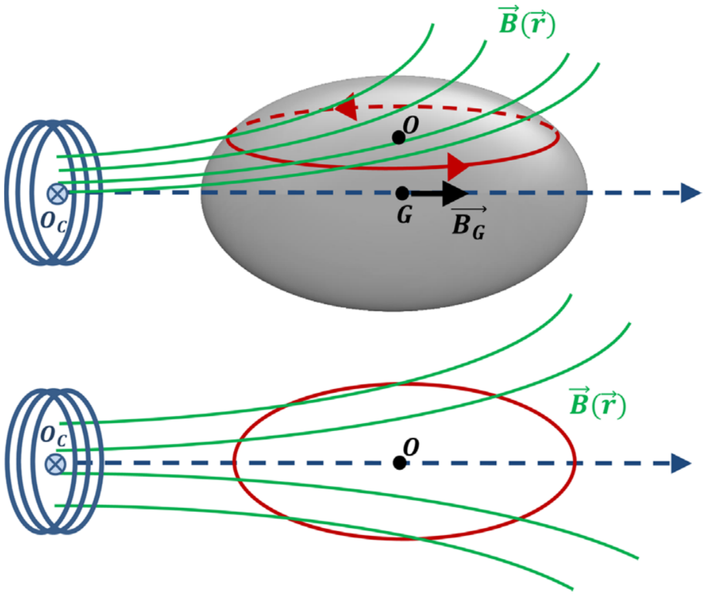

Figure 6.1: Non-homogeneous magnetic field on a quasi-spherical body[28]

$$\mu_e = \frac{M_{e_i}}{M_i} = \frac{\int_{V_0} \rho_e R_0^2 \,\mathrm{d}V_0}{\int_{V_0} R_0^2 \,\mathrm{d}V_0} \tag{6.2}$$

$$\mu_e = \int_{V_0} \frac{\vec{B}_0 \frac{\vec{B}_G}{B_G^2} R_0^2}{\int_{V_0} R_0^2 \,\mathrm{d}V_0} \,\mathrm{d}V_0 \tag{6.3}$$

Where $R_0 = \frac{2S_0}{L_0}$, S_0 is the surface area, L_0 is the longitude of the eddy current loop, V_0 is the volume of the electrical circuit and $\vec{B}_0$ and $\vec{B}_G$ are, respectively, the magnetic field in center of the eddy current loop in Figure 6.1 and in the CoG of the body.

Due to the symmetry of the Kosmos-3M rocket, there will be two efficiency factors, namely $\mu_{e-x,y}$ and μ_{e-z}. In order to get a clear overview of the influence of $\mu_{e-x,y}$ and μ_{e-z}, they will be modelled for a varying distance from the ECB to the Kosmos-3M rocket between 0 and 10 meters, the result of which can be found in Figure 6.2.

The trend line of μ_{e-z} is steeper than that of $\mu_{e-x,y}$, which is due to the fact that the Kosmos-3M rocket longest axis is along the z-axis, while its shortest axis is along its diametral axis, as presented in Figure 5.2. Since the object is longer about the z-axis, and the magnetic field vector is pointing along a diametral axis the variation in magnetic field at a short distance will be bigger, resulting in small efficiency factor, while at greater distance the influence of the non-uniformity rapidly diminishes. On the other hand, the efficiency factors for both x- and y- direction with a magnetic field

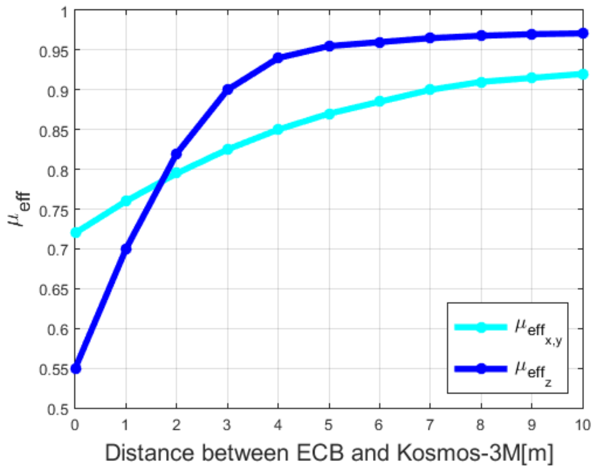

Figure 6.2: Influence of the non-uniformity of the magnetic field on the Magnetic Tensor

vector pointing in the z-direction has a flatter trend line, which is due to the fact that the diameter of the Kosmos-3M is smaller than its length.

The Magnetic Tensor simulated with the influence of the non-uniformity of the magnetic field then becomes:

$$M_{Kosmos} = \begin{bmatrix} 1.7394 & 0.0835 & 0.0377 \\ 0.0835 & 1.6663 & -0.0288 \\ 0.0377 & -0.0288 & 0.9521 \end{bmatrix} 10^6 Sm^4 \tag{6.4}$$

6.2. INTERACTION WITH EARTH MAGNETIC FIELD

Another factor that influences the detumbling of the Kosmos-3M by an ECB is the Earth's magnetic field, which affects both the detumbling of the target and the working of the chaser.

For the detumbling of the target, the contribution of the Earth's magnetic field means that there is an extra magnetic field creating eddy currents on the conductive surfaces of the Kosmos-3M, effectively changing the resulting magnetic field vector as defined in Chapter 5.

In order to estimate the influence and strength of the Earth's magnetic field an arbitrary orbit of a Kosmos-3M rocket will be used, with a height of 950 km and an inclination of 82.9 degrees, which are average values of the critical cloud as defined in Chapter 2 where the Kosmos-3M second stages reside.

An estimate of the ground track of a Kosmos-3M second rocket stage orbit can be found in Figure 6.3 in a Mercator projection with rotating Earth, where the orbit is assumed to have zero eccentricity, zero degrees in longitude of ascending node for the starting point and a zero degrees argument of periapsis.

Then, using the latitude and longitude values of Figure 6.3, the World Magnetic Model (WMM) can be used to calculate the Earth's magnetic field at a specific location and time. Using Matlab®, which has the WMM package pre-installed, the strength of the magnetic field can be found for the arbitrary orbit in Figure 6.3. The output of the function gives the magnetic field vector, horizontal intensity and total intensity of which the first and last can be found in Figures 6.4 and 6.5, plotted in a North-East-Down (NED) reference frame.

As can be seen from Figures 6.4 and 6.5 the total magnetic field varies between 17 and 40 μT and the biggest magnetic field strength is measured in the z-direction. In order to verify this result, the Earth's magnetic field strength can be approximated by[55]:

Figure 6.3: Arbitrary orbit of a Kosmos-3M second rocket stage for 5 orbital periods

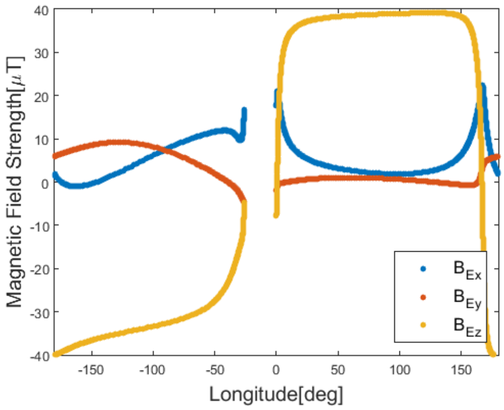

Figure 6.4: Strength Earth's magnetic field in the x-, y- and z-direction for an arbitrary orbit for one orbital period

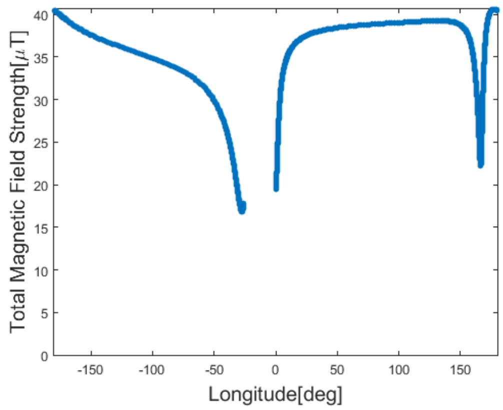

Figure 6.5: Total strength Earth's magnetic field for an arbitrary orbit for one orbital period

$$B_E = \frac{2M}{R_c} \tag{6.5}$$

Where M is the magnetic moment of the Earth, equalling 7.96 10^{15} Tm^3, and R_c is the distance from the center of the Earth to the spacecraft, equalling 7321.14 km.

As a result the Earth's magnetic field strength at a distance of 950 km equals:

$$B_{E_{950}} = \frac{2M}{R_c} = 40.5702\mu T \tag{6.6}$$

It can thus be concluded that the model as presented in Figures 6.4 and 6.5 is verified.

Furthermore, when comparing these values to that of the magnetic field vector of the ECB presented in Chapter 5, it can be concluded that they are of the same order of magnitude and that the

Earth magnetic field will thus have an impact on the detumbling of the Kosmos-3M second stage, which shall be further discussed in Chapter 7.

The other effect that the Earth's magnetic field has on the mission is the interaction with the ECB generated magnetic field. Similar to the working principle of a magnetorquer, which are used for attitude control, a torque is induced due to the interaction of the coil generated magnetic field and the Earth's magnetic field[6]. This induced torque will, over time, align the magnetic dipole of the coil with the Earth's magnetic field.

This torque needs to be counteracted, in order for the relative position of the chaser to the target to remain the same over the duration of the detumbling mission, by using reaction wheels or Control Moment Gyros (CMGs). Another option would be to use an AC power source for the electromagnetic coil, effectively leading to a null perturbing torque on the coil for each cycle of the AC current[6]. However, this approach has the disadvantage that the current cannot be changed rapidly as discussed in Chapter 3.

In order to assess the feasibility of this mission, the torque induced by the ECB in combination with the torque induced by the Earth's magnetic field needs to be simulated and compared against existing ADCS's.

In order to find the torque created by the interaction with the Earth's magnetic field, the magnetic dipole moment of the chaser needs to be found, which can be calculated by using Equation (6.7)[28].

$$\mu_c = n_e I_0 A_{em} \tag{6.7}$$

Where n_e is the number of windings, I_0 is the current through the electromagnet and A_{em} is the loop area of the electromagnet. Using the values as presented in Chapter 3 results in a magnetic dipole of the chaser equalling $107,600$ Am^2.

The torque acting on the chaser can be found by taking the cross-product of the magnetic dipole vector of the chaser and the strength of the Earth's magnetic field:

$$\vec{T} = \vec{\mu} \times \vec{B}_{ext} \tag{6.8}$$

Where $\vec{B}_{ext}$ is the Earth's magnetic field in this case and μ is the magnetic dipole vector:

$$\vec{\mu} = I_0 \times n_e \vec{A}_{em} \tag{6.9}$$

For this problem, the Earth's magnetic field vector is given in the NED frame, while the magnetic dipole of the chaser is simulated in the frame as defined in Chapter 4. Therefore, the magnetic dipole will be converted to the NED frame before the torque is calculated. Furthermore, the maximum magnetic field vector of the Earth will be used in the calculations since the maximum torque that can work upon the chaser at any moment in time needs to be found.

First, the torque will be calculated using Equations (6.6) and (6.7), which is a simplified representation of the actual situation. The torque can then be found to be:

$$T_c = \mu_c B_{E_{950}} = 4.3654 Nm \tag{6.10}$$

Then, using the maximum value, taking into account that the Earth's magnetic feild changes direction and magnitude throughout the orbit, from Figure 6.5, the torque vector can be found:

$$\vec{T}_E = \vec{\mu} \times \vec{B}_E = [-0.1997\ 0.3459\ 0.8285]^T Nm \tag{6.11}$$

Which leads to a total torque of around $0.92 Nm$. This torque is significantly smaller than the torque found by using the simplified representation of the actual situation, which is due to the fact that the verification torque calculates the maximum torque without 3D-effects, while for the torque vector, the magnetic field vector and its position relative to the magnetic field vector of the Earth, it influences the torque generated and leads to a smaller total torque.

Adding this torque to the torque generated by the ECB and the chaser, gives a good estimate of the torque that needs to be counteracted while the ECB is active.

The maximum torque vector generated by the ECB occurs at the start of the detumbling mission when the rotation is largest and when the magnetic field vector is placed perpendicular to the initial angular velocity vector, which leads to a maximum torque vector of:

$$\vec{T}_{ECB} = [-0.0426 \; -0.0448 \; -0.0065]^T \tag{6.12}$$

The total maximum torque vector working on the chaser then equals:

$$\vec{T}_{tot} = \vec{T}_E + \vec{T}_{ECB} = [-0.2423 \; 0.3011 \; 0.8220]^T \tag{6.13}$$

It can be concluded that the torque generated by the ECB is relatively small compared to the torque generated by the Earth's magnetic field and that the total torque is around $1Nm$. The most obvious choice in order to counteract these torques is by using CMGs, of which the M50 Control Moment Gyroscope by Honeywell is an example, which shows that with the use of current technology, these torques can be easily nullified[56].

6.3. INFLUENCE OF FERROMAGNETIC MATERIALS

In previous chapters it was assumed that the Kosmos-3M rocket only consisted of conductive non-magnetic materials. In reality, there are closed current loops in instrumentations, which together with ferromagnetic materials leave residual permanent magnetism in the rocket body[57].

These residual permanent magnets will either be attracted or repulsed by the magnetic field generated by the ECB.

First, the magnetic field strength of the residual permanent magnets in the Kosmos-3M second stages needs to be estimated, which is strongly dependent on the magnetic field in which the ferromagnet is placed or which is placed upon the ferromagnet.

Applying a magnetic field to ferromagnetic materials results in the atomic dipoles aligning themselves to the magnetic field, thus resulting in a magnetic flux density, which can be expressed as[57]:

$$B_i = H_i + 4\pi I_i \tag{6.14}$$

Where B_i is the internal magnetic flux density, H_i is the internal magnetic intensity and I_i is the internal intensity of magnetization, which equals $I_i = KH_i$ where K is the magnetic susceptibility of the material.

If the permeability of the materials, μ, is known, than the above equation can be simplified as follows[57]:

$$B_i = \mu H_i \tag{6.15}$$

Even when the magnetic field is removed, part of the alignment will be retained, leading to the material being magnetized and will stay magnetized forever until a magnetic field in the opposite direction is applied to the material. It can thus be concluded that ferromagnetic materials and closed loops in instrumentation will be magnetized due to the interaction with the Earth's magnetic field. Furthermore, when the ECB is placed upon the object, these materials and closed current loops will be magnetized further.

In order to simulate the influence of these residual permanent magnets, the ferromagnetic materials in the object will be represented as rods.

The torque generated by the interaction of the magnetic field of the ferromagnetic materials and the combinations of the Earth's magnetic field and the magnetic field of the ECB, will again be simulated using Equation (6.8), where μ is the magnetic dipole vector of the rods.

The magnetic dipole or moment can then be found by[58]:

$$\mu_h = \frac{B_h V_h}{\mu_0} \tag{6.16}$$

Where B_h is the magnetic flux induced in the rod, V_h is the volume of the rod and μ_0 is the permeability of free space, which was already defined in Chapter 3.

The volume of the rod will be approximated by the percentage of ferromagnetic materials in the Kosmos-3M second stage. The magnetic flux B_h can be approximated by using the mathematical method proposed by Kumar, which is based on an induced flux density developed by Flately[59, 60]:

$$B_h = \frac{2}{\pi} B_s \tan^{-1}\left[\gamma\left(H \pm H_c\right)\right] \tag{6.17}$$

Where γ is a constant defined as:

$$\gamma = \frac{1}{H_c} \tan\left(\frac{\pi B_r}{2B_s}\right) \tag{6.18}$$

Where H is the component of the magnetic field strength aligned with the rod. Furthermore, when $dH/dt < 0$ H_c is positive and negative otherwise.

The most common ferromagnetic materials used in spacecraft are iron-alloys and steel magnets. In order to approximate the other unknowns average values will be used, which can be found in Table 6.1[61].

Table 6.1: Selection of magnetic field vectors

Coercivity	H_c	5.600	$[A/m]$
Saturation flux density	B_s	1.78	$[T]$
Remanence flux density	B_r	0.95	$[T]$
Density	ρ	8.05	$[g/cm^3]$

As a result, the constant γ can be approximated as 0.1986. In order to approximate the induced magnetic flux, B_h, first a hysterisis loop diagram needs to be made. This is necessary since the magnetic field strength varies over time as the object rotates, which means that the component of the magnetic field strength aligned with the rod, H, also varies over time.

Even without the ECB working on the Kosmos-3M rocket, the ferromagnetic materials are magnetized due to the interaction with the Earth's magnetic field. When the magnetic field is alternated, the magnetization will trace out a loop, called a hysterisis loop. However, for the Kosmos-3M second stage detumbling mission an DC power source is used, meaning that there will not be an alternating magnetic field. Additionally, due to the fact that the Earth's magnetic field is not uniform along the orbit, presented in Figure 6.3, and the fact that the object is rotating over time, the magnetic field varies over time, which in turn affects the induced magnetic flux in the rods, which is represented in Figure 6.6.

In order to model the variation in magnetic flux in the ferromagnetic rods, the magnetic field strength, H, needs to be modelled, which is dependent on the magnetic field and the permeability of the material, which in the case of this mission is an average value as was already defined.

The maximum magnetic field strength will be calculated to assess the maximum influence on the deorbiting mission, which will be further investigated in Chapter 7. The maximum magnetic

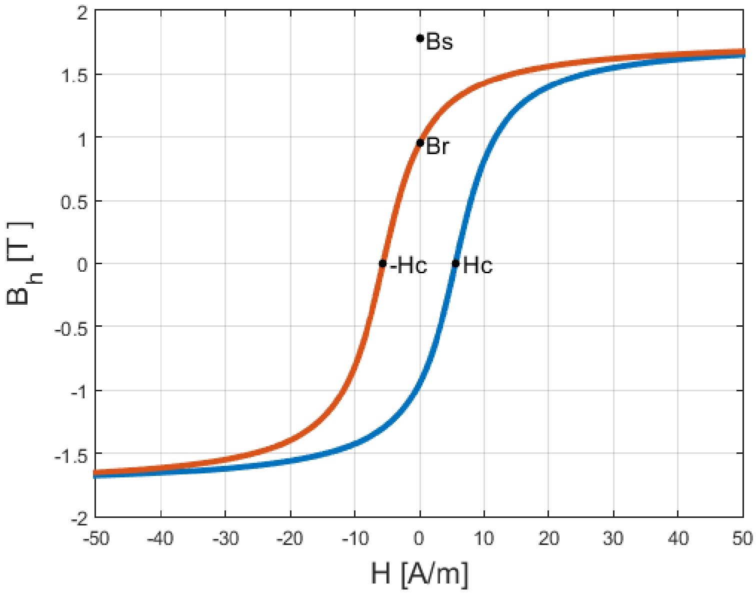

Figure 6.6: Hysterisis loop

field strength occurs when the rods are parallel to the magnetic field vector, using Equation (6.15) this results in a magnetic field strength of 6.4810^{-4} A/m.

Then, using Equation (6.16) the maximum magnetic dipole of the object can be found, when assuming 0.01% of the body consists of ferromagnetic materials. The maximum magnetic dipole of the target due to the presence of ferromagnetic materials and closed current loops, equals 19.014 A/m^2.

Finally, the maximum torque on the target, due to ferromagnetic materials in the body, can be found:

$$T_t = \mu_h B_{tot} = 0.00308 Nm \tag{6.19}$$

When comparing the torque generated by the interaction of ferromagnetic materials with the Earth's magnetic field and the magnetic field, as created by the ECB, in Equation (6.19) to the torque generated by the ECB Equation (6.12), it can be concluded that the presence of ferromagnetic elements will have an influence on the detumbling mission. In Chapter 7 this effect will be applied to the detumbling mission of the Kosmos-3M second stages as presented in Chapter 5.

In order to more accurately represent the real-life situation, a safety factor to the torque in Equation (6.19) will be added to represent the decay of the materials over time due to their interaction with the space environment, which represent the decay in the ability of the ferromagnetic materials to carry a current.

7

Final detumbling of a Kosmos-3M second stage

In this Chapter the magnetic interactions described in Chapter 6 will be added to the detumbling mission as was simulated in Chapter 5. Due to the non-uniformity of the magnetic field, the detumbling of the Kosmos-3M second rocket stage takes significantly longer. Furthermore, the influence of the Earth's magnetic field, for short term detumbling missions, is shown to have a big influence on the detumbling over the z-axis, with the influence on the angular velocity over the x- and y-axis being relatively small in comparison. For missions lasting more than 100 days, the Earth's magnetic field has a large influence on all angular velocities. And finally the presence of ferromagnetic materials and closed current loops in the target lead to small disturbances when the rotational velocity of the uncooperative object is close to zero.

Combining all the magnetic interactions, it is concluded that they have a negative effect on the detumbling time and state, with the detumbling taking both longer and converging to a higher rotational velocity compared to the results in Chapter 5. Therefore, an alternate mission is proposed that consists of three phases, namely a first detumbling phase lasting 15 days, a realignment of the chaser phase and a final detumbling phase. It is shown that when the angle over which the chaser realigns itself relative to the uncooperative object, all angular velocities converge to a value close to 0 degrees per second within the space of 31 days.

7.1. Magnetic interactions

This section will add the magnetic interactions separately to the model as shown in Figure 4.1 in order to assess their influence on the detumbling mission. In Section 7.2 these magnetic interactions will be combined in the model and the final detumbling of the Kosmos-3M upper stages will be simulated.

7.1.1. Earth's magnetic field

In order to include the effect of the Earth's magnetic field, first the orbital period of a Kosmos-3M rocket needs to be calculated. The same input parameters will be used as in Section 6.2.

$$T_{orb} = 2\pi\sqrt{\frac{a^3}{\mu_{earth}}} \approx 1.734 \text{ days} \tag{7.1}$$

When comparing the orbital period of an arbitrary orbit of a Kosmos-3M second rocket stage as shown in Figure 6.3 to the detumbling times as presented in Chapter 5, it can be concluded that the detumbling mission spans multiple orbital periods.

In Figure 6.4 the magnetic field is plotted in the x-, y- and z-direction in the NED frame plotted. Since the detumbling mission spans multiple orbital periods, the simulation of the Earth's magnetic field strength needs to be expanded. However, for the sake of simplicity and to limit the computation time, the trend found in Figure 6.4 is assumed to be repeated every orbit. In Figure 6.3 it can be seen that the orbit lanes are spaced with a constant distance. However, since the magnetic field varies especially with latitude and only slightly with longitude, the assumption to use the trend in Figure 6.4 for the entire mission will be a good approximation.

Furthermore, Figure 6.4 shows that the biggest variation and therefore the largest magnetic field occurs in the z-direction, which is the down direction in the NED frame. The z-axis of the NED frame coincides with the z-axis of the chaser fixed frame, leading to the conclusion that the variation of the magnetic field due to the influence of the Earth's magnetic field will be the largest in the z-direction.

In order to better grasp the influence of the Earth's magnetic field on the detumbling mission, a case as defined in Table 5.3 will be used.

Due to the variation of the Earth's magnetic field during the duration of the detumbling mission, the detumbling over the different axis will have disturbances. In order to assess these differences, first case 7 in Table 5.3 will be used as the magnetic field generated by the ECB at the CoG of the target, which is the optimal case. The result of this simulation can be found in Figures 7.1 to 7.3. The inputs of the model can be found in Table 5.2, which means that the influence of the non-uniformity on the magnetic field has not yet been included.

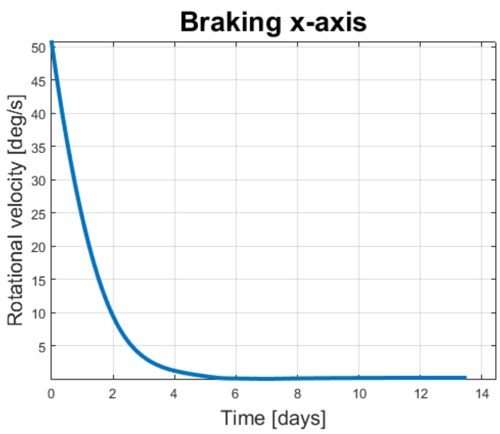

Figure 7.1: Detumbling of Kosmos-3M upper stage for case 7 over the x-axis with the influence of the Earth's magnetic field

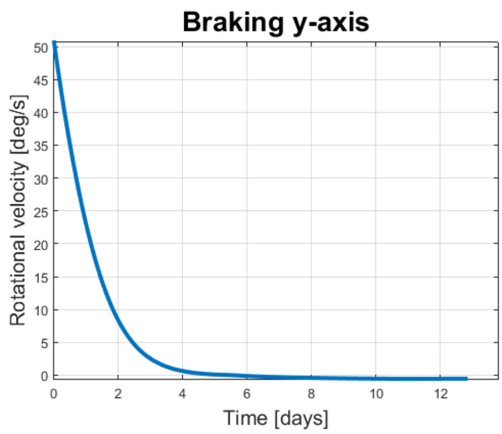

Figure 7.2: Detumbling of Kosmos-3M upper stage for case 7 over the y-axis with the influence of the Earth's magnetic field

When comparing Figures 7.1 to 7.3 to Figures 5.12 and 5.13 it can be seen that the detumbling of the x- and y-axis remains relatively similar. However, the Earth's magnetic field does have a major influence on the angular velocity over the z-axis with the rotation rate not converging to zero, which means that the magnetic field vector and the angular velocity vector have aligned over time.

Additionally, a worst case scenario, with a long detumbling time, will also be tested on the influence of the Earth's magnetic field. Therefore, case 10 in Table 5.3 will be used. The result of the simulation can be found in Figures 7.4 to 7.6.

The first noticeable difference between Figures 7.4 to 7.6 and Figures 5.16 and 5.17 is the fact that the detumbling over the x- and z-axis do not match, which is due to the fact that the Earth's magnetic field is different over the x- and y-axis. However, both angular velocities still converge to a non-zero rotational velocity in around the same period of time. Similarly to case 7 with the influence of the Earth's magnetic field, the angular velocity over z-axis takes 5 times longer, but does converge to a similar rotation rate as the case where only the magnetic field of the ECB is present.

It can thus be concluded that the Earth's magnetic field has a big influence on the angular ve-

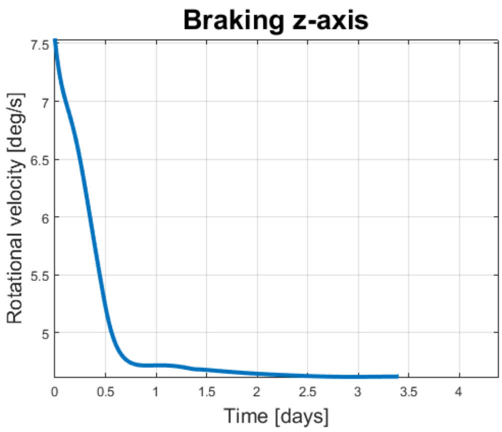

Figure 7.3: Detumbling of Kosmos-3M upper stage for case 7 over the z-axis with the influence of the Earth's magnetic field

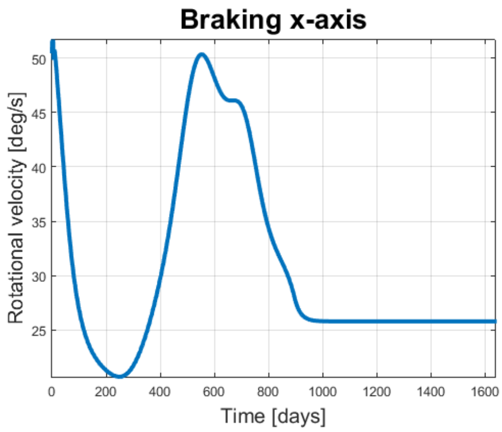

Figure 7.4: Detumbling of Kosmos-3M upper stage for case 10 over the x-axis with the influence of the Earth's magnetic field

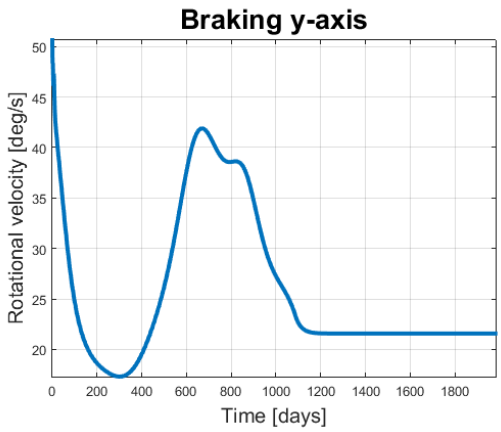

Figure 7.5: Detumbling of Kosmos-3M upper stage for case 10 over the y-axis with the influence of the Earth's magnetic field

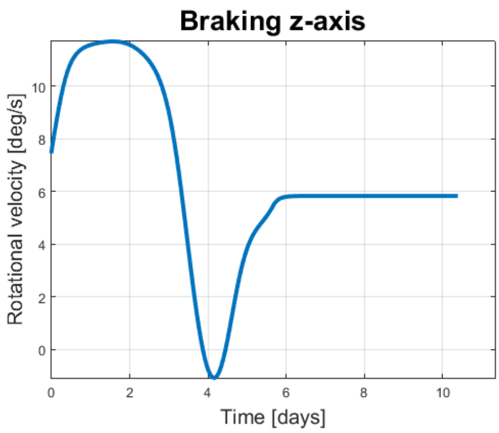

Figure 7.6: Detumbling of Kosmos-3M upper stage for case 10 over the z-axis with the influence of the Earth's magnetic field

locity over the z-axis in the chaser fixed frame, with the influence on the angular velocity over the x- and y-axis being relatively small in comparison.

7.1.2. FERROMAGNETIC MATERIALS AND CLOSED CURRENT LOOPS

In Chapter 6 it was concluded that the influence of ferromagnetic materials and closed current loops will have a relatively small influence on the detumbling mission. However, in Chapter 6 the maximum torque was calculated, while for the duration of the detumbling mission, the torque will vary over time due to the variation of the Earth's magnetic field and the relative position of the ferromagnetic bars of the Kosmos-3M to the resulting magnetic field vector.

Similarly to the addition of the Earth's magnetic field, in order to better grasp the influence of the presence of ferromagnetic materials and closed current loops on the detumbling mission, cases 7 and 10 of Table 5.3 will be used.

Again, leaving out the non-uniformity of the magnetic field and the Earth's magnetic field, case 7 with the addition of ferromagnetic elements as defined in Chapter 6 leads to the detumbling simulation as presented in Figures 7.7 to 7.9.

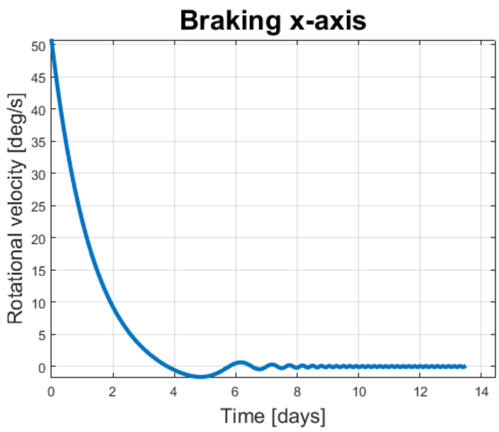

Figure 7.7: Detumbling of Kosmos-3M upper stage for case 7 over the x-axis with the influence of ferromagnetic materials

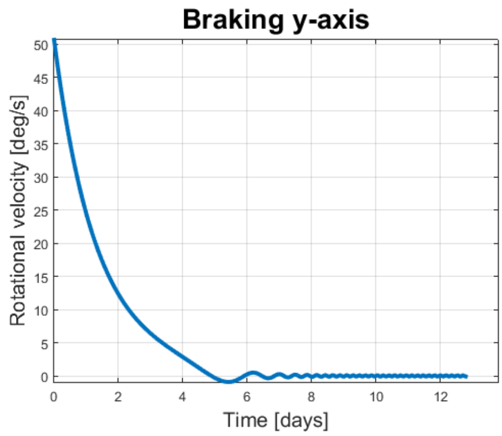

Figure 7.8: Detumbling of Kosmos-3M upper stage for case 7 over the y-axis with the influence of ferromagnetic materials

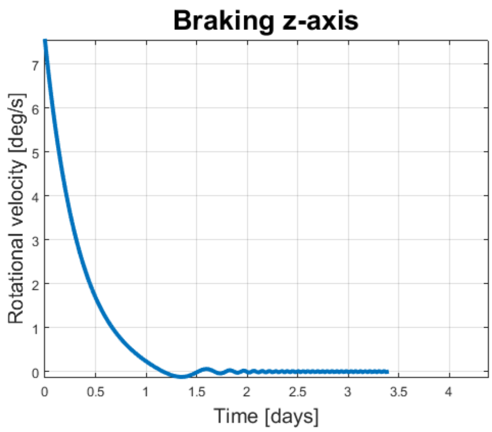

Figure 7.9: Detumbling of Kosmos-3M upper stage for case 7 over the z-axis with the influence of ferromagnetic materials

When comparing Figures 7.7 to 7.9 to Figures 5.12 and 5.13 it can be seen that they differ only slightly, with the angular velocity over all axis approaching zero faster, but taking longer to converge. However the velocity never truly converges, which is due to the fact that when the rotational velocity approaches zero, the influence of the torque due to the ferromagnetic materials becomes larger than the influence of the torque created by the ECB.

In Figures 7.10 to 7.12 case 10 is simulated with the addition of ferromagnetic materials. However, for case 10 the rotational velocities do not converge to zero, but instead converge to a new steady state where there is still a rotational velocity present. As a result, the influence of the torque due to the ferromagnetic materials is relatively small compared to the total rotational velocity, leading to no noticeable effect to be perceived when looking at the mission over a long period of time (days).

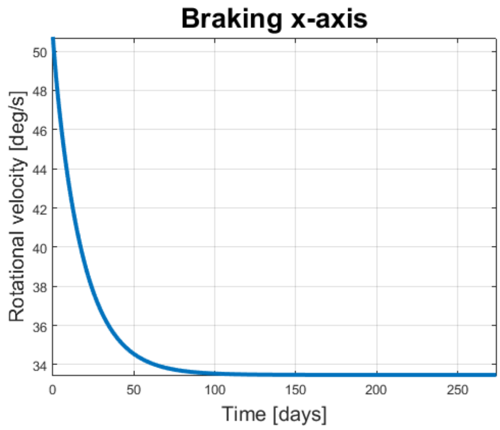

Figure 7.10: Detumbling of Kosmos-3M upper stage for case 10 over the x-axis with the influence of ferromagnetic materials

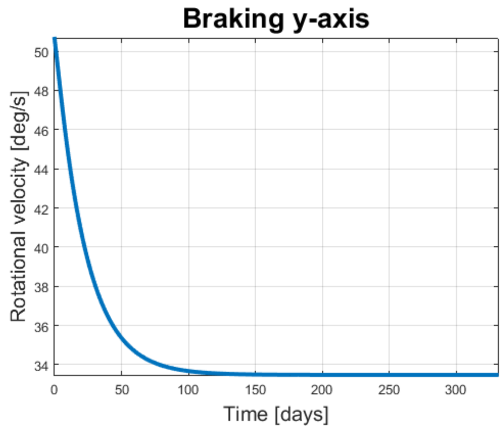

Figure 7.11: Detumbling of Kosmos-3M upper stage for case 10 over the y-axis with the influence of ferromagnetic materials

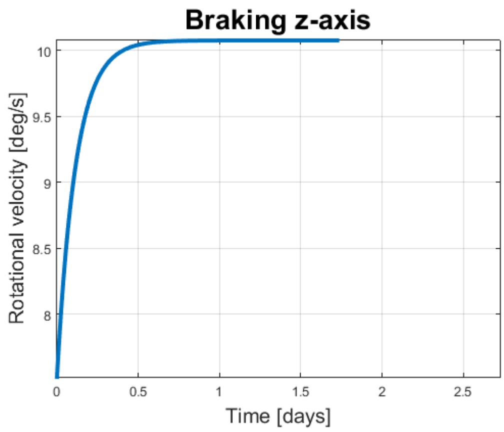

Figure 7.12: Detumbling of Kosmos-3M upper stage for case 10 over the z-axis with the influence of ferromagnetic materials

It can thus be concluded that the presence of ferromagnetic materials in the Kosmos-3M rocket will only have a small influence on the detumbling mission. However, if eddy current braking was to be applied to an uncooperative object with a higher percentage of ferromagnetic materials on its body, then the interaction of the ferromagnetic materials and the ECB will have a more noticeable influence on the detumbling mission.

7.2. FINAL DETUMBLING OF KOSMOS-3M UPPER STAGES

In order to more accurately simulate the detumbling of the Kosmos-3M second stages, compared to Chapter 5, all magnetic interactions discussed in Chapter 6 will be added to the model as presented in Figure 4.1. This results in new steps to be taken and a different flow of the model, as can be seen in Figure 7.13.

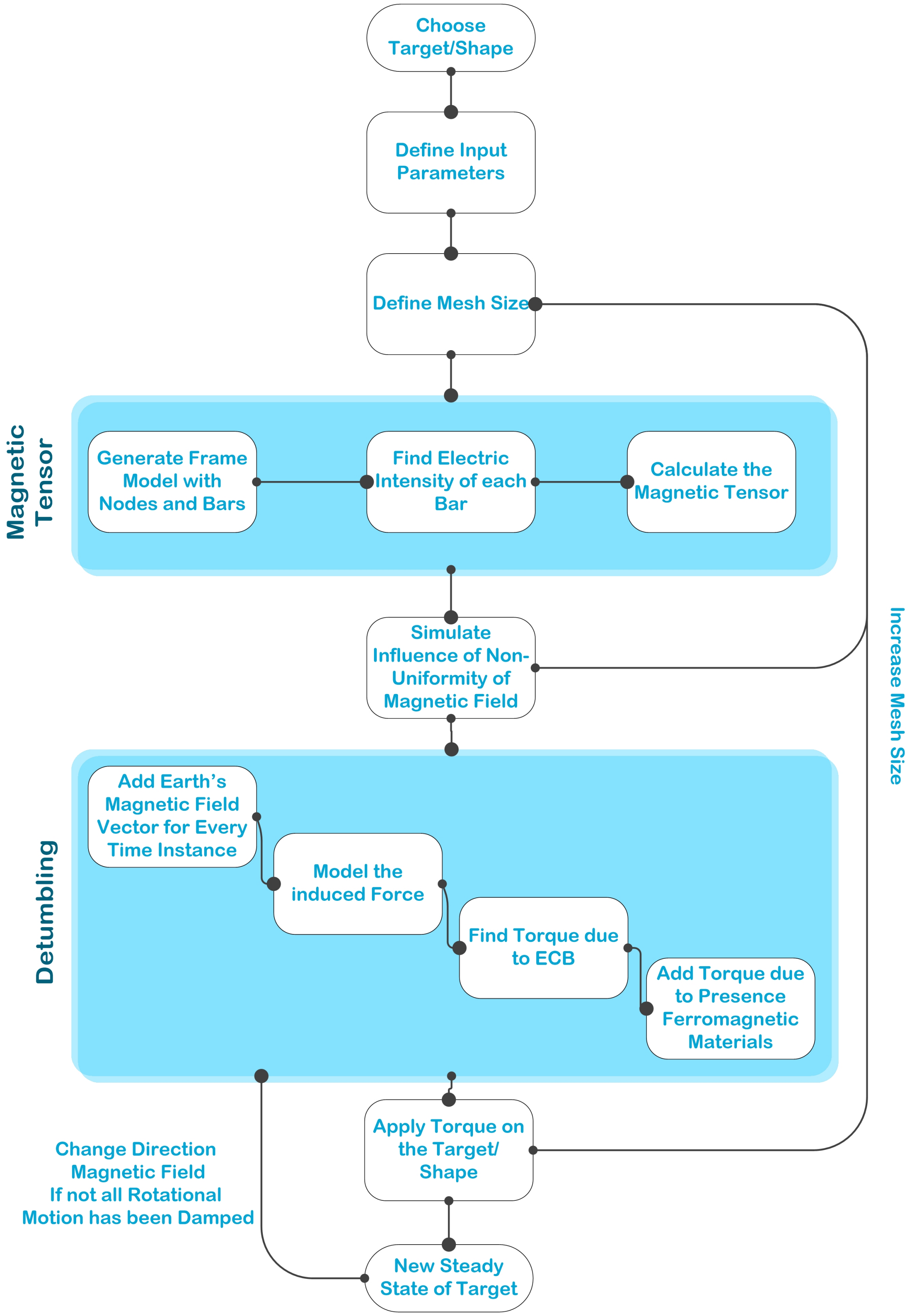

Figure 7.13: Final detumbling modelling procedure

In Section 7.1, it was shown that the magnetic interactions do not lead to the uncooperative objects' rotational velocities converging to zero independent of the magnetic field vector's position. This leads to the conclusion that either a prior mission is necessary in order to accurately determine the target's state or that the chaser needs to realign itself over time or after a certain amount of time in order to assure that all angular velocities are damped within the limit as defined in Chapter 2. The latter will be tested and simulated in this Section.

In order to simulate the realignment of the chaser, first the operating time of the ECB needs to be defined. In Figures 5.18, 5.20, 5.22, 5.24 and 5.26 the time the ECB needs to detumble the Kosmos-3M second rocket stages to a new steady state was represented, and as a result the average detumbling time can be found. The time, without the outliers since they represent undesirable cases with long detumbling times, after which 99% of all angular velocities have converged, equals 15 days.

The mission will thus consist of three phases, namely: an initial detumbling phase equalling 15 days, a chaser realigning phase assumed to last 1 day and a final detumbling phase.

Case 4 of Table 5.3 will be used to test the assumption that all rotational velocities can be damped with realigning the chaser over a fixed angle. This angle will be assumed to be 90 degrees initially. Later in this Chapter, the sensitivity of the angle on the detumbling mission will be investigated.

In Figures 7.14 to 7.16 Case 4 is plotted for the new mission design consisting of the three phases. The rotational velocity over all axes converge to a value close to zero degrees per second.

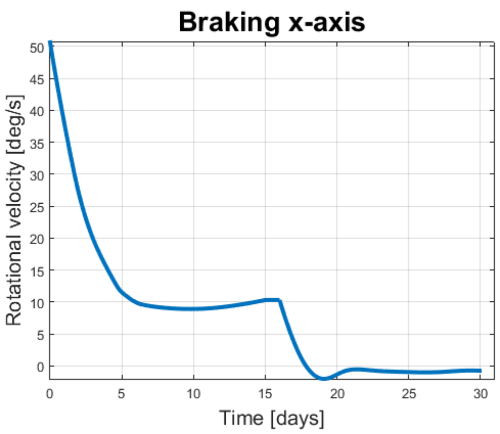

Figure 7.14: Detumbling of Kosmos-3M upper stage for case 4 over the x-axis with all magnetic perturbations

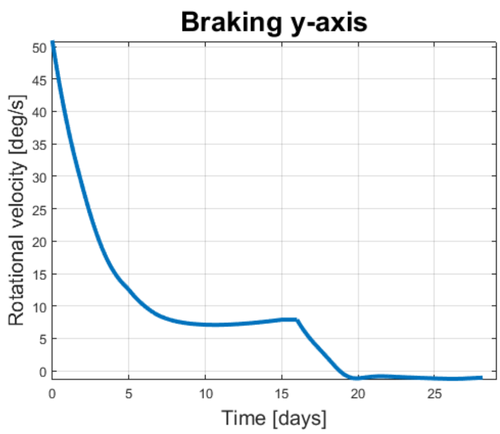

Figure 7.15: Detumbling of Kosmos-3M upper stage for case 4 over the y-axis with all magnetic perturbations

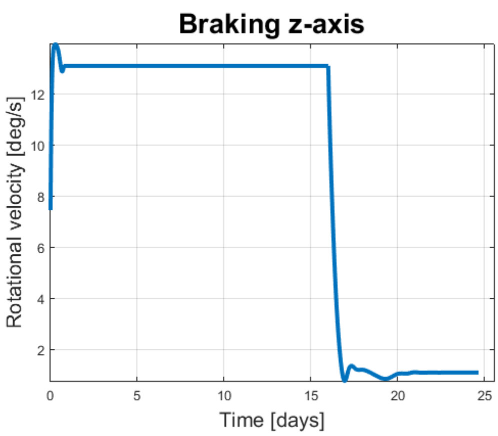

Figure 7.16: Detumbling of Kosmos-3M upper stage for case 4 over the z-axis with all magnetic perturbations

In order to test if all angular velocities will converge to zero with this new mission design consisting of three phases, an overview in different planes, similar as in Chapter 5, is presented in Figures 7.17 to 7.21. The rotational velocity the model converges to, is plotted over 360 degrees in fixed planes separated by 45 degrees in order to provide an overview of the new steady states.

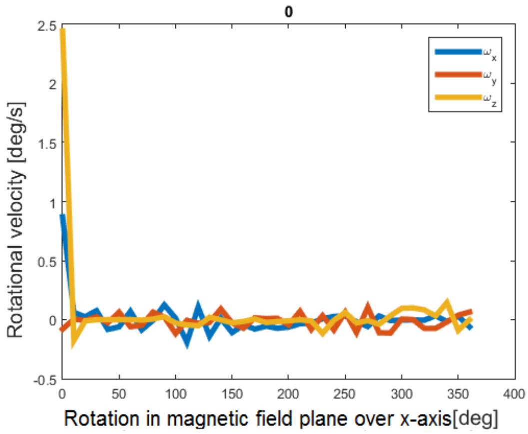

Figure 7.17: Final converged rotational velocity in a plane 0 degrees rotated over the z-axis

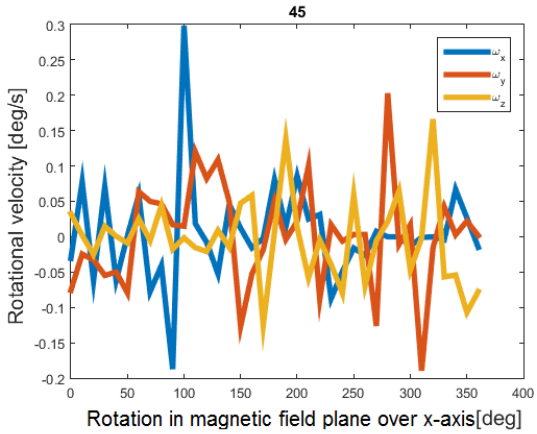

Figure 7.18: Final converged rotational velocity in a plane 45 degrees rotated over the z-axis

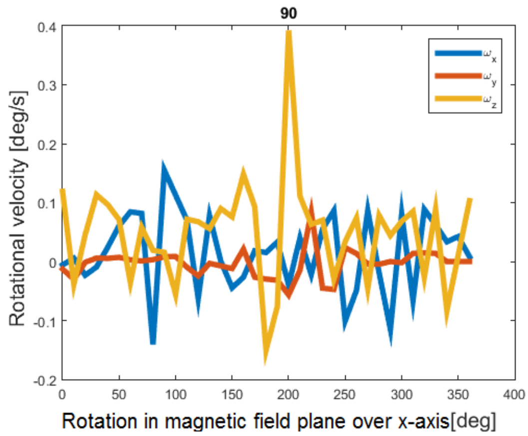

Figure 7.19: Final converged rotational velocity in a plane 90 degrees rotated over the z-axis

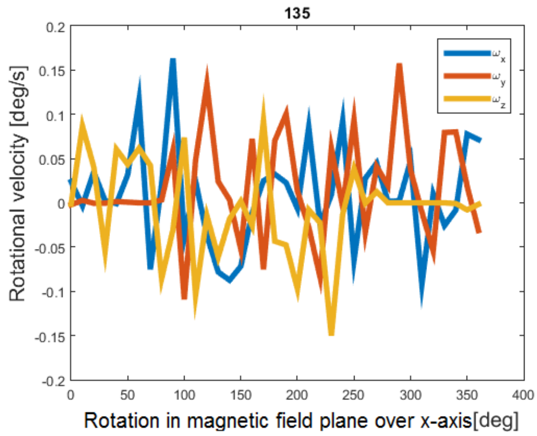

Figure 7.20: Final converged rotational velocity in a plane 135 degrees rotated over the z-axis

Figures 7.17 to 7.21 show that all angular velocities, except for one outlier in Figure 7.17, are damped to a value close to zero degrees per second. For some cases, the angular velocity converges to a negative value, which is due to the magnetic interactions added to the model. It can thus be concluded that the Kosmos-3M second rocket stage can be detumbled without prior knowledge on its state. Furthermore, the period in which the object is detumbled takes on average 19 days, and can take as long as 31 days.

However, realigning the chaser perfectly over an angle of 90 degrees could prove to be difficult, therefore, the sensitivity of the realignment of the chaser will be tested by rotating the chaser over an angle of 60 degrees instead, the result of which can be found in Figures 7.22 to 7.26.

As can be seen in Figures 7.22 to 7.26, the rotational velocity still converges to a value close to zero, indicating that the chaser does not need to be realigned over exactly 90 degrees relative to the chaser. The smaller the angle over which the chaser realigns itself, the larger the detumbling times, since the magnetic field vector and the angular velocity vector are nearly parallel for cases where the chaser realigned itself over an angle smaller than 45 degrees.

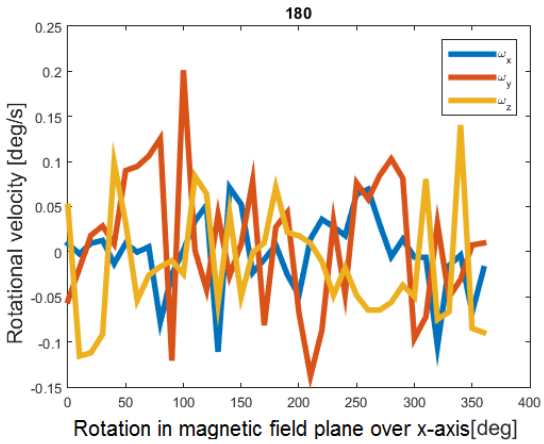

Figure 7.21: Final converged rotational velocity in a plane 180 degrees rotated over the z-axis

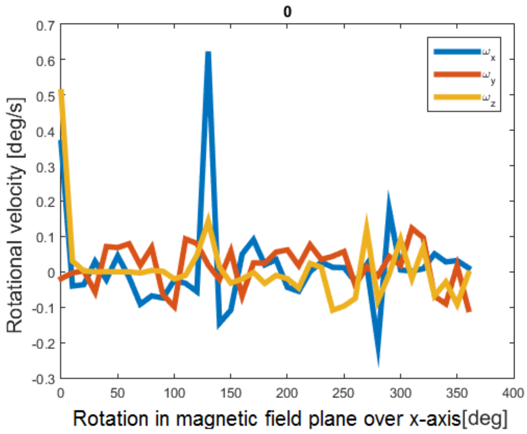

Figure 7.22: Final converged rotational velocity in a plane 0 degrees rotated over the z-axis

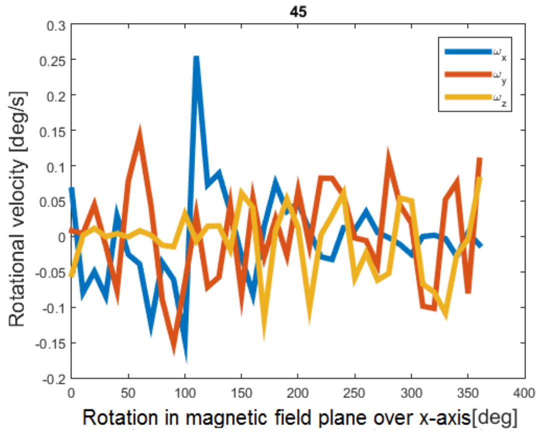

Figure 7.23: Final converged rotational velocity in a plane 45 degrees rotated over the z-axis

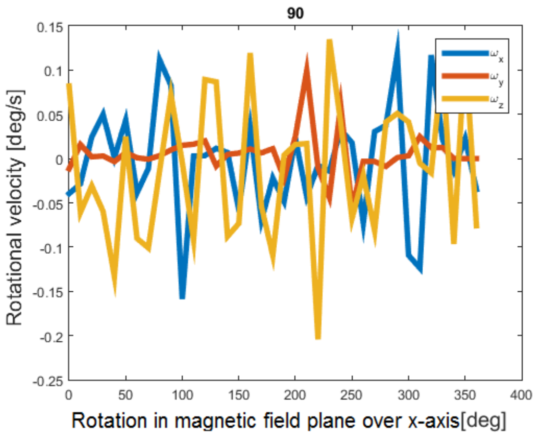

Figure 7.24: Final converged rotational velocity in a plane 90 degrees rotated over the z-axis

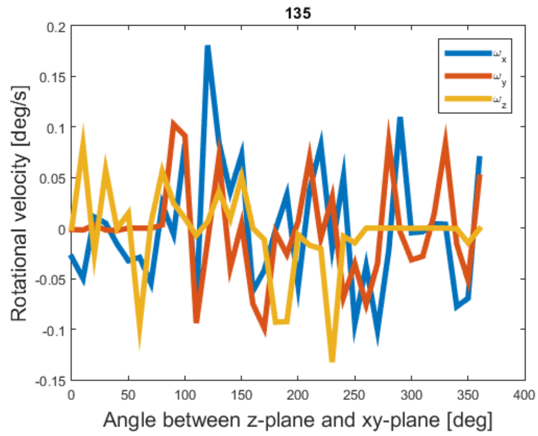

Figure 7.25: Final converged rotational velocity in a plane 135 degrees rotated over the z-axis

It can thus be concluded, that in order to minimize the detumbling time and assure that the Kosmos-3M upper stages are detumbled to a near-zero value, the chaser needs to realign itself after the first detumbling phase over an angle that is close to 90 degrees, after which a second detumbling

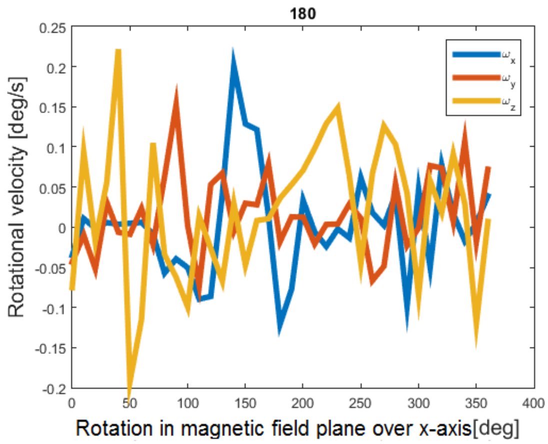

Figure 7.26: Final converged rotational velocity in a plane 180 degrees rotated over the z-axis

phase needs to be initiated.

8

Conclusion and Recommendations

8.1. Conclusion

No matter what measures are taken, space debris will remain a problem for current and future space missions. Ever since the space race between the USA and the Soviet Union, the Earth orbits have been cluttered with debris, many smaller than 1 cm. Removing all these objects is impossible, but removing or repairing the objects that pose the most risk at colliding with other debris or current and future missions could drastically reduce these risks. However, before an active debris removal or on-orbit servicing mission can be undertaken, the debris needs to be detumbled.

This Thesis focuses on the most common types of debris in Earth orbits, which are second rocket stages. More specifically, a high spatial density of debris is located at an altitude between 800 and 900 km. The Kosmos-3M upper stages make up more than half of the uncooperative objects in this altitude range and are considered ideal targets. They are of equal size and shape, they are robust and have few appendages, which simplifies the debris removal mission greatly. Furthermore, their body has a high percentage of conductive material, which is necessary to achieve fast detumbling times when using the eddy current braking technique.

All target shapes in the thesis are detumbled by the use of an eddy current brake (ECB), which means that a magnetic field is created and aimed at the uncooperative object by an electromagnet carried by a chaser. This electromagnet will be an electromagnetic coil made from magnesium diboride MgB_2, which is a high temperature superconductor, with a radius of 1 meter, 500 windings and a current of 500 Ampere. This electromagnet will output a magnetic field with a strength of 0.022 Tesla at the center of the coil and a magnetic field strength of 162.4 μT at a distance of 5m from the center of the coil which coincides with the CoG of the object.

Ideally, the detumbling technique, ECB, needs to work for a wide range of shapes and sizes in order to be able to detumble a large amount of the debris population. Therefore, different shapes and sizes were used for the Magnetic Tensor model in order to show that they can be detumbled with the use of an eddy current brake (ECB). More specifically, a sphere, cylinder, double silo and Kosmos-3M second rocket stage were modelled. The sphere, cylinder and double silo were only tested for specific scenario's, but the results are a good indicator that targets of different shapes and sizes can be detumbled with the use of an ECB. For fully conductive shapes or targets, the angular velocity was shown to converge to a new steady state after no more than 12 days for the test scenario's.

Furthermore, since all materials can be considered a conductor, where a good conductor has a low resistance and a bad conductor a high resistance, the ECB technique can also be applied to targets that have a relatively low ratio of high conductive material. This is shown for both the double silo and Kosmos-3M second stage configurations, with the ratio of high conductive material to the total mass varying between 32.5 and 25 %. The ratio of conductive material in the body of the target, influences the strength of the induced torque and thus the detumbling times, with a smaller ratio of conductive material leading to a weaker induced torque and longer detumbling times.

The initial detumbling simulation of the basic shapes and the Kosmos-3M second rocket stage ignores all forces and torques except for the torque induced by the ECB. The detumbling of the Kosmos-3M second rocket stage, with an angular velocity vector equalling [50.63 50.63 7.53] deg/s, was tested for different magnetic field vectors, meaning that the magnetic field vector is pointing in a different direction for each simulation. It was concluded that a Kosmos-3M second stage can be detumbled with the use of an ECB in the span of 7 days when the magnetic field vector is perpendicular to the initial angular velocity vector. However, the detumbling time and new steady state are dependent on the combination of the magnetic field vector and the angular velocity vector. More specifically, when the magnetic field vector approaches any of the major axes of ration or approaches the angular velocity vector, long detumbling times are measures, which exponentially increase with diminishing angle between the angular velocity vector and the magnetic field vector.

In order to model the detumbling of the Kosmos-3M upper stages more accurately, additional magnetic interactions were added to the model. It was shown that the non-uniformity of the magnetic field has a negative impact on the detumbling time. Furthermore, the Earth's magnetic field has a large influence on the detumbling of the z-axis for short detumbling times, while for longer detumbling times, all angular velocities experience a strong effect from the Earth's magnetic field. Finally, the presence of ferromagnetic materials in the Kosmos-3M second stages only has a noticeable influence over the entire detumbling mission when the angular velocity converges to a value close to zero degrees per second.

It can be concluded that the detumbling of the Kosmos-3M upper stages, which combines all magnetic interactions, cannot be guaranteed without a prior mission to asses their state or a subsequent detumbling phase. An alternate mission design, which includes a first detumbling phase, a realignment phase, where the chaser realigns itself over a certain angle relative to the uncooperative object, and a second detumbling phase, guarantees the Kosmos-3M upper stages to converge to a rotational velocity close to zero degrees per second. However, the angle over which the chaser realigns itself strongly influences the detumbling time. For ideal circumstances, the Kosmos-3M upper stages can be detumbled within the space of 19 days, while the worst case scenario, where the chaser has realigned itself over an angle smaller than 45 degrees, the detumbling can take as long as 3 years.

8.2. RECOMMENDATIONS

In this thesis, an initial design of the ECB was made. In order to assess the statement that the electromagnetic coil can be powered solely by solar panels on the chaser, a more detailed electromagnet can be designed together with a detailed chaser design. In order to arrive to a final detailed chaser design, the mission as a whole will need to be designed, where the chaser operations from the moment they are launched need to be simulated, including flying to an uncooperative target, performing a rendez-vous, flying in formation, realignment of the chaser relative to the target and flying to the next uncooperative target. This design includes the mission lifetime, from which the number of space debris objects that can be removed from Low Earth Orbit follows, an overview of the flight times, and the fuel necessary in order to perform in-orbit manoeuvres. Additionally, the non-magnetic aspects of formation flying and how it influences the detumbling mission can be assessed to test the viability of the mission as a whole and to investigate which instruments and attitude determination and control systems are best suited for this mission.

Alternatively, future research can also focus on the targets. Eddy Current Braking can be applied to different shapes and sizes than those presented in this thesis, with different conductive material ratios in order to assess the efficiency of using an ECB for different shapes, materials, etc. Furthermore, in order to more accurately simulate the detumbling of the Kosmos-3M upper stages, the materials used and their place in the rocket body can be updated to better represent the real-life situation.

BIBLIOGRAPHY

[1] B. Bastida and H. Krag, *Strategies for active removal in leo,* in *Proceedings of the 5th European Conference on Space Debris* (ESA SP-672, 2009).

[2] M. M. Castronuovo, *Active space debris removal—a preliminary mission analysis and design,* Acta Astronautica **69**, 848 (2011).

[3] M. Emanuelli, *Design and evaluation of an active space debris removal mission with chemical and electrodynamic tether propulsion systems,* in *2012 Beijing Space Sustainability Conference* (Beijing, China, 2012).

[4] L. Corpaccioli, J. Deloo, and T. a. Knop, *Termination of Hazardous and Obsolete Rocket Stages Final Report*, Report (Faculty of Aerospace Engineering, TU Delft, 2012).

[5] A. Flores-Abad, O. Ma, and K. a. Pham, *A review of space robotics technologies for on-orbit servicing,* Progress in Aerospace Sciences **68**, 1 (2014).

[6] K. Kumar, N. O. Gomez, and J. M. R. a. Martin, *Robotic system for active debris removal: Requirements, state-of-the-art and concept architecture of the rendezvous and capture (rvc) control system,* (2015).

[7] e.Deorbit, , *CDF study report*, Report (ESA, 2012).

[8] K.Wormnes, R. L. Letty, and L. a. Summerer, *Esa technologies for space debris remediation,* ESA (2013).

[9] J. Reed, J. Busuets, and C. White, *Grappling system for capturing space debris,* 2nd European Workshop for Active Debris Removal (2012).

[10] T. V. Peters, A. Pellacani, and P. a. Attina, *Cobra active derbis removal concept,* in *64th International Astronautical Congress* (Beijing, China, 2013).

[11] S.-I. Nishida and S. Kawamoto, *Strategy for capturing of a tumbling space debris,* Acta Astronautica **68**, 113 (2011).

[12] T. Bennett, D. Stevenson, and E. a. Hogan, *Prospects and challenges of touchless electrostatic detumbling of small bodies,* Advances in Space Research **56**, 557 (2015).

[13] Inter-Agency Space Debris Coordination Committee (IADC), , *Key definitions of inter-agency space debris coordination committee (iadc),* (2013).

[14] M. Force, *When the nature and duration of space becomes appropriation: A proposition – "use" as a legal predicate for a state's objection to active debris removal,* in *International Astronautical Congress* (Space Generation Advisory Council, Beijing, China, 2013).

[15] T. Chow, D. Prasad, and G. a. Federico, *Conceptualizing an economically, legally and politically viable active debris removal option,* in *International Astronautical Congress* (Space Generation Advisory Council, Beijing, China, 2013).

[16] Inter-Agency Space Debris Coordination Committee (IADC), , *Space debris: Iadc assessment report for 2011,* (2013).

[17] D. S. McKnight, F. Di Pentino, and A. a. Kaczmarek, *System engineering analysis of derelict collision prevention options,* Acta Astronautica **89**, 248 (2013).

[18] D. Mcknight, *The orbital debris hazard: fact or fiction,* in *MIT Alumni Club* (Cognovation).

[19] R. Biesbroek, *The e.deorbit cdf study: A design study for the safe removal of a large space debris,* in *6th IAASS Conference* (ESA).

[20] M. H. Kaplan, B. Boone, and R. a. Brown, *Engineering isssues for all major modes of in sity space debris capture*, AIAA Space 2010 Conference & Exposition (Anaheim, California, 2010).

[21] J. C. Liou and N. L. Johnson, *A sensitivity study of the effectiveness of active debris removal in leo,* Acta Astronautica **64**, 236 (2009).

[22] C. Bombardelli, *Deorbiting / reorbiting of space debris with an ion beam shepherd satellite,* in *2011 Beijing Space Sustainability Conference* (Universidad Politécnica de Madrid).

[23] L. E. Z. Jasper, C. R. Seubert, and H. a. Schaub, *Tethered tug for large low earth orbit debris removal,* in *AAS/AIAA Astodynamics Specialists Conference* (Charleston, South Carolina, US, 2012).

[24] S.-b. Liao, P. Dourmashkin, and J. W. Belcher, *Faraday's law,* in *Course Notes: Physics 8.02 Electricity and Magnetism at MIT* (Massachusetts Institute of Technology, 2004).

[25] Innospection, *Eddy current theory,* (2011).

[26] S. Abiko, *Detumbling and capturing strategies with eddy current brake system on orbital space robot,* in *IEEE International Conference on Robotics and Automation*, edited by J. Shibaura Institute of Technology (IEEEE).

[27] M. Jankovic, K. Kumar, and N. O. a. Gómez, *Spacecraft concept for active de-tumbling and robotic capture of ariane rocket bodies,* (2015).

[28] N. O. Gomez and S. J. Walker, *Eddy currents applied to de-tumbling of space debris: Analysis and validation of approximate proposed methods,* Acta Astronautica **114**, 34 (2015).

[29] F. Sugai, S. Abiko, and T. a. Tsujita, *Detumbling an uncontrolled satellite with contactless force by using an eddy current brake,* in *Intelligent Robots and Systems (IROS), 2013 IEEE/RSJ International Conference on*, pp. 783–788.

[30] F. Sugai, S. Abiko, and T. a. Tsujita, *Development of an eddy current brake system for detumbling malfunctioning satellites,* in *System Integration (SII), 2012 IEEE/SICE International Symposium on*, pp. 325–330.

[31] J. H. Durrell, A. R. Dennis, and J. a. Jaroszynski, *A trapped field of 17.6 t in melt-processed, bulk gd-ba-cu-o reinforced with shrink-fit steel,* Superconductor Science and Technology **27**, 082001 (2014).

[32] J. Vanderlinde, *Classical Electromagnetic Theory*, Vol. 2nd Ed. (Kluwer Academic Publishers, New York, USA, 2004).

[33] W. D. Markiewicz, D. C. Larbalestier, and H. W. a. Weijers, *Design of a superconducting 32 t magnet with rebco high field coils,* Applied Superconductivity, IEEE Transactions on **22**, 4300704 (2012).

[34] R. A. Bamford, B. Kellett, and J. a. Bradford, *An exploration of the effectiveness of artificial mini-magnetospheres as a potential solar storm shelter for long term human space missions,* Acta Astronautica **105**, 385 (2014).

[35] M. A. Susner, M. D. Sumption, and M. A. a. Rindfleisch, *Critical current densities of doped mgb2 strands in low and high applied field ranges: The jc(b) crossover effect,* Physica C: Superconductivity **490**, 20 (2013).

[36] A. Gurevich, S. Patnaik, and V. a. Braccini, *Very high upper critical fields in mgb 2 produced by selective tuning of impurity scattering,* Superconductor Science and Technology **17**, 278 (2004).

[37] K. Grinter, *John f. kennedy space center - frequently asked questions,* (2000).

[38] B. Collaudin and N. Rando, *Cryogenics in space: a review of the missions and of the technologies,* Cryogenics **40**, 797 (2000).

[39] V. Baturkin, *Micro-satellites thermal control—concepts and components,* Acta Astronautica **56**, 161 (2005).

[40] MMS Wire Industries, , *Magnet wire insulation guide,* (2014).

[41] S. J. St. Lorant and E. Tillmann, *Superconducting magnets in high radiation environments: Design problems and solutions,* in *11th International Conference on Magnet Technology (MT-11)*, edited by T. Sekiguchi and S. Shimamoto (Springer Netherlands, 1990) Book section 120, pp. 697–702.

[42] National Aeronautics and Space Administration, , *Assessment and control of spacecraft magnetic fields,* **NASA SP-8037** (1970).

[43] J. Ormsby, *Eddy Current Torques and Motion Decay on Rotating Shells*, Report (United States Air Force, 1967).

[44] L. Smith, *A Theoretical Study of the Torques induced by a Magnetic Field on Rotating Cylinders and Spinning Thin-wall Cones, Cone Frustums, and General Body of Revolution*, Report (Planetary and Space Science, National Aeronautics and Space Administration, 1962).

[45] R. A. Schill, *General relation for the vector magnetic field of a circular current loop: a closer look,* Magnetics, IEEE Transactions on **39**, 961 (2003).

[46] D. Dew-Hughes, *The critical current of superconductors: an historical review,* Low Temperature Physics **27**, 713 (2001).

[47] U. A. Bakshi and A. V. Bakshi, *Electromagnetic fields* (Technical Publications, Pune, India, 2010).

[48] B. Shibaji, P. Siddhartha Shankar, and B. a. Partha, *Pulsed magnetic field measurement outside finite length solenoid: Experimental results & mathematical verification,* Journal of Electromagnetic Analysis and Applications **2013** (2013).

[49] M. Eisterer, *Magnetic properties and critical currents of mgb 2,* Superconductor Science and Technology **20**, R47 (2007).

[50] O. NanoScience, *Mercury instrumentation: Intelligent control of cryogenic and magnetic environments,* (2011).

[51] I. Cryomagnetics, *Model 4g superconducting magnet power supply,* (2011).

[52] S. OdenWald, S. Higley, and D. a. Janney, *Space Math* (NASA, 2013).

[53] D. Halliday, J. Walker, and R. Resnick, *Fundamentals of Physics* (Wiley, 2008).

[54] J. Meriam and L. Kraige, *Engineering Mechanics: Statics* (Wiley, 2011).

[55] J. Wertz and W. Larson, *Space Mission Analysis and Design* (Springer Netherlands, 1999).

[56] Honeywell, *M50 control moment gyroscope,* (2006).

[57] *XIth International Astronautical Congress: Stockholm, 1960, Proceedings : Main Sessions* (1961).

[58] H. S. Ousaloo, *Hysteresis nutation damper for spin satellite,* The Open Aerospace Engineering Journal **6**, 1 (2013).

[59] R. R. Kumar, D. D. Mazanek, and M. L. Heck, *Simulation and shuttle hitchhiker validation of passive satellite aerostabilization,* Journal of Spacecraft and Rockets **32**, 806 (1995).

[60] T. W. Flatley and D. A. Henretty, *A magnetic hysteresis model,* (1995).

[61] K. Kaiser, *Electromagnetic Compatibility Handbook* (Taylor & Francis, 2004).